Testing Quadru- and Octopolar Asymmetry in Planck Data

Sara Clausen Jønvik

Thesis submitted for the degree of
Master of Science in Astronomy

Institute of Theoretical Astrophysics
University of Oslo

15.09.2017

Abstract

We perform an investigation of quadru- and octopolar asymmetry in the CMB data by expanding the on the study of alignment and angular clustering of the dipole components of the CMB power distribution across multipoles $l = 2$ to $l = 1500$, as done in section 6.5 in the 2015 Planck isotropy article Ade et al. (2016c). We develope a routine that is able to extract the underlying spherical harmonic coefficient of a masked map, up to $l = 3$. The direction of the quadrupole and octoplar components are defined as in de Oliveira-Costa et al. (2004) and a pseudo-Rayleigh statistic is used to estimate the significance of the clustering as the portion of simulations based on the ΛCDM model that exhibit a clustering greater than the observational data. We find no significan clustering in neither the quadrupole or the octople. A correlation analysis is also performed in order to avoid the problems arising from the definition of direction in the quadrupole and octopole. This analysis does not find a significant clustering in the dipole, in tension with the results published in Ade et al. (2016c), but detects a tentative clustering in the octopole. Investigations with larger number of simulations are needed in order to better assess the accuracy of the results found here.

Acknowledgements

This thesis was written as a part of a Master's Degree in Astronomy at the University of Oslo.

I would like to thank my supervisor Frode K. Hansen who's neverending optimism, encorougement, cheery demeanor and good humour. It has made the more frustrating parts of this thesis manageable. Thank you also for your pedagogical patience while helping me understand the occasionally hard to grasp problems arising during my work the past year, and for creating a very interesting proposal for my thesis.

Thank you to ITA and the student adnimistration for letting me take the time I need, enabling me to finish this thesis properly even through a very hard and difficult time in my life.

Thank you Viljar, for your encoragement, gallows humour and patiance especially during the last couple of months. Cannot say with certainty that I would have handled the situation as well as you have. To Marit for your at times annoyingly optimistic and energetic outlook on life. And to all of you guys in the Stellar Cellar, who made the bad or boring days much less bad and much less boring.

And last, but by no means least: Tor Arne Tørresdal Fossum, this is for you. I promised I would finish it. Thank you for all you did for me.

Contents

Chapter 1

Introduction

Everywhere around our little blue dot there is a diffuse, isotropic microwave radiation, peaking at about 160 GHz in frequency. It permeates the universe from all directions, with an average temperature of 2.7248 K and small variations of the order of 10^{-5} K (Fixsen, 2009). This was first discovered in 1964, rather by accident [1], by two radio astronomers Arno Penzias and Robert Wilson, who originally thought it must have been some undetermined systematic noise. Fortunately they soon became aware that a phenomenon much like this had in 1948 been theorized by George Gamow, Ralph Alpher, and Robert Herman.

This background radiation is a remnant from the time of recombination, approximately 380 000 years after the Big Bang and epoch of inflation. Before this the universe consisted of a hot plasma of free electrons, protons and photons, the temperature being too high to allow protons and electrons to combine. The photons went through constant Compton scattering of the free electrons (Dodelson, 2003), resulting in a mean free path much shorter than the particle horizon and an opaque universe. At some later point the expansion enabled a significant amount of protons to combine with the free electrons, allowing the photons to travel freely. This point is what is referred to as recombination, the first point (according to modern cosmological models) that the protons and electrons could combine to simple atoms. Thus, this creates a sort of fog wall, a limit to how far out/back in time we can see. Naturally, this is of great interest to cosmologists. It creates an image of how the universe was at the moment of photon-matter decoupling, enabling us to observe the over/under densities in the early universe, the tiny seeds of matter and dark matter that later clump together into large scale structures. This image, so to speak, gives us a glimpse into the state of the early universe. The statistical properties of the Cosmic Microwave Background (CMB) is a direct measure of the beginning of the universe, whether or not our universe went through a big bang, inflation, matter content etc. The initial discovery of it's long theorized presence sparked interest among cosmologists all over the world, but alas in the following decades observations were more or less limited to estimations of the average temperature, which was consistently estimated to be about 3 K.

Theorists predicted the fluctuations in the temperature created by the gravitational potential wells and and photons traversing these wells, but it was not until the COsmic Background Explorer (COBE) satellite made its first measurements that we were able to really use this microwave radiation to explore the properties of the early universe. The final result of the COBE mission was the thermal spectrum of the CMB (see figure 1.1) showing a the most precise black

[1] `http://aether.lbl.gov/www/science/cmb.html`

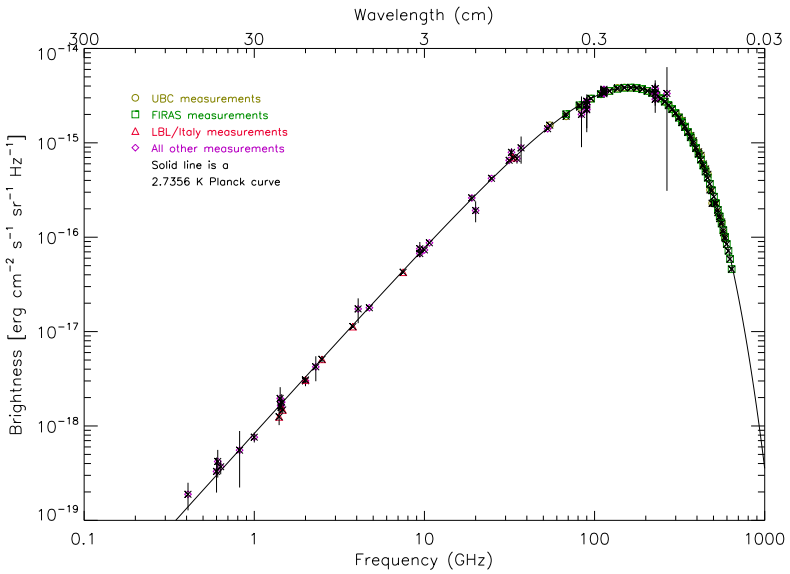

Figure 1.1: Thermal spectra of the CMB as shown in Smoot (1999). The solid curve shows a theoretical Planckian spectrum, with the dots and marks give the different instruments on the COBE satellites and other experiments.

body measurement ever measured [2], peaking at around $\lambda = 0.19$ cm. If the universe did indeed start out with a hot Big Bang, we would expect the resulting thermal spectrum to be a perfect black body spectrum (with some irregularities due to later red-shift effects). The COBE results more or less confirmed the Big Bang model as the ruling cosmological model.

Observations with the DMR instrument on COBE confirmed the presence of tiny anisotropies at a power of 3 mK with a near scale-invariant spectrum in the isotropic and largely homogeneous radiation, confirming the presence of long theorized gravitational wells in the early universe. These gravitational over and under density areas were a large part of what enabled matter to later clump together into the large scale structures we observe today, and the anisotropies gave a glimpse into the processes in the early inverse and a foundation for the theories of large-scale structures. Alas, even if the resolution was impressive with tools available at the time, COBE could only probe the intermediate and large scales of the universe, with the finer details washed out by the limiting resolution, as demonstrated in figure (1.2)

With COBE's successor, the Wilkinson Microwave Anisotropy Probe (WMAP), we were finally able to probe the smaller scales of the sky, gaining much more detailed information about the smaller temperature fluctuations. Compared to COBE, WMAP gave an enormous increase in the resolution of the CMB maps, with an angular resolution of less than 0.2 degrees (Bennett et al., 2003) (see upper right of figure 1.2). This enabled us to do much more detailed and precise parameter estimation of different models describing the matter-energy content in the universe, concluding that the ΛCDM model (cold dark matter universe with a term containing a cosmological constant) was the best possible fit to the resulting data (Spergel et al., 2003). Some of the simplest inflationary models of the time provided very good fits (Komatsu et al., 2003) (Peiris et al., 2003a), and the detection of early reinoziation more or less completely ruled out warm dark matter as a possible dark matter candidate (Spergel et al., 2003) The res-

[2] Not including lab experiments

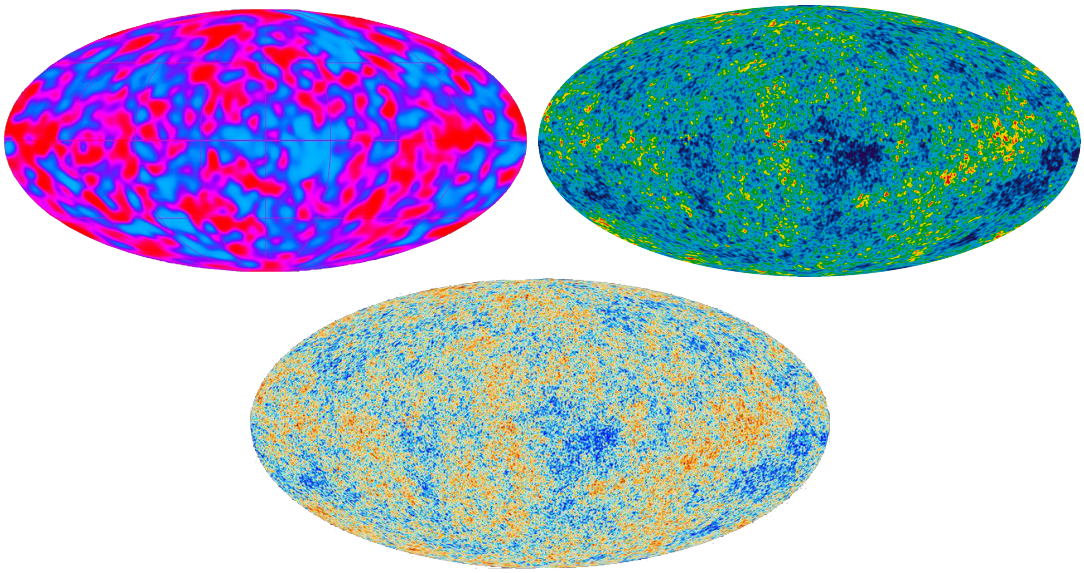

Figure 1.2: Comparison of the three maps produced by COBE (top left), WMAP (top right) and Planck (bottom) satellites. Sources: COBE (`https://science.nasa.gov/missions/cobe`), WMAP 9-year map (`https://map.gsfc.nasa.gov/resources/cmbimages.html`), Planck (`http://www.esa.int/spaceinimages/Images/2013/04/Planck_CMB_black_background`)

ulting data also presented limits on the potential non-Gaussian nature of the primordial density fluctuations, determining that the non-Gaussian fluctuations were, if present, too small to detect with the resolution available (Komatsu et al., 2003).

The data from the Plank satellite (bottom part of figure 1.2) improved the resolution of the observations further, being able to distinguish structures between 33 and 5 arcseconds apart (varying between detectors/frequency bands) (Ade et al., 2014a). It also had a larger frequency range in the observations (Ade et al., 2014a), giving a much better handle on foregrounds and point sources. This enabled us to do improved testing of the anomalies first found in COBE and WMAP, and with a different experiment with different scanning strategies, beam function and so on, it provided a good test as to whether the previous anomalous detections were a product of systematics in the satellite and data analysis, or a feature in the CMB data.

The results of the Planck mission further strengthened the conclusions drawn from the WMAP data, and the results were still in excellent agreement with the 6-parameter ΛCDM model (Ade et al., 2014d). The constraints on said parameters were improved significantly. They found no significant detection of non-Gaussianities in the data after correcting for foregrounds (Ade et al., 2014g) (Ade et al., 2014f), and none of the possible extensions made to the ΛCDM model improved the fit noticeably beyond what you would expect from including more parameters.

Although no non-Gaussianities were found, there were signs of some deviations from isotropy. Several of these where also discovered in the WMAP data, but with no way to cross check with other large scale experiments at the time, most of them were thought to be the results of badly resolved foregrounds or unknown systematics. The discovery of the same deviations in the Planck data, which had widely different methods and systematics, meant that these deviations were a part of the CMB.

One such anomaly was the apparent presence of a dipolar distribution in the fluctuations of the CMB (Ade et al., 2016c). This hemispherical power asymmetry in the anisotropies appeared

in both the WMAP and Planck data with very similar direction, indicating that they were true features in the CMB, and not a result of the (very different) systematics of the two experiments (see figure 3.4). If the universe is indeed isotropic, this power asymmetry should not have been present. The significance of the detection was just in the limit of what is possible with the random nature of the CMB signal, but high enough to warrant further inspection (see figure 3.4) .

The goal of this thesis is to generalize the code used to detect the clustering of the dipole direction in the Planck data to inspect if we can see the same clustring in higher order multipoles. I will expand the `remove_dipole` routine in HEALPix in order to estimate the spherical harmonic coefficients of a masked map, and extend the clustering analysis to quadru- and octopolar asymmetry in the distribution of power in the CMB across multipoles. The challenge then is to find some definition of direction valid for quadrupoles and octopoles (which is much less intuitive than the dipole) or to develop some sort of method we can use to compare entire maps instead of just directions (e.g correlation). In the end I will produce direction illustrations and significance plots of the same type as the ones used in the Planck Isotropy article (see Ade et al. (2016c)).

The structure of this thesis is as follows: Chapter 2 will give an introduction to the power spectrum of the CMB and describe the general properties of the spherichal harmonic transform in order to illustrate how the map analysis is performed, as well as describe the MASTER code used to generate the maps. Chapter 3 gives a more thorough introduction to the Hemispherical Dipole asymmetry and how the analysis was performed in the Planck 2013 (Ade et al. (2014f)) and Planck 2015 release (Ade et al. (2016c)) and the statistics used there. In chapter 4 we outline the mathematics involved in generalizing the `remove_dipole` routine in order to find the underlying quadrupole and octopole components, how the direction of these components are defined, and the estimation of correlation between maps/images. Chapter 5 describes the cross check performed on the routine, and the resulting significance of our analysis. Chapter 6 discusses the abovementioned results and in chapter 7 we conclude.

Chapter 2

Spherical Harmonics, Power Spectrum & CMB Analysis

ΛCDM is an abbreviation for a dust-filled (CDM) universe governed by a cosmological constant Λ. It describes a universe dominated by what we today call dark matter, matter which can only interact with baryonic matter through gravitation, and dark energy (Λ), in addition to relativistic and non-relativistic particles, as described by the standard cosmological paradigm. In the early stages of the universe, baryonic matter, dark matter and radiation dominated the expansion rate and general evolution of the universe. Dark energy had a negligible effect in that regard, but is today thought to be the dominating factor responsible for the accelerating expansion (Lyth, 1993).

The two key assumptions behind this model are that the universe is homogeneous on large scales and isotropic. In other words the content of the universe is more or less evenly distributed when you consider very large scales, and no matter which direction you look in it looks the same. We are assuming that the *cosmological principle* holds: "Viewed on a sufficiently large scale, the properties of the universe are the same for all observers" (Keel, 2007). If we assume, in addition, that our place in the cosmos is not privileged over any other place, then the assumption of isotropy around us implies that the Universe appears isotropic as seen from any point of observation. The homogeneity of the Universe follows from the isotropy around every point of observation. This assumption gives us an important vantage point when observing the universe and creating cosmological models. It means that our position of observation is not special, that moving our vantage point a couple of millions of light years does not affect the results of observations on large scales and, therefore, that our observations and conclusions drawn from said observations are general observations valid at any point in the universe.

Of course, the assumption of homogeneity breaks down at smaller scales as can be easily proved simply by looking at the night sky. This is the case on somewhat large scales as well as we have observed both clusters and clusters of clusters (superclusters) of galaxies. The largest structures detected today are the somewhat infamous *Sloan Great Wall* with a size of 400 Mpc at red-shift 0.073 (Gott et al., 2005) which was detected in the Sloan Digital Sky Survey, and the *Hercules-Corona Borealis Great Wall* even further away at red-shift ~ 2, with an observed size of 2000-3000 Mpc (Horvath et al., 2014) (Horvath et al., 2015). When talking about the homogeneous universe we often speak of the sizes along the line of the *Hubble radius*[1],

[1] Also referred to as the Hubble horizon, Hubble volume or Hubble sphere

$\sim c/H_0 \approx= 45000$ Mpc (*proper* horizon, not comoving). This scale is the limit beyond which objects are receding from an observer faster than the speed of light due to the expansion of the universe. On top of this homogeneous background we have density fluctuations leading to large scale structures, which according to the assumption of isotropy should appear the same no matter what direction we look in. The assumption of isotropy is what we will test in this thesis.

2.1 Spherical Harmonics

Figure 2.2 shows the four foreground cleaned CMB maps published in the 2013 Planck results, from the four different component separation methods chosen for the Planck data Ade et al. (2014b). We will in this thesis use data which is foreground cleaned using only the SMICA method, because the SMICA map was concluded as the map with the lowest foreground contamination (Ade et al., 2014b). The data sets used are the Planck data from the public release 2, which can be found on the web page of the *Planck Legacy Archive*, `http://pla.esac.esa.int/pla/#home`, an online archive for data and information, containing all public products of the Planck mission.

In order to extract the multitude of information present in the CMB we need a set of tools that enables to effectively study the statistical properties of maps made up of $\sim 5 \times 10^7$ pixels for each detector in the satellite (Ade et al., 2014c). This is done by using the spherical harmonic transform of the CMB-map (Hivon et al., 2002).

The spherical harmonics satisfy the spherical harmonics equation, and are given as the angular part of the Laplace equation. Formally, it is defined (from Boas (2006)) as

$$Y_{lm}(\theta, \phi) \equiv \sqrt{\frac{2l+1}{4\pi} \frac{(l-m)\,!}{(l+m)\,!}} P_{lm}(\cos\theta) e^{im\phi}, \tag{2.1}$$

where $P_{lm}(\cos\theta)$ is the associated Legendre polynomial, usually looked up in tables. The first multipoles of the spherical harmonics, up to the quadrupole, are shown in equations 2.4-2.12.

Assuming we have a map of the form $T(\theta, \phi)$, where θ and ϕ are the spherical coordinates describing the position of the pixel, and T is the temperature measured at said pixel, we can transform the temperature variations in the map to a set of spherical harmonics $Y_{lm}(\theta, \phi)$ using

$$a_{lm} = \int T(\theta, \phi) Y^*_{lm}(\theta, \phi) \sin(\theta) d\theta d\phi, \tag{2.2}$$

which has the inverse transform

$$T(\theta, \phi) = \sum_{l=0}^{\infty} \sum_{m=-l}^{l} a_{lm} Y_{lm}(\theta, \phi) \tag{2.3}$$

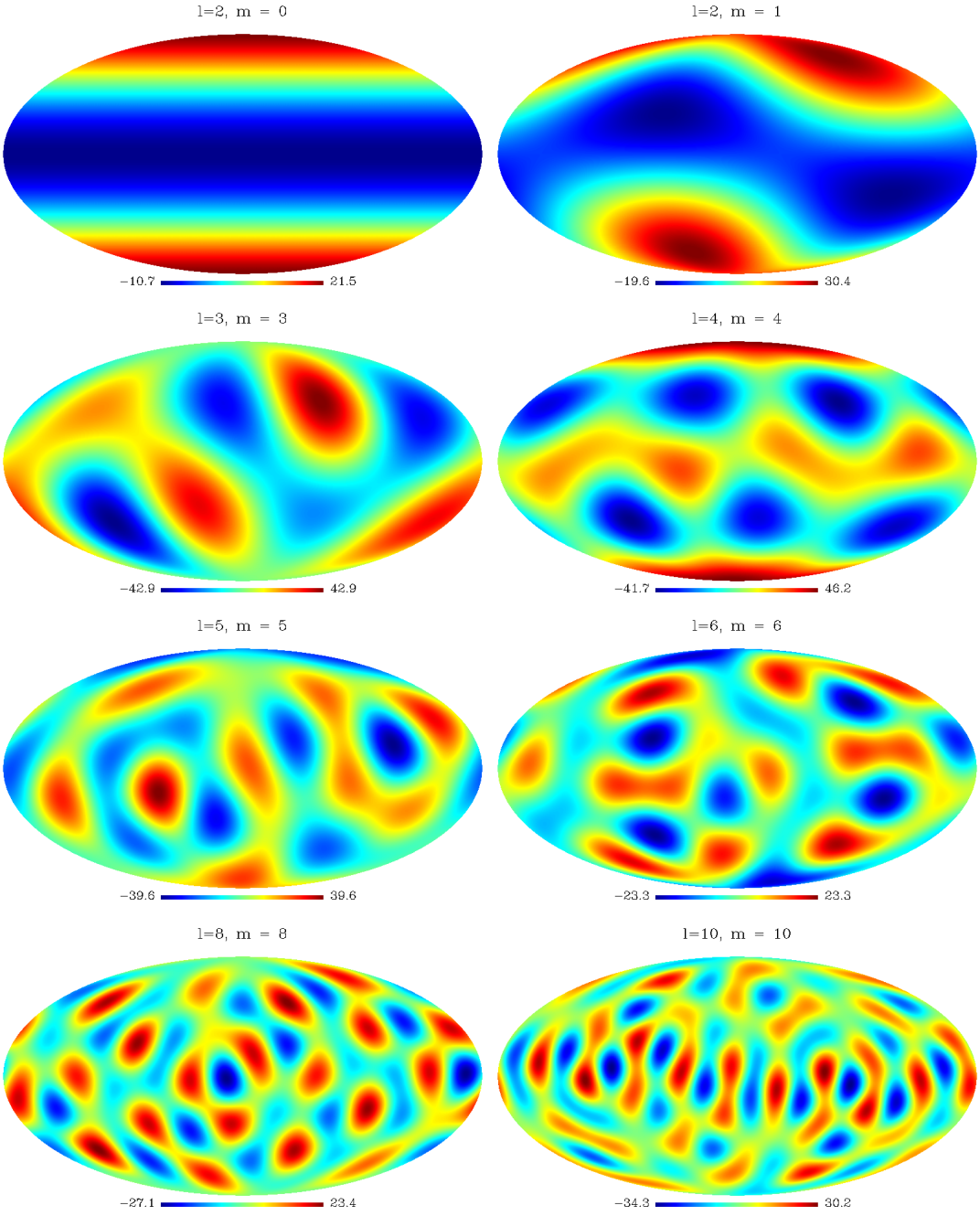

Figure 2.1: Maps of the spherical harmonic coefficients (a_{lm}) generated for a set of multipoles l and m. These were constructed from power spectrum given in the file `cl.fits` from the HEALPix package as example data (Gorski et al., 2005). The maps contain values from only the given multipole l, and m from 0 up to the value given above each map, with contributions from lower l set to 0 and where produced using the `create_alm` and `alm2map` commands in the HEALPix package. The multpoles were chose to give a feeling of what how the scales change with multipole and how the phase change from m twists the orientation of the "blobs" in the maps (see the first two maps).

$$Y_{00} = \frac{1}{2}\frac{1}{\sqrt{\pi}} \tag{2.4}$$

$$Y_{1-1} = \frac{1}{2}\sqrt{\frac{3}{2\pi}}\sin\theta e^{-i\phi} \tag{2.5}$$

$$Y_{01} = \frac{1}{2}\sqrt{\frac{3}{\pi}}\cos\theta \tag{2.6}$$

$$Y_{11} = -\frac{1}{2}\sqrt{\frac{3}{2\pi}}\sin\theta e^{i\phi} \tag{2.7}$$

$$Y_{2-2} = \frac{1}{4}\sqrt{\frac{15}{2\pi}}\sin^2\theta e^{-2i\phi} \tag{2.8}$$

$$Y_{2-1} = \frac{1}{2}\sqrt{\frac{15}{2\pi}}\sin\theta\cos\theta e^{-i\phi} \tag{2.9}$$

$$Y_{20} = \frac{1}{4}\sqrt{\frac{5}{\pi}}\left(3\cos^2\theta - 1\right) \tag{2.10}$$

$$Y_{21} = -\frac{1}{2}\sqrt{\frac{15}{2\pi}}\sin\theta\cos\theta e^{i\phi} \tag{2.11}$$

$$Y_{22} = \frac{1}{4}\sqrt{\frac{15}{2\pi}}\sin^2\theta e^{2i\phi} \tag{2.12}$$

We are decomposing the map into components that can be described by a coefficient a_{lm} and a spherical harmonic, Y_{lm},

$$T(\theta,\phi) = a_{00}Y_{00}(\theta,\phi) + a_{10}Y_{10}(\theta,\phi) + a_{11}Y_{11}(\theta,\phi) + a_{1-1}Y_{1-1}(\theta,\phi) + a_{20}Y_{20}(\theta,\phi) + \cdots$$

up to the desired multipole l. The a_{00} term describes the monopole, e.g. average temperature, the a_{1m} gives the dipole, a_{2m} is the quadrupole and a_{3m} is the octopole. The monopole is often removed from the maps before map analysis because the mean temperature is of little interest as is the dipole due to earth's orbit around the sun.

In order to completely describe the map using the a_{lm} coefficients we need to include all multipoles up to ∞, which is impossible. But including only the coefficients up to a given $l_{\max}$ will produce a map containing all the information on scales down to $\Delta\Phi_{l_{\max}} = 180^\circ/l_{\max}$- The multipole m which runs from $-l$ to l describes the phase multipoles. For example, creating a map from spherical harmonics and a_{lm} coefficients up to $l_{\max} = 1000$ will produce a map with variations and details down to $\Delta\Phi_{1000} = 180^\circ/l_{\max} = 180^\circ/1000 = 0.18^\circ$, and the multipoles m will affect the details oriantation with respect to each other. Example maps produced for different multipoles are shown in figure 2.1, where we can see the effect of the phase m in the first two maps in the top of the figure.

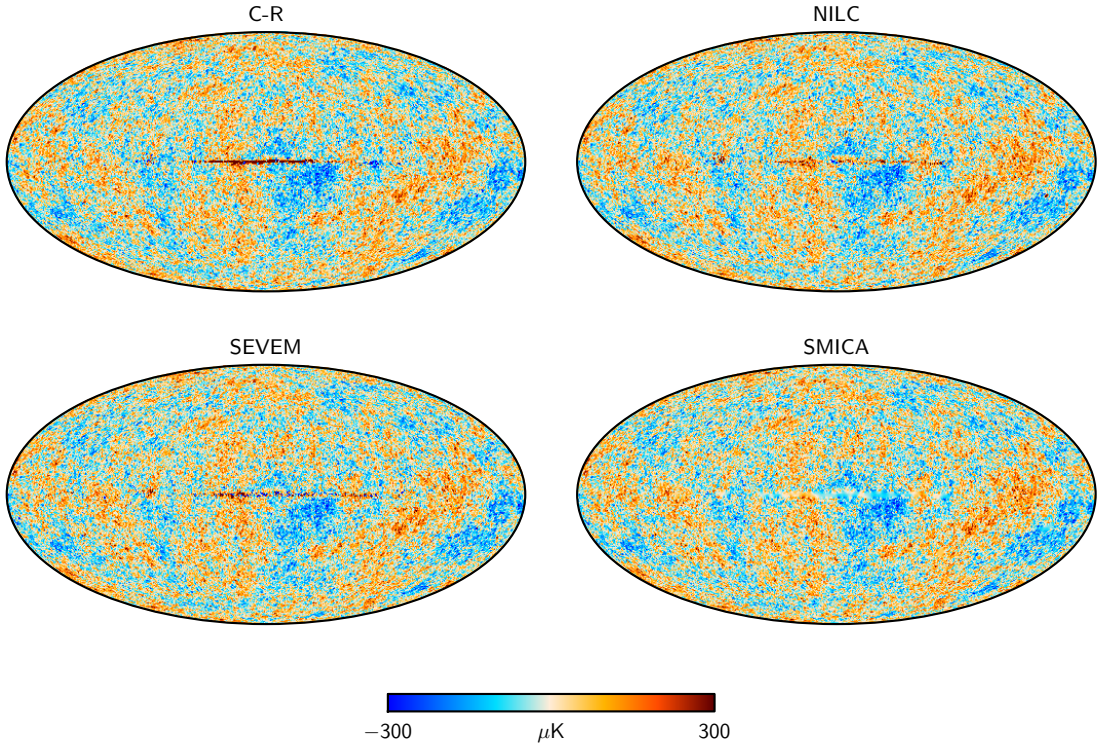

Figure 2.2: Maps produced from the 2013 Planck data using the four different component separation techniques for foreground removal (Commander-Ruler, NILC, SMICA, SEVEM) as shown in Ade et al. (2014b).

With this decomposition we can study the map at size ranges of interest. We can analyle the different components separately and study the relation/correlation between different ranges, both in the maps themselves and using the a_{lm} coefficients (Paykari, P. and Starck, J. L., 2012).

2.2 The Power Spectrum

The power spectrum of the spherical harmonic transform of a map like the CMB map gives us the strength of the variations at a given scale/multipole l . If, for example, the value of the power spectrum at multipoles around 500 is very high, the fluctuations on scales around 0.36° are very strong. The power spectrum given with the 2013 Planck results are shown in figure 2.3, with the fiducial model containing the theoretical predictions given as the red line in the figure (for more details, see Dodelson (2003)). The conclusion reached in the 2015 Planck release confirms the results published in (Ade et al., 2014d) with some improvements in how the low-l spectrum and systematics are handled, again concluding that the six-parameter base ΛCDM model as a very good match to the observed CMB sky and it's power spectrum (Ade et al. (2016b)).

2.2.1 Constructing a Simulated CMB Map from a Theoretical Model

The temperature variations we observe in the CMB are a direct result of perturbations to photon fluctuations, here denoted as Θ. This quantity can, through much tedious work already per-

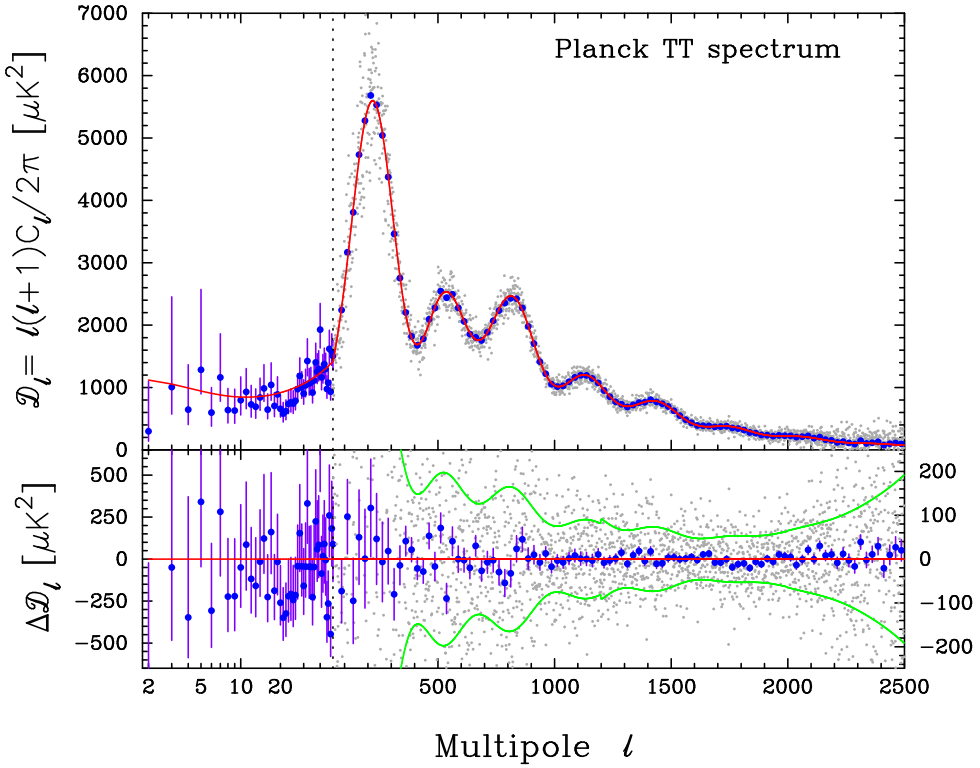

Figure 2.3: Power spectrum published with the 2013 Planck articles (Ade et al., 2014d). The fiducial ΛCDM model is shown as the red line with the power spectrum produced from the data are given as the gray dots. The blue dots with error bars show the data averaged over multipole bins of $\Delta l \approx 31$ with 68 % confidence intervals given by the asymmetric error bars. The black dotted line going vertically through the plot indicates the cut between the low range and high range at $l = 50$. In the lower multipole range, from $l = 2$ to 49 the data is given using a logarithmic scale on the multipole axis in order to better show the variations at lower multipoles. Along the rest of the multipole axis the scale is linear. The lower part in the plot shows the residual when subtracting the fiducial model. The green lines indicate the $\pm 1\sigma$ errors. Note the change in vertical scale in the lower panel at $l = 50$. The y-range values for $l \geq 50$ are given on the right side og the plot while the y-range for $l = 2 - 49$ are given on the left side.

formed in great detail by my betters in Dodelson (2003) and Øystein Elgarøys supplementary cosmology notes in AST5220 at the university of Oslo [2], be estimated by the use of perturbation theory and General Relativity. The main goal of an analytical expression for these variations would be to relate them to the physical quantities governing the behavior of our universe. Only key points are repeated here in order to give a sense of how the theoretical power spectrum is constructed.

Since the temperature variations can be expressed as perturbations of photon fluctuations, the Boltzmann equation would be a natural first step. It can be expressed in a very general form as

$$\frac{df}{dt} = C[f], \tag{2.13}$$

where the quantity C denotes a general form of the interaction between different forms of particles. The left hand side gives the time derivative of the distribution function, e.g. Bose-Einstein for photons. In short, the resulting Boltzmann equation for photons becomes,

$$\dot{\Theta} + ik\mu\Theta + \dot{\Phi} + ik\mu\Psi = -\dot{\tau}(\Theta_0 - \Theta + \mu v_b) \tag{2.14}$$

where the terms have been Fourier transformed in order to simplify the calculations, resulting in the ik factor where k is the wavenumber. Θ describes the perturbations to the photon fluctuations as a function of wavenumber (equivalent to position) and photon momentum ($\hat{p}$), μ describes the direction of the photon propagation and v_b is the bulk velocity of electrons. The time derivative with respect to conformal time is denoted by the dots above the respective symbols and τ is defined as the optical depth up to a certain conformal time η. The terms Ψ and Φ denote the gravitational and a curvature potential of space-time, respectively. Θ_0 is the numerical value of Θ integrated across a sphere defined by the photon momentum.

Solving this differential equation is anything but simple. It involves a dozen of coupled differential equations that needs to be solved simultaneously. But within this maze of equations are nearly all necessary information needed to create a CMB power spectrum. The matter-energy content, gravitational potential, curvature, the amount of different particles present in the early universe. Everything is in the end contained in the solution to the coupled differential equations, except for the general effects of inflation, which have not been included in the calculations up to this point.

We can now define a theoretical power spectrum from the photon fluctuation perturbations at the time of recombination. Intuitively since the variations we measure on the sky are temperature fluctuations we would expect that the strength of said fluctuations would be given by a relation on the form $C_l \sim \Theta_l^2$, but since the scale dependence of the coupled differential equations has been ignored up to this point by setting the initial condition of Φ to 0, we need to include a primordial power spectrum $P(k)$:

$$C_l = \int P(k)\Theta_l^2(k)\frac{d^3k}{(2\pi)^3} \tag{2.15}$$

The photon fluctuation perturbations now act as a tranfer function that relates the fluctuations at the time of recombination to what we observe today. The spectrum $P(k)$ describes the scale

[2] `http://www.uio.no/studier/emner/matnat/astro/AST5220/v16/pensumliste/index.html` Acquired 31.08.2017

dependence and consequences of the quantum fluctuations arising during the epoch of inflation. It can be inferred from experiments like the CMB or other large scale structure experiments, and quite similarly to the CMB describes the power of the initial quantum fluctuations as a function of scale, this time given by the wavenumber k (Peiris et al., 2003b). Most inflationary models predict some power law primordial spectra, as shown in 2.16 with some normalization constant $P(k_0)$ at a pivot scale k_0 (usually chosen to simplify calculations), with or without a "running" of the spectral index given by the derivative in the power in equations 2.16 or the running of the running given by the second order derivative (Ade et al., 2014e). Most modern theories of inflation predicts that these fluctuations are close to Gaussian random distributed, leading the fluctuations in the power spectrum to also be Gaussian random distributed.

$$P(k) = P(k_0)\left(\frac{k}{k_0}\right)^{n_s(k_0)+\frac{1}{2}(dn_s/d\ln k)\ln(k/k_0)+\frac{1}{6}d^2n_s/d\ln k^2\ln(k/k_0)^2+\cdots} \tag{2.16}$$

As mentioned in the introduction, the reigning fiducial model description of the universe today is the ΛCDM model, a six parameter model describing the geometry and matter-energy content in the universe. The fiducial power spectrum C_l is in the simlated maps used in this thesis implemented by running a a "quick" estimation of the ΛCDM spectrum from the observed sky, and generating a set of simulation from the estimated power spectrum. The simulated skies are then run through a set of Full Focal Plane simulation (FFP8 for the 2015 release and the data used in this thesis, described in the Planck data (Ade et al., 2014a)), which creates a modeled version of the *time ordered information*, mimicking the effects introduced in the CMB map from the satellite. The FFP8 simulated data consists of 10 fiducial *mission* realizations of the CMB reduced to 18 144 maps, in addition to 10^4 Monte-Carlo realizations of noise and CMB data reduced to 10^6 maps. On top of the CMB produced from the theoretical model are realizations of the foreground sky, adding effects of contamination from thermal dust, spinning dust, synchrotron and free-free emissions, the cosmic infrared background, radio sources and SZ clusters (Ade et al., 2016a). More details on the FFP8 simulations can be found in (Ade et al., 2016a) and in the explanatory supplement on the in the Planck Legacy Archive [3].

2.3 Estimating the Power Spectrum From Observational Data

The observational data is a stream of time ordered information which we sort into maps through map making algorithms. Doing spherical harmonic transformations on the observed CMB sky we can calculate the power spectrum from observations, defined from the variance of the spherical harmonic coefficients,

$$\langle a_{lm}a_{l'm'}\rangle = \delta_{ll'}\delta_{mm'}C_l. \tag{2.17}$$

In the case of a Gaussian random field (assumed to be the case in the CMB (Ade et al., 2014g)) the average and the variance of the coefficients carry all the statistical information in the map. For the spherical harmonic a_{lm} coefficients the average disappears (Hinshaw et al., 2003), and all information is contained solely in the power spectrum C_l. In the absence of noise and masking, an unbiased estimator limited only by cosmic variance of said power spectrum is given by a simple sum over multipoles (Cahill, 2013) (Hivon et al., 2002),

[3] http://pla.esac.esa.int/pla/#home

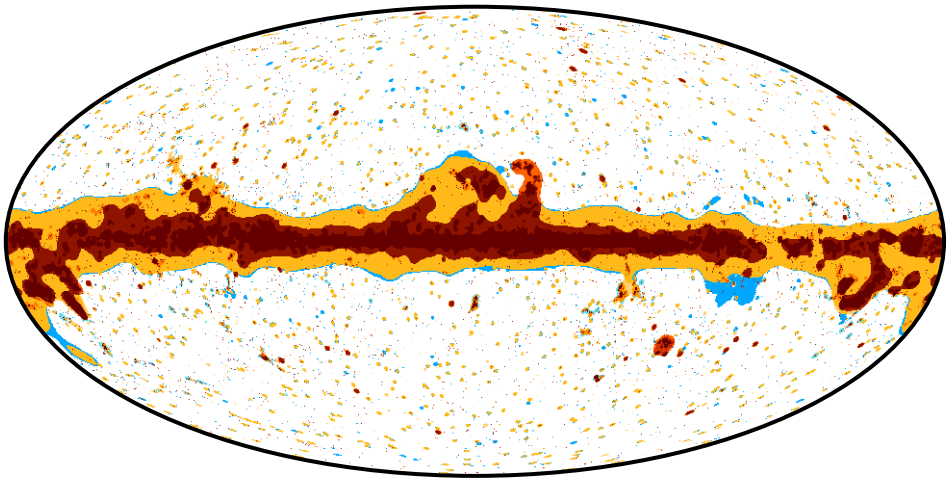

Figure 2.4: Figure showing the different confidence masked produced with each of the four component separation methods used with Planck data, Commander-Ruler (light blue), NILC (dark red), SEVEM (yellow), and SMICA (light red). The union mask of the four, U73, masks all colored pixels from the foreground cleaned map (Ade et al., 2014b).

$$\hat{C}_l = \frac{1}{2l+1} \sum_{m=-l}^{l} a_{lm}^{\mathrm{X}} a_{lm}^{\mathrm{Y}*}. \tag{2.18}$$

Here, X and Y denote the a_{lm} coefficient calculated from two different half-mission maps (Adam et al., 2016). The noise properties these half-mission maps are nearly completely independent, constructed from one half each of the full mission observations made available with the 2015 data release. We use here only the cross power spectrum, not the auto power spectrum. The cross power spectrum has the advantage that it is not biased by the noise in the maps, if the noise between the two maps is uncorrelated (Hinshaw et al., 2003).

Having two maps, one constructed from theoretical models and FFP8, and one observed, we can analyse the difference in properties between the maps to asses the how well the theoretical models really fit the observations. Since the power spectrum of the CMB contain all of it's statitistcial properties, we can use spherical harmonic transformation in order to do this. These are here implemented through the HEALPix , specifically through the `map2alm` and `alm2map` routines. A short description of HEALPix can be found in appendix B, section B.1

Unfortunately the data from observational experiments are contaminated by foregrounds of different kinds, like radiation from the galaxy (e.g CO and thermal dust emission, free-free emission, synchrotron emission) and strong radio and microwave point sources. This means that we have to mask parts of the sky in order to remove both galactic contamination around the galactic plane and point source emission. After the component separation ("foreground cleaning") is performed using one of the four component separation techniques, the remaining residual contamination are masked using a confidence mask, a mask that removes all parts of the sky still believed to be a source of contamination. This mask is included as a simple multiplication, setting the contaminated pixels to 0. The mask used in this thesis is the U73 mask (see figure 2.4), a combination of the confidence masks developed for the 4 different component separation methods used in the Planck data, leaving 73 % of the sky unmasked (Ade et al., 2014b) .

The inclusion of the mask can be easily incorporated into the spherical harmonic transform:

$$\tilde{a}_{lm} = \int T(\theta,\phi)W(\theta,\phi)Y^*_{lm}(\theta,\phi)\sin(\theta)d\theta d\phi, \tag{2.19}$$

where $\tilde{a}_{lm}$ now denotes the *pseudo* spherical harmonics coefficients given by masking the map. This can be approximated as a sum over pixels instead,

$$\tilde{a}_{lm} \approx \Delta_{\rm pix}\sum_{i=0}^{N_{pix}} T(i)W(i)Y^*_{lm}(i), \tag{2.20}$$

where $\Delta_{\rm pix}$ gives the pixel area and i numbers the pixels on the map.

The definition of the power spectrum is still the same as in equation 2.17 with the same estimator as in equation 2.18, but we now have a pseudo power spectrum due to the cut sky, which leads to a corruption of the statistical properties of the map.

$$\tilde{C}_l = \frac{1}{2l+1}\sum_{m=-l}^{l}|\tilde{a}_{lm}|^2. \tag{2.21}$$

This pseudo power spectrum can be related to the underlying power spectrum through their ensemble averages,

$$\langle\tilde{C}_l\rangle = \sum_{l'} M_{ll'}\langle C_{l'}\rangle, \tag{2.22}$$

where $M_{ll'}$ is a mode-mode coupling matrix, describing the coupling occurring between multipoles in a cut sky map where parts of the sky are masked. We use the MASTER code developed as described in (Hivon et al., 2002), where the effects of the mode-mode coupling, beam, pixelation, potential filtering (for example removal of systematics resulting from scanning strategies) and the noise, are included when calculating the ensemble average in equation 2.22,

$$\langle\tilde{C}_l\rangle = \sum_{l'} M_{ll'}F_{l'}B^2_{l'}\langle C_{l'}\rangle + \langle\tilde{N}_{l'}\rangle \tag{2.23}$$

$$= \sum_{l'} K_{ll'}\langle C_{l'}\rangle + \langle\tilde{N}_{l'}\rangle \tag{2.24}$$

Here $B_{l'}$ describes the effect of beam and map pixelation, $F_{l'}$ is the filter transfer function, noise is $\tilde{N}_{l'}$ and $K_{ll'}$ is the kernel denoting the combined effect of the first three. So the estimated underlying power spectrum is a solution composed of several effects, in order to correct for systematics and noise.

The MASTER code bins the slowly varying power spectrum $D_l = C_l(l+1)l/2\pi$ (see figure 2.3), using the binning operator in equation 2.25 for a set of bins $n_{\rm bins}$, indexed by b. This binning is done in order to minimize the oscillations in the power spectrum occurring as a consequence of the coupling between the multipoles, and to reduce the subsequent errors (Hivon et al., 2002).

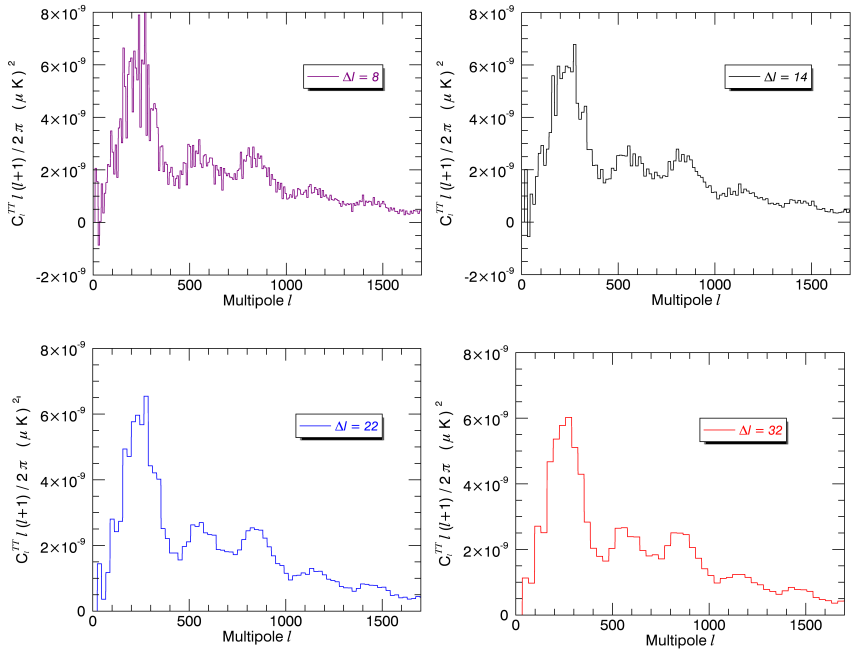

Figure 2.5: Illustrations of the binned spectra created by the MASTER code used in this thesis for three different bin sizes, $\Delta l = 8$, $\Delta l = 14$, $\Delta l = 22$ and $\Delta l = 32$. The power spectra were created using the MASTER algorithm before the split into $N_{\text{side}} = 1$ maps, and therefore valid for the whole masked map.The bin sizes were selected in order to demonstrate the level oscillation occurring from cut sky maps in smaller bin sizes, therefore demonstrating why a binning is helpful when estimating the spectra from data or FFP8 simulations

The power spectrum then becomes $C_b = P_{bl}C_l$, where P_{bl}. We only define the bins as flat band, disjoint bins, but other forms of binning can be implemented in the algorithm. An example of binned power spectra are shown in figure 2.5 for four different bin sizes. As can be seen, the oscillations in the power spectrum are much more prominent for the smallest bin size $\Delta l = 8$ than for the three other plot, with no apparent oscillation in $\Delta l = 32$ other than the acoustic peaks and small oscillations in the silk damping tail also seen in the continuous spectrum shown in 2.3.

The reciprocal binning operator Q_{bl} is given in equation 2.26, where we have shifted the notation to Einstein summation convention [4]. We have kept the notation in order to remain consistent with notation in Hivon et al. (2002).

$$P_{bl} = \begin{cases} \frac{1}{2\pi}\frac{l(l+1)}{l^{b+1}_{\text{low}} - l^{b}_{\text{low}}} & \text{if } 2 \leq l^{b}_{\text{low}} \leq l < l^{b+1}_{\text{low}} \\ 0 & \text{else} \end{cases} \tag{2.25}$$

$$Q_{bl} = \begin{cases} \frac{2\pi}{l(l+1)} & \text{if } 2 \leq l^{b}_{\text{low}} \leq l < l^{b+1}_{\text{low}} \\ 0 & \text{else} \end{cases} \tag{2.26}$$

An unbiased estimate of the binned power spectrum is then given by

$$\hat{C}_b = K_{bb'} P_{b'l} \left(\tilde{C}_l - \langle \tilde{N}_l \rangle \right), \tag{2.27}$$

[4] Repeated indices are summed over (Hivon et al., 2002) (Einstein, 1916)

where $K_{bb'}$ is the binned version of the kernel $K_{ll'}$,

$$K_{bb'} = P_{bl} K_{ll'} Q_{l'b'} = P_{bl} M_{ll'} F_{l'} B^2_{l'} Q_{l'b'} \tag{2.28}$$

Analytical derivations of the coupling kernel $K_{ll'}$ is given in the appendix in Hivon et al. (2002). This kernel $K_{bb'}$ now grants us a fast and easy method to handle the systematics and foregrounds left over after the map has been cleaned using the SMICA method, although it returns a binned power spectrum. For the purposes in this thesis we need to recombine the binned spectrum back to a continuous one. We use a set of different bin sizes, from 8 to 32 with increments of 2, in order to ensure that the results are not tweaked by the choice in binning. The recombining is done by summing the contribution at each multipole from all bin sizes, and weighting the contribution by the variance of the bin size, $\sqrt{N_b}$, creating a variance weighted mean at each multipole l (Ade et al., 2016c). Figure 2.5 shows a set of the different bin sizes. The smallest bin is set to $\Delta l = 8$, and as can be seen in figure 2.5 it still contains noticeable oscillations. Smaller Δl are affected by stronger and stronger oscillations from the multipole coupling, so the smallest bin size is set to $\Delta l = 8$ in order to minimize this effect in the analysis. The highest bin size is set to $\Delta l = 32$, inclusion of power spectrum with larger bin sizes did not affect the results and we conclude therefore that the bigger bin sizes smear out too many details to give more information.

Chapter 3

Dipolar Asymmetry

In 1968 Ehlers, Geren, and Sachs proved the theorem that states "If a family of freely-falling observers measure self-gravitating background radiation to be exactly isotropic, then the Universe is exactly Friedmann-Lemaitre-Robertson-Walker (Ehlers et al., 1968). " The impact of this is that, only in a more or less isotropic universe can the universe accurately be described with a Friedmann-Lemaitre-Robertson-Walker metric, and subsequently be well described by most modern cosmological models. Our universe *is*, as far as observations today show, very close to completely isotropic with very small variations. In addition, the fact that these anisotropies in the background found in the COBE data were as small as the were, showed that the universe is almost Friedmann–Robertson–Walker at the time of last scattering, according to the theorem proven by Stoeger et al. (1995).

Both WMAP and Planck data supported the claim that the universe is isotropic to a factor of 10^{-5}, as well as establishing 6-parameter ΛCDM as the model with the best fit to the data (Spergel et al., 2007) (Ade et al., 2014d). The interesting part is then that the universe is *almost* isotropic, not completely. Within the data they found features that were in tension with the assumption of isotropy (Bennett et al., 2011) (Ade et al., 2016c). The random nature of the CMB allows for some odd features, so with today's resolution and amount of data, it often boils down to calculating the *significance* of the findings. The question is, given simulations generated by completely random processes with parameters and estimations from known physical processes, how "weird" is your observed data? One good example is the apparent presence of Stephen Hawking's initials right above the galactic equator in the WMAP data (figure 3.1), as pointed out by Bennett et. al in (Bennett et al., 2011). Yes it is definitely weird, but when you look for weird things in random data you are bound to find something that looks odd, and it wouldn't be very scientific to reevaluate our cosmological framework simply because some oddly shaped clusters of over and under densities. Many scholars still contend that the detected anomalies most likely do not point towards some form of new physics (Bennett et al., 2011) (Ade et al., 2016c).

The presence of a dipolar asymmetry across large and/or nonadjacent multipole ranges means that the power of fluctuations in one half of the sky is stronger than the other, meaning that no matter what size scales you view, large or small, the amplitude of the fluctuations across the map is stronger on one half. This in turn indicates that the gravitational wells are deeper on one half of the sky, which should have implications structure formation. Finally it means that the universe in essence does *not* look the same no matter what direction you look, and structures in

one part of the sky would appear to be bigger. The detection of this asymmetry can therefore be done with different data than just the CMB, and in order to know with some semblance of certainty whether the detection in the random generated fluctuations on the sky really point to new physics or if they are simple products of said random nature, we need to cross-check the findings in the CMB with other types of observations (e.g. quasars, structure formations, sky surveys). Still, the detection in the CMB is curious.

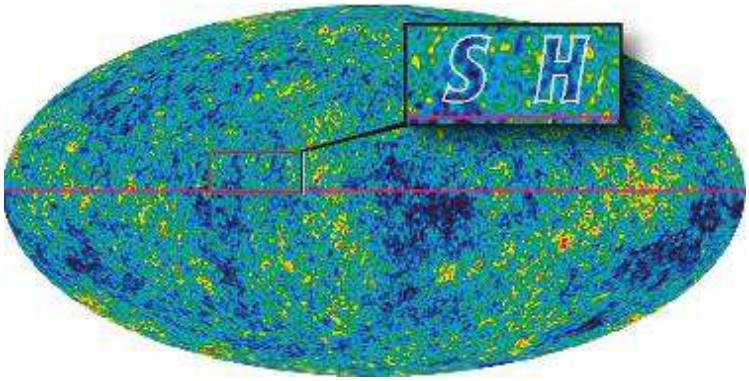

Figure 3.1: Stephen Hawkings initials found just above the galactic equator in WMAP data Bennett et al. (2011)

3.1 High-*l* Hemispherical Power Asymmetry

The apparent dipolar asymmetry in the CMB was first discovered in the WMAP data using both an N-point correlation function (Eriksen et al., 2004), power spectrum analysis in a similar way as we do here (Eriksen et al., 2004), and the genus statistics (Park, 2004). Since then, the investigation of hemispherical asymmetry has been split into many different parts and approaches (Ade et al., 2016c). In order to give proper context to the methods developed in this thesis, we will go through the main points of the angular clustering approach, or high-*l* asymmetry as it is sometimes called, as described in more details in section 6.5 in Ade et al. (2016c), section 5.5 in Ade et al. (2014f) and in Axelsson et al. (2013). We are building on the methods used to calculate the angular clustering of the dipolar distributions of power across the multipole range $l = 2 - 1500$ and comparing this clustering to 2500 simulations based on the fiducial ΛCDM model. The subsequent goal is then to generalize the method to higher multipoles in order to see if we find the same clustering with a quadrupolar or octopolar distribution.

In order to reproduce the dipolar investigation we split the sky map into 12 pieces defined by the HEALPix $n_{\rm side} = 1$ map (Gorski et al., 2005) and calculate the power spectrum in each separate patch on the sky. An example of a CMB map construced from the first 1000 multipoles from the power spectrum included in the HEALPix package is shown in figure 3.2, where everything but the third pixel is masked out. This is implemented using the MASTER algorithm as described in section 2.3, returning the binned spectrum described above. We mask the map using the U73 mask and then a mask with only one $n_{\rm side} = 1$ patch of value 1, the rest set to 0. Since the spherical harmonics transform is a sum over all contributions to the transform this formalism ensures that when an entire map is transformed using the `map2alm` procedure in HEALPix , only the $N_{\rm side} = 1$ patch left unmasked will contribute to the a_{lm} coefficients and the resulting power spectrum will be valid only for that patch of the sky. Doing this for all patches of the sky results in 12 different power spectrum, one for each patch, and this way we can compare the

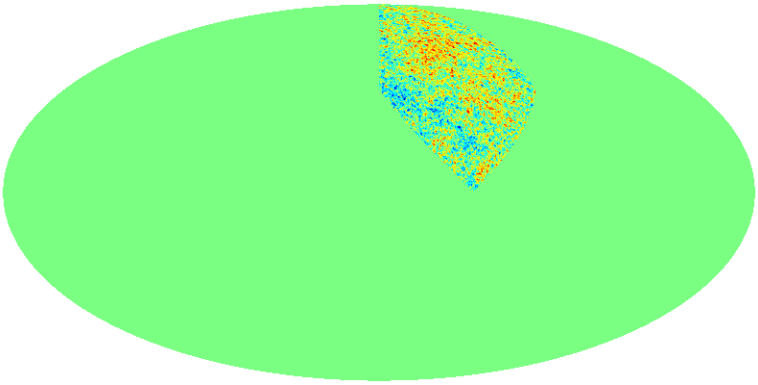

Figure 3.2: Example of a CMB map with structures up to $l = 1000$, masked by a $N_{\text{side}} = 1$ map upgraded to the same resolution, with every pixel except the third $N_{\text{side}} = 1$ pixel set to 0. The underlying map was constructed from the 1000 first multipoles of the power spectrum provided in the HEALPix package.

power of the anisotropies across the sky for all multipoles above $l = 2$ included in the power spectrum. Using $l_{\text{max}} = 1500$ we are then left with 1500 $n_{\text{side}} = 1$ maps for the data and each of the simulations, one map for each multipole l. we then recombine these into a continuous spectrum as described in section 2.3. A set of maps for some selected multipoles is shown in figure 3.3.

As might become apparent from the maps illustrated in figure 3.3, it is difficult to be able to discern a multipole distribution by eye in maps with such a low resolution, but the maps do contain enough information to enable us to extract spherical harmonic coefficients up to $l = 2$, the quadrupole. This can be seen by considering the fact that from the relation between angular size of the details included in a map and multipole l, $\Delta\Phi_l = 180^\circ/l = \pi/l$. Since a map resolution only resolves details down to $\Delta\theta = \sqrt{\pi/(3N_{\text{side}}^2)}$ (see the section on HEALPix in B.1), only angular details smaller or equal to this limit can be regained from a map of N_{side} resolution. We have an *ideal* lower limit to the map resolution needed for a given N_{side},

$$\Delta\Phi \geq \Delta\theta \quad \rightarrow \quad \frac{\pi}{l} \geq \sqrt{\frac{\pi}{3N_{\text{side}}^2}} \quad \rightarrow \quad N_{\text{side}} \geq \frac{l}{\sqrt{3\pi}}. \tag{3.1}$$

So approximately we need N_{side} greater than $l/3$.

We also need to consider how many spherical harmonic coefficients would be needed to faithfully recreate a map. If the map contains $N_{\text{pix}} = 12N_{\text{side}}^2$ data points, we would need $12N_{\text{side}}^2$ spherical harmonic coefficients in order to avoid information loss. For each multipole l we have $2l + 1$ coefficients, so up to a multipole l we have N_a spherical harmonic coefficients given as

$$N_a = \sum_{l=0}^{l_{\text{max}}} (2l + 1) = (l_{\text{max}} + 1)^2. \tag{3.2}$$

We need a number of pixels equal to or greater than N_a in order to resolve details down to a given l_{max}:

$$N_a = (l_{\text{max}} + 1)^2 \leq 12N_{\text{side}}^2 \quad \longrightarrow \quad l_{\text{max}} \leq \sqrt{12}N_{\text{side}} - 1 \approx 2.5N_{\text{side}}. \tag{3.3}$$

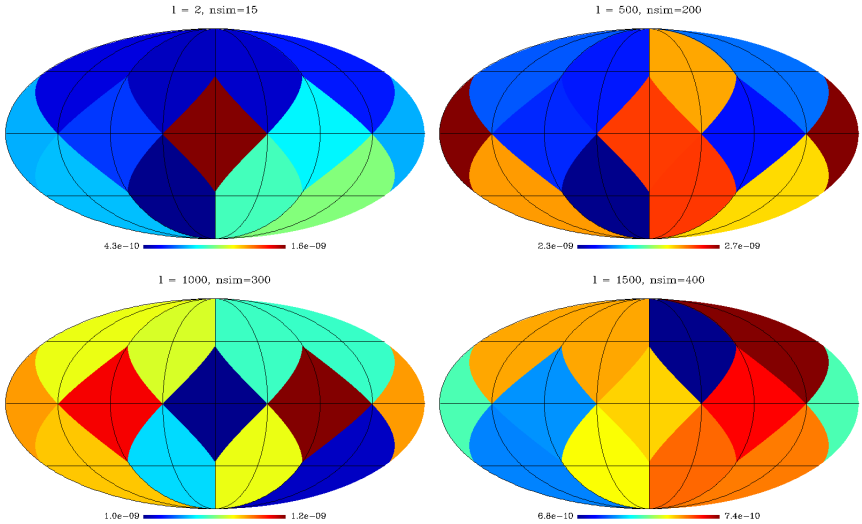

Figure 3.3: A selection of $N_{\text{side}} = 1$ maps showing the strength of the fluctuations in each pixel patch for a given multipole l, for different simulations. "Simulation number" 15 gives the power spectrum calculated from the data, the other were created from ffp6 simulations.

This means that in order to recreate a map faithfully from the spherical harmonics we need an N_{side} of at least $l_{\text{max}}/2.5$ to be maintain the amount of information. As a rule of thumb we can calculate the spherical harmonic coefficients of a map with high precision up to $l_{\text{max}} \approx 2N_{\text{side}}$. For higher multipoles the information is gradually lost due to pixelation effects untill we reach $l_{\text{max}} = 3N_{\text{side}}$ where we can no longer gain more information. So for $N_{\text{side}} = 1$ we can resolve a_{lm} coefficients up to $l_{\text{max}} = 2$ without information loss or loss of precision.The maps shown in figure 3.3 do therefore contain enough information to enable ut so extract both the dipole and the quadrupole. In the octopole case we need to move to $N_{\text{side}} = 2$ in order to ensure a high enough resolution.

In the procedures used in Ade et al. (2016c), Ade et al. (2014f) and Axelsson et al. (2013), the maps are calibrated by the standard deviation calculated for each map at each multipole using the 500 simulations. The `remove_dipole*` routine is then used to find a direction estimate for the dipolar component of the power spectrum maps for each multipole. This routine returns the coordinate direction of the estimated dipole as well as removing the dipole component from the map, and a statistics is then developed to analyze the mean separation between these coordinates. It can be shown that the angular distance between two coordinates (θ_1, ϕ_1) and (θ_2, ϕ_2) can be expressed as

$$\cos(\Delta\theta) = \cos(\theta_1)\cos(\theta_1) + \sin(\theta_1)\sin(\theta_2)\cos(\phi_1 - \phi_2). \tag{3.4}$$

In Ade et al. (2016c) the mean separation angle between the dipole directions was kept as the $\cos(\Delta\theta)$ (instead of $\Delta\theta$) in order to keep the statistics closer to the Rayleigh statistics used in a similar analysis in section 6.6 of Ade et al. (2016c). For consistency we will stick to this notation here.

The pseudo Rayleigh statistic [1] is then constructed as a mean of all angular distances up to a

[1] We chose to call it pseudo Rayleigh simply because it is denoted Rayleigh statistic in Ade et al. (2016c), but it is not exactly a Rayleigh statistic since the amplitude information is disregarded

certain l_{lim},

$$RS_{l_{\text{lim}}} = \sum_{l=2}^{l_{\text{lim}}} \frac{\cos(\Delta\theta_l)}{l_{\text{lim}} - 1}. \tag{3.5}$$

This is done for all values of l_{lim} from 2 up to a given $l_{\text{max}} = 1500$. If the CMB is isotropic as assumed in the fiducial model, the dipolar directions of these components should display a more or less random nature with dipole directions pointing in random directions across the sky. Averaged over many simulation, we should have a mean separation angle of the directions of around 90°. With random generated data we would expect some clustering of the dipole component directions, but how clustered is the observational data compared to the simulations?

A p-value is then defined as the fraction of simulations that exhibit a mean separation angle smaller than the one observed in the data between all multipoles. The result published in Ade et al. (2016c) is shown in figure 3.4. The top image shows the estimated dipole directions averaged over bins of approximately 100 multipoles from $l = 2 - 1500$ and the bottom image shows the above-mentioned p-values. A smaller p-value means a more statistically significant result, and as concluded in Ade et al. (2016c), the plot of p-values shows a significant clustering for most multipoles above $l \sim 200$. The dotted line in the significance plot indicates the limit at which we evaluate the significance as strong or not. A p-value of about 0.5 % ($p = 0.005$), less than 0.05% of the simulations have a clustering as strong as the data. We will continue to use this limit for significance throughout the thesis. Any significance said to be strong or noticeable is below $p = 0.005$.

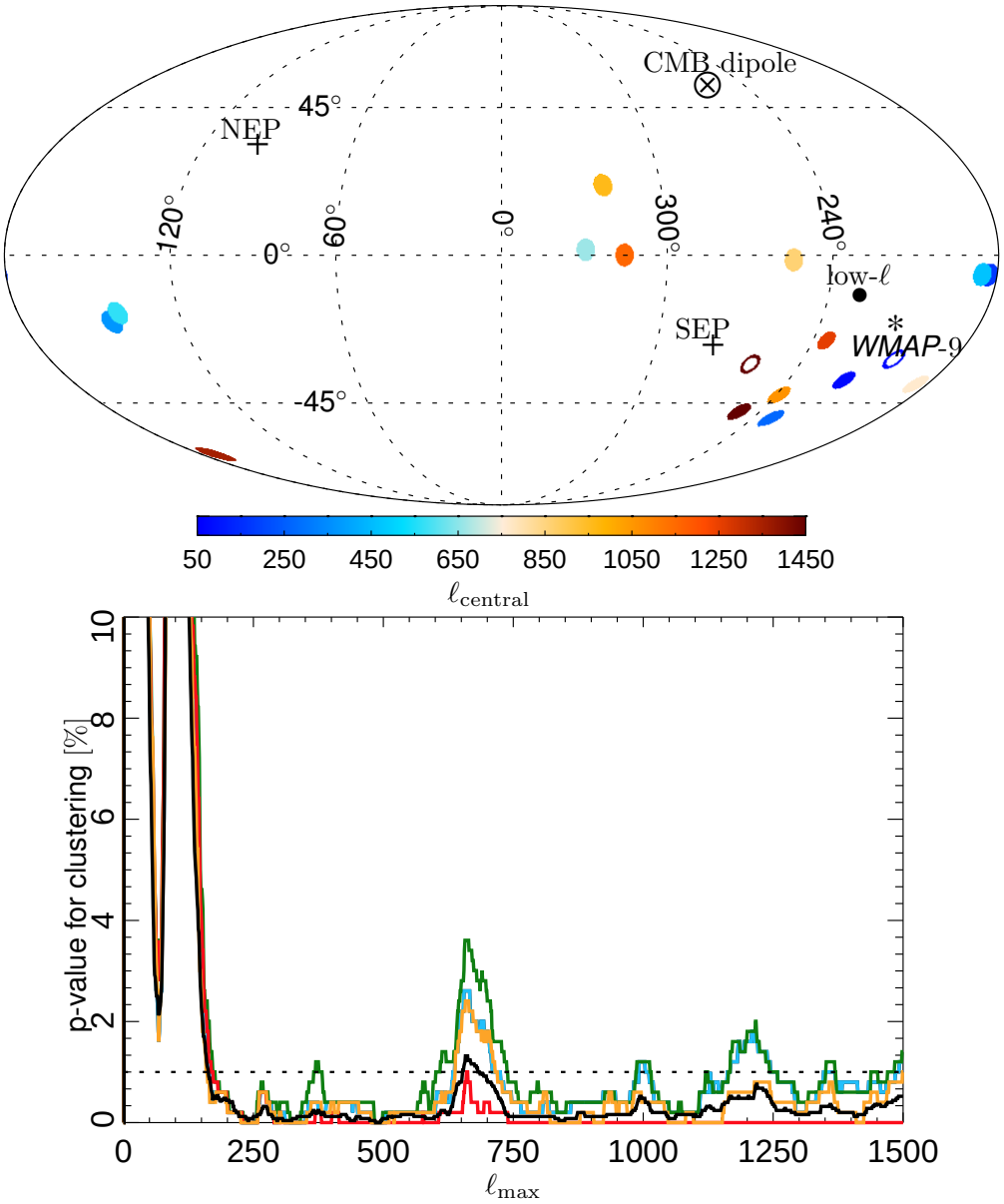

Figure 3.4: Figures found in Ade et al. (2016c) Top: Map showing the estimated dipole direction of the power asymmetry found in Ade et al. (2016c), averaged for multipole ranges (color-coded). The best estimated average direction from WMAP is shown as an asterix ($*$) and the CMB dipole component is shown as a $\otimes$. The direction marked with low-l (∞) gives the preferred direction of the dipolar modulation model of the hemispherical asymmetry. Bottom: Derived p-values for the angular clustering of the power distribution in the top figure as a function of $l_{\rm max}$, determined for the four different foreground cleaned maps, Commander (red), NILC (orange), SEVEM (green), and SMICA (blue), based on 500 simulations. For one of the maps (SMICA), the p-values based on 2500 simulations are also shown (black). The p-values are based on the fraction of simulations Rayleigh statistic (see Ade et al. (2016c)), determined for each multipole l, compared to the data. The results shown here have been marginalized over bin sizes in the range $\Delta l = 8$ to $\Delta l = 32$.

Chapter 4

Quadrupolar & Octopolar Asymmetry

The detection of angular clustering presented in Ade et al. (2016c) is a detection across all multipole ranges, as well as nonadjacent ranges. This can be seen from table 26 and figure 37 in the Planck 2015 isotropy article (Ade et al., 2016c). In the estimation of the significance shown in figure 3.4 the lowest multipole was set to $l = 2$. This estimation resulted in a noticeable significance in the data, compared to the simulations. Still, this might be the result of low-l asymetry affecting the high-l result, due to the cumulative nature of the Rayleigh statistic (given in equation 3.5). When setting the lowest multipole to $l = 200$ instead of 2, the mean of the significance (averaged over all multipoles) is significantly weaker, at 1.52 % as opposed to < 0.04 %. This indicate that the clustering does not only occur between multipoles in the same range, but between the multipole ranges $l < 200$ and $l > 200$ as well, effectively ruling out dipolar modulation in one specific multipole range as a fitting model of the clustering. The detection is therefore an indication that there may be features that are in breach with the assumption of isotropy that affect both large and smaller structures. A natural next step would then be to see whether this apparent breach also manifests in octopolar or quadrupolar form, but in order to do this we need to 1) generalize the `remove_dipole` code from the HEALPix package, and 2) define some sort of direction for quadrupole and octopole map or find some other way to see if the distribution of power across the sky are distributed in a similar quadrupole or octopole distribution. In order to get step 1. out of the way, it is necessary to take a closer look at precisely how the direction is estimated in the `remove_dipole` routine.

4.1 Extracting the Dipole Component from a Masked Map

As mentioned earlier, extracting the underlying a_{lm} coefficients from a masked map is non-trivial. Transforming a masked and unmasked version of the same map would yield two different sets of spherical harmonic coefficients, so we need to take the masking into account. An example of the difference in coefficients between a masked and unmasked version of the same map is included in table 4.1 showing the first 10 multipoles in the maps. The map is generated using the power spectrum included in HEALPix . As can be seen, even with only one decimal number, the difference is obvious.

One way to correct for this effect is to use the spherical harmonic transform of a map as defined in equation 2.2, and expand on the discrete form in equation 2.20 for the pseudo a_{lm},

l,m	m = 0	m = 1	m = 2	m = 3	m = 4	m = 5	m = 6	m = 7	m = 8	m = 9	m = 10
l=2	(34.1, 0.0) (36.9, 0.0)	(13.2, -20.9) (12.8, -19.5)	(-6.2, 7.9) (-5.7, 4.5)								
l=3	(1.1, 0.0) (1.5, 0.0)	(0.1, -11.9) (-2.2, -7.9)	(-26.4, 30.5) (-22.9, 28.1)	(14.8, 7.6) (10.1, 3.6)							
l=4	(54.1, 0.0) (47.3, 0.0)	(4.5, -2.2) (4.3, -3.0)	(3.5, 4.8) (1.1, 8.0)	(-7.7, -21.9) (-7.7, -21.1)	(-8.7, -1.0) (-1.1, -3.0)						
l=5	(-20.0, 0.0) (-18.9,0.0)	(-11.0, 3.1) (-7.4, 0.2)	(-11.8, -1.2) (-12.5, 0.4)	(-0.5,-3.9) (2.5, -1.6)	(7.3, -16.3) (5.5, -16.6)	(-16.4, -11.3) (-8.0, -9.5)					
l=6	(-12.1, 0.0) (-6.4, 0.0)	(0.1, -12.3) (0.6, -10.4)	(-0.8, -0.3) (1.6, -3.9)	(10.5, -8.9) (9.4, -8.7)	(-0.1, -4.7) (-3.5, -5.5)	(-0.7, 4.3) (0.0, 3.1)	(-4.6, 4.5) (-4.9, -2.4)				
l=7	(-20.5, 0.0) (-20.4, 0.0)	(8.7, -1.4) (4.5, 1.5)	(5.5, 2.1) (4.7, 0.5)	(4.2, -8.4) (1.3, -10.8)	(-12.9, 4.5) (-12.3, 5.9)	(-3.9, -6.2) (-8.8, -5.5)	(-8.6, -5.4) (-9.2, -6.0)	(-9.2, -1.6) (-3.9, -0.1)			
l=8	(-0.6, 0.0) (-4.0, 0.0)	(1.9, -2.3) (1.5, -3.2)	(1.5, -7.1) (0.9, -3.6)	(-4.0, -3.2) (-1.4, -3.7)	(-13.3, 0.5) (-9.1, 1.8)	(6.1, -2.5) (5.7, -2.4)	(0.7, -10.3) (0.9, -5.5)	(0.0, -5.0) (1.8, -1.0)	(3.0, 9.5) (1.6, 4.3)		
l=9	(2.8, 0.0) (1.6, 0.0)	(-4.7, 4.7) (-1.0, 2.6)	(-0.8, -1.2) (0.2, 0.0)	(7.5, -10.0) (9.5, -7.1)	(3.5, 6.9) (3.7, 5.5)	(1.3, -2.0) (3.6, -3.0)	(1.4, -0.2) (3.7, -1.2)	(-2.1, 1.0) (-2.4, 0.4)	(3.5, 1.6) (-0.9, 3.3)	(0.3, 0.8) (0.8, -0.7)	
l=10	(-5.7, 0.0) (-3.6, 0.0)	(-3.2, -5.6) (-1.9, -4.6)	(1.0, 1.2) (1.4, -1.7)	(1.2, -9.7) (-2.7, -9.6)	(8.6, -0.8) (4.1, -1.3)	(-2.5, 3.0) (-1.7, 2.5)	(9.2, 3.1) (7.2, 0.1)	(0.3, 2.4) (-1.4, -0.1)	(0.9, 0.4) (1.6, 3.1)	(-4.2, -7.0) (-2.3, -5.0)	(10.3, -15.1) (2.7, -10.0)

Table 4.1: Table comparing the spherical harmonic coefficients resulting from a masked (bottom number in each box) and unmasked (top number) version of the same map. The map was created from the power spectrum included in the HEALPix package, transformed to a_{lm} coefficients up to $l = 100$, which are then transformed to a map, with one version masked by the U73 mask. Each map is then transformed back to spherical harmonic coefficients. The two maps are shown in figure 4.1

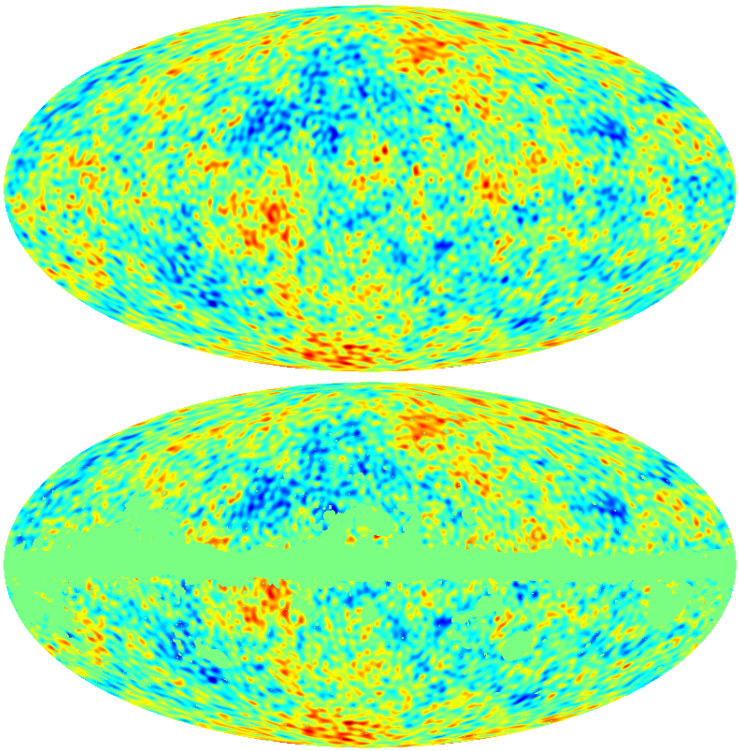

Figure 4.1: Masked and unmasked map used when producing the spherical harmonics coefficients listed in table 4.1. The masked used is the U73 masked, the confidence mask produced for any of the four different component separation techniques given in Ade et al. (2014b). They are created from the first 100 power spectrum elements given in the HEALPix package, using the `create_alm` and `alm2map` routines.

$$\tilde{a}_{lm} = \Delta_{\text{pix}} \sum_{k=0}^{N_{\text{pix}}} M_k Y_{lm}^{k*} T_k. \tag{4.1}$$

Here, Δ_{pix} is the pixel area, M_k is the masking of pixel k and the sum runs over all k pixels in the map. Now, transforming the map T_k using another set of spherical harmonic coefficients $T(\theta, \phi) = \sum_{l'm'} a_{l'm'} Y_{l'm'}^k$,

$$\tilde{a}_{lm} = \Delta_{\text{pix}} \sum_k M_k Y_{lm}^{k*} \sum_{l'm'} a_{l'm'} Y_{l'm'}^k. \tag{4.2}$$

This is a matrix equation that can be solved for the underlying spherical harmonic coefficients, $a_{l'm'}$, from the pseudo coefficient $\tilde{a}_{lm}$.

This matrix equation is used in the `remove_dipole*` routine in HEALPix , but they exploit the similarities between the spherical coordinate transform of the Cartesian coordinates (equation 4.3) and the spherical harmonics Y_{lm}.

$$x = r \sin\theta \cos\phi, \qquad y = r \sin\theta \sin\phi, \qquad z = r \cos\theta \tag{4.3}$$

Since the spherical harmonic coefficients of the CMB for $l = 1$ contain all information of the dipole component of the map, we can use the spherical harmoncis to find a direction for the dipole, defined as the position of the maxima in the map (or the "north pole"). Looking at the dipole components in equations 2.4 - 2.12 we see that the Y_{lm} for $l = 1$ can be expressed using Cartesian coordinate. The same can be done with spherical harmonic coefficients a_{lm} by writing out the integral given in equation 2.2, using the mathematical form of the dipole in $D(\theta, \phi)$ (equation 3.4).

$$a_{lm} = \int D(\theta, \phi) Y_{lm}^*(\theta, \phi) \sin(\theta) d\theta d\phi$$

where $D(\theta, \phi) = A\Big[\cos(\theta_p)\cos(\theta) + \sin(\theta_p)\sin(\theta)\cos(\phi_p - \phi)\Big]$, and (θ_p, ϕ_p) is the coordinate for the global maximum in the dipole. This coordinate is defined as the direction of the dipole, and the alignments results and clustering described in the thesis is defined by the angular distance between these directions. The detailed calculations of these transformations to coordinates is shown in the appendix A, giving the results in equations 4.4 - 4.6. Following from the normalization and orthogonality of the spherical harmonic functions $Y_{lm}(\theta, \phi)$ it can be shown that $Y_{l-m} = (-1)^m Y_{lm}^*(\theta, \phi)$, and subsequently the same holds for the spherical harmonic coefficients, $a_{l-m} = (-1)^m a_{lm}^*$, where a_{lm}^* denotes the complex conjugate of a_{lm}. Using this identity$a_{1-1} = -a_{11}^*$, and the resulting expressions are

$$a_{10} = 2A\sqrt{\frac{\pi}{3}}\cos\theta_p \tag{4.4}$$

$$a_{11} = -A\sqrt{\frac{2\pi}{3}}\sin\theta_p\cos\phi_p + iA\sqrt{\frac{2\pi}{3}}\sin\theta_p\sin\phi_p \tag{4.5}$$

$$a_{1-1} = A\sqrt{\frac{2\pi}{3}}\sin\theta_p\cos\phi_p + iA\sqrt{\frac{2\pi}{3}}\sin\theta_p\sin\phi_p. \tag{4.6}$$

Using the spherical coordinate transform of Cartesian coordinates given in equation 4.3 we find a relation between Cartesian coordinates and spherical harmonic coefficients, giving the direction of the dipole as

$$z_p = \frac{a_{10}}{2}\sqrt{\frac{3}{\pi}}, \qquad y_p = \mathcal{I}\{a_{11}\}\sqrt{\frac{3}{2\pi}}, \qquad x_p = -\mathcal{R}\{a_{11}\}\sqrt{\frac{3}{2\pi}}, \tag{4.7}$$

where x_p, y_p and z_p are the cartesian coordinate of the maxima of the dipole. The same can be done for the spherical harmonics:

$$x \sim \mathcal{R}\{Y_{11}\}, \qquad y \sim \mathcal{I}\{Y_{11}\}, \qquad z \sim Y_{10}.$$

Rewriting the expressions for coefficients and harmonics like this, the `remove_dipole` routine solves the matrix equation in 2.20 as a matrix equation over coordinates,

$$\begin{pmatrix} 1 \\ x' \\ y' \\ z' \end{pmatrix} = \sum_{k=0}^{N_{\rm pix}} M_k \begin{pmatrix} 1 & x^k & y^k & z^k \\ x^k & x^k x^k & x^k y^k & x^k z^k \\ y^k & y^k x^k & y^k y^k & y^k z^k \\ z^k & z^k x^k & z^k y^k & z^k z^k \end{pmatrix} \begin{pmatrix} 1 \\ x \\ y \\ z \end{pmatrix} \tag{4.8}$$

where the coordinates denoted as marked, x', y' and z' describes the masked dipole and the unmarked coordinates describes the underlying, unmasked dipole. The zero'th element in this matrix returns the average temperature in the map (monopole), and the length of the vector $r = \sqrt{x^2 + y^2 + z^2}$ gives the amplitude of the dipole, denoted A in the expression for the dipole map. Our methods are based on this routine, but in generalizing this to higher multipoles, the Cartesian vector notation used in `remove_dipole*` becomes very unintuitive, and a shift to spherical harmonic space is required. In our routine we expand on the expression given in equation 4.1 without moving to pixel space.

4.2 Extending the `remove_dipole` code to higher multipoles

In expanding to higher multipoles it is helpful to write out some of the terms in the spherical harmonics in order to more easily see the form of the matrix, especially for implementation.

$$\begin{aligned}\tilde{a}_{lm} &= \sum_{k=0}^{N_{\rm pix}} \Delta_{\rm pix} M_k Y^{k*}_{lm} T_i \\ &= \sum_k \Delta_{\rm pix} M_k Y^{k*}_{lm} \sum_{l'm'} a_{l'm'} Y^k_{l'm'} \\ &= \sum_k \Delta_{\rm pix} M_k Y^{k*}_{lm} [a_{00} Y^k_{00} + a_{10} Y^k_{10} + a_{1-1} Y^k_{1-1} + a_{11} Y^k_{11} + a_{20} Y^k_{20} \\ &\quad + a_{21} Y^k_{21} + a_{22} Y^k_{22} + a_{2-1} Y^k_{2-1} + a_{2-2} Y^k_{2-2}] \end{aligned} \tag{4.9}$$

Using the relation between negative and positive phase multipoles m given in the section above we can rewrite some of the terms in the expression above,

$$\begin{aligned} a_{1-1}Y_{1-1} + a_{11}Y^k_{11} &= (-1)^{-1} a^*_{11} (-1)^{-1} Y^{k*}_{11} + a_{11} Y^k_{11} = 2a^r_{11}\mathcal{R}\{Y_{11}\} - 2a^i_{11}\mathcal{I}\{Y_{11}\} \\ a_{2-1}Y_{2-1} + a_{21}Y^k_{21} &= (-1)^{-1} a^*_{21} (-1)^{-1} Y^{k*}_{21} + a_{21} Y^k_{21} = 2a^r_{21}\mathcal{R}\{Y_{21}\} - 2a^i_{21}\mathcal{I}\{Y_{21}\} \\ a_{2-2}Y_{2-2} + a_{22}Y^k_{22} &= (-1)^{-2} a^*_{22} (-1)^{-2} Y^{k*}_{22} + a_{22} Y^k_{22} = 2a^r_{22}\mathcal{R}\{Y_{22}\} - 2a^i_{21}\mathcal{I}\{Y_{22}\} \end{aligned}$$

With these new rearranged terms we can split everything in equation 4.9 into real and imaginary parts,

$$\begin{aligned}\tilde{a}_{lm} = \sum_k \Delta_{\rm pix} M_k Y^{k*}_{lm} [a_{00} Y^k_{00} + a_{10} Y^k_{10} + 2a^r_{11}\mathcal{R}\{Y_{11}\}^k - 2a^i_{11}\mathcal{I}\{Y_{11}\}^k + a_{20} Y^k_{20} \\ + 2a^r_{21}\mathcal{R}\{Y_{21}\}^k - 2a^i_{21}\mathcal{I}\{Y_{21}\}^k + 2a^r_{22}\mathcal{R}\{Y_{22}\}^k - 2a^i_{22}\mathcal{I}\{Y_{22}\}^k] \end{aligned} \tag{4.10}$$

where we for brevity denote the real and imaginary part of a_{lm} as a^r_{lm} and a^i_{lm} respectively. The same is done for the pseudo spherical harmonic coeficients, $\tilde{a}_{lm}$. Keeping in mind the relation $a_{l-m} = (-1)^m a^*_{lm}$, we only need to perform this for the positive values of the multipoles m. The full calculations are given in appendix A, section A.2, resulting in the matrix equation given in 4.11. Here $\Delta_{\rm pix}$ denotes the area of each HEALPix pixel (see appendix B, section B.1 for details on the HEALPix package), and M_k denotes the mask in pixel k. The full form of the matrix is given in 4.12.

$$\begin{pmatrix} \tilde{a}_{00} \\ \tilde{a}_{10} \\ \tilde{a}^r_{11} \\ \tilde{a}^i_{11} \\ \tilde{a}_{20} \\ \tilde{a}^r_{21} \\ \tilde{a}^i_{21} \\ \tilde{a}^r_{22} \\ \tilde{a}^i_{22} \end{pmatrix} = \sum_k \Delta_{\rm pix} M_k R^k_{ll'mm'} \begin{pmatrix} a_{00} \\ a_{10} \\ a^r_{11} \\ a^i_{11} \\ a_{20} \\ a^r_{21} \\ a^i_{21} \\ a^r_{22} \\ a^i_{22} \end{pmatrix} \tag{4.11}$$

$$R^k_{lml'm'} = \begin{pmatrix} (Y^k_{00})^2 & Y^k_{10}Y^k_{00} & 2Y^{rk}_{11}Y^k_{00} & -2Y^{ik}_{11}Y^k_{00} & Y^k_{20}Y^k_{00} & 2Y^{rk}_{21}Y^k_{00} & -2Y^{ik}_{21}Y^k_{00} & 2Y^{rk}_{22}Y^k_{00} & -2Y^{ik}_{22}Y^k_{00} \\ Y^k_{00}Y^k_{10} & (Y^k_{10})^2 & 2Y^{rk}_{11}Y^k_{10} & -2Y^{ik}_{11}Y^k_{10} & Y^k_{20}Y^k_{10} & 2Y^{rk}_{21}Y^k_{10} & -2Y^{ik}_{21}Y^k_{10} & 2Y^{rk}_{22}Y^k_{10} & -2Y^{ik}_{22}Y^k_{10} \\ Y^k_{00}Y^{rk}_{11} & Y^k_{10}Y^{rk}_{11} & 2\left(Y^{rk}_{11}\right)^2 & -2Y^{ik}_{11}Y^{rk}_{11} & Y^k_{20}Y^{rk}_{11} & 2Y^{rk}_{21}Y^{rk}_{11} & -2Y^{ik}_{21}Y^{rk}_{11} & 2Y^{rk}_{22}Y^{rk}_{11} & -2Y^{ik}_{22}Y^{rk}_{11} \\ -Y^k_{00}Y^{ik}_{11} & -Y^k_{10}Y^{ik}_{11} & -2Y^{rk}_{11}Y^{ik}_{11} & 2\left(Y^{ik}_{11}\right)^2 & -Y^k_{20}Y^{ik}_{11} & -2Y^{rk}_{21}Y^{ik}_{11} & 2Y^{ik}_{21}Y^{ik}_{11} & -2Y^{rk}_{22}Y^{ik}_{11} & 2Y^{ik}_{22}Y^{ik}_{11} \\ Y^k_{00}Y^k_{20} & Y^k_{10}Y^k_{20} & 2Y^{rk}_{11}Y^k_{20} & -2Y^{ik}_{11}Y^k_{20} & (Y^k_{20})^2 & 2Y^{rk}_{21}Y^k_{20} & -2Y^{ik}_{21}Y^k_{20} & 2Y^{rk}_{22}Y^k_{20} & -2Y^{ik}_{22}Y^k_{20} \\ Y^k_{00}Y^{rk}_{21} & Y^k_{10}Y^{rk}_{21} & 2Y^{rk}_{11}Y^{rk}_{21} & -2Y^{ik}_{11}Y^{rk}_{21} & Y^k_{20}Y^{rk}_{21} & 2\left(Y^{rk}_{21}\right)^2 & -2Y^{ik}_{21}Y^{rk}_{21} & 2Y^{rk}_{22}Y^{rk}_{21} & -2Y^{ik}_{22}Y^{rk}_{21} \\ -Y^k_{00}Y^{ik}_{21} & -Y^k_{10}Y^{ik}_{21} & -2Y^{rk}_{11}Y^{ik}_{21} & 2Y^{ik}_{11}Y^{ik}_{21} & -Y^k_{20}Y^{ik}_{21} & -2Y^{rk}_{21}Y^{ik}_{21} & 2\left(Y^{ik}_{21}\right)^2 & -2Y^{rk}_{22}Y^{ik}_{21} & 2Y^{ik}_{22}Y^{ik}_{21} \\ Y^k_{00}Y^{rk}_{22} & Y^k_{10}Y^{rk}_{22} & 2Y^{rk}_{11}Y^{rk}_{22} & -2Y^{ik}_{11}Y^{rk}_{22} & Y^k_{20}Y^{rk}_{22} & 2Y^{rk}_{21}Y^{rk}_{22} & -2Y^{ik}_{21}Y^{rk}_{22} & 2\left(Y^{rk}_{22}\right)^2 & -2Y^{ik}_{22}Y^{rk}_{22} \\ -Y^k_{00}Y^{ik}_{22} & -Y^k_{10}Y^{ik}_{22} & -2Y^{rk}_{11}Y^{ik}_{22} & 2Y^{ik}_{11}Y^{ik}_{22} & -Y^k_{20}Y^{ik}_{22} & -2Y^{rk}_{21}Y^{ik}_{21} & 2Y^{ik}_{21}Y^{ik}_{22} & -2Y^{rk}_{22}Y^{ik}_{22} & 2\left(Y^{ik}_{22}\right)^2 \end{pmatrix} \tag{4.12}$$

Here, we have denoted $\mathcal{R}\{Y_{lm}\}$ and $\mathcal{I}\{Y_{lm}\}$ as Y^r_{lm} and Y^i_{lm} in order to save enough space to be able to show the entire matrix on a single page.

This matrix is diagonal with a "θ - symmetric" mask, that is if the mask is a simple band around the equator with no ϕ-dependence. This can be seen from the integral in equation 2.2. Having a mask that is only dependent on theta does not affect the phase of the spherical harmonic coefficients and thus only result in a factor in the coefficients. The matrix above would therefore be completely diagonal and trivial to solve. For all other masks, this is not the case, and a matrix equation algorithm is needed in order to solve equation 4.11. We have used the Singular Value Decomposition method also used in `remove_dipole`. A short description of the method is given in appendix B, section B.2.

4.2.1 Octopole Components

With the form of the matrix equation in 4.1, it should be obvious that a generalization to higher multipoles is trivial. In this thesis we only do this generalization for the octopole, which means including 7 more elements in the a_{lm}-vectors and 175 elements in the A_{lm} matrix in 4.12. Considering the simple generalization and the size of the resulting equations and matrix, we do not write out the octopole matrix here, only a slightly expanded form of the matrix equation in 4.1, shown in equation 4.13. These two matrix equations in 4.11 and 4.13 form the basis of all results produced in this thesis.

The good thing about having the matrix on this form is that it is very simple to implement. Tedious, but simple. Two vectors can be created, one containing the conjugated real and imaginary elements of Y^*_{lm} in equation 4.10, and one containing the factors and elements of $Y_{l'm'}$ in the paranthesis on the right hand side in equation 4.10. Both of these vectors are trivially generalized to higher multipole with the addition of $Y_{l0}, Y^r_{l1}, -Y^i_{l1}, Y^r_{l2}, \ldots, Y^r_{ll}, -Y^i_{ll}$ on the Y^*_{lm} vector and $Y_{l0}, 2Y^r_{l1}, -2Y^i_{l1}, 2Y^r_{l2}, -2Y^i_{l2}, \ldots, 2Y^r_{ll}, -2Y^i_{ll}$ on the $Y_{l'm'}$ vector.

$$\begin{pmatrix} \tilde{a}_{00} \\ \tilde{a}_{10} \\ \tilde{a}^r_{11} \\ \tilde{a}^i_{11} \\ \tilde{a}_{20} \\ \tilde{a}^r_{21} \\ \tilde{a}^i_{21} \\ \tilde{a}^r_{22} \\ \tilde{a}^i_{22} \\ \tilde{a}_{30} \\ \tilde{a}^r_{31} \\ \tilde{a}^i_{31} \\ \tilde{a}^r_{32} \\ \tilde{a}^i_{32} \\ \tilde{a}^r_{33} \\ \tilde{a}^i_{33} \end{pmatrix} = \sum_k \Delta_{\rm pix} M_k R^k_{ll'mm'} \begin{pmatrix} a_{00} \\ a_{10} \\ a^r_{11} \\ a^i_{11} \\ a_{20} \\ a^r_{21} \\ a^i_{21} \\ a^r_{22} \\ a^i_{22} \\ a_{30} \\ a^r_{31} \\ a^i_{31} \\ a^r_{32} \\ a^i_{32} \\ a^r_{33} \\ a^i_{33} \end{pmatrix} \tag{4.13}$$

4.3 Difining a Direction for the Quadrupole and Octopole Components

Initially we will implement the definition of direction described in de Oliveira-Costa et al. (2004). This approximation to quadrupole and octopole direction was originally defined in order to investigate the apparent alignment between the quadrupole and octopole in the WMAP data (Bennett et al., 2011). The analysis was revisited in the 2013 Planck release (Ade et al., 2014f), where the significance of detection was found to be 99 % and the quadrupole and octopole misalignment was only 8° after correcting for the kinematic quadrupole (quadrupole contribution arising due to our motion relative to the CMB).

This method consists of finding the axis $\hat{n}$ around which the *angular dispersion* is maximized (de Oliveira-Costa et al., 2004). This is done by imagining the quadrupole and octopole components of a map as a wave function,

$$\frac{\delta T}{T}(\hat{n}) \equiv \Psi(\hat{n}) \tag{4.14}$$

which then has a maximized angular dispersion around some axis $\hat{n}$ given by

$$\langle \Psi | (\hat{n} \cdot \mathbf{L})^2 | \Psi \rangle = \sum_m m^2 |a_{lm}(\hat{n})|^2 \tag{4.15}$$

So, our estimate of a *planar* [1] quadrupole or octopole direction (or any multipole, for that matter) is simply given as the direction $\hat{n}$ which maximizes the sum above. For a completely planar component the vector direction $\hat{n}$ points perpendicular out of the the band around which the maxima and minima lays. This direction is found by rotating the spherical harmonic coefficients to every pixel in the $N_{\rm side} = 1$ and $N_{\rm side} = 2$ in our analysis and the pixel that maximizes

[1] See the last two images in figure C.4 for examples of more or less planar octopole components.

the above sum is saved as the planar direction of the octopolar or quadrupolar direction. The rotations are performed using the rotation matrices described in the appendix of de Oliveira-Costa et al. (2004), and includes among other things sorting the spherical harmonics into a vector with only real numbers by replacing the terms $e^{im\phi}$ in their definition with $\sqrt{2}\sin m\phi$, 1, $\sqrt{2}\cos m\phi$ for $m < 0$, $m = 0$ and $m > 0$. Effectively we are left with a vector of real, sorted spherical harmonic coefficients $\sqrt{2}\mathcal{I}\{a_{lm}\}$, a_{00}, $\sqrt{2}\mathcal{R}\{a_{lm}\}$. The rotational matrices are then applied in order to rotate the sorted spherical harmonics vector.

4.3.1 Map Correlation

As was emphasized above, the definition of direction for the quadrupole and octople assumes some planar property in the components. If we encounter octople maps of more complex shape, this definition will most likely not be able to pick up on any well defined direction, and the results of the comparison between maps could become less reliable. A different method could be implemented for a more reliable test of the similarities between the maps. We implement a correlation inspection of the maps with the Pearson correlation coefficient, also known as the Pearson's product moment correlation. The correlation coefficient between two maps X and Y with the same number of pixels is defined as in **?** and Lee Rodgers and Nicewander (1988),

$$r_{XY} = \frac{\sum_{i=0}^{N_{\text{pix}}}(X_i - \overline{X})(Y_i - \overline{Y})/}{\sqrt{\sum_{i=0}^{N_{\text{pix}}}(X_i - \overline{X})^2}\sqrt{\sum_{i=0}^{N_{\text{pix}}}(Y_i - \overline{Y})^2}}, \tag{4.16}$$

where X_i and Y_i gives the pixel values in the two maps at pixel i and $\overline{X}$ and $\overline{Y}$ are the mean of the maps. This coefficient is a measure between the similarity between two different discrete data sets. A correlation of 0 is completely uncorrelated, 1 is completely correlated and -1 is completely anti-correlated. In other words, $r = 1$ means that two variables increase in tandem, $r = 0$ means that a change in one variable does not affect the other variable, and $r = -1$ means that an increase in one variable leads to a decrease in the other. It is a direct measure of the linear dependence between two variables. An example of correlation coefficients between two data sets plotted as scatter plots is given in figure 4.2.

The idea is that an investigation of correlation between the maps might give an indication of the similarities between the data and simulations at each multipole, between two maps. In a way we are using correlation to find out how similar two images are, but our images just happen to be low resolution HEALPix maps. Of course, a problem in this case is that our images consist of 12 pixels and small differences in pixel values could have a large impact on the analysis, but in principle we should get a noticeably positive correlation between two similar maps, if not completely precise measurement. The goal is to find a more general way of describing the similarities between two maps instead of direction in the case where the direction is not a well defined property. We could then use a test statistics to find the significance of the similarities, given the null hypothesis that the maps are uncorrelated, or $r = 0$.

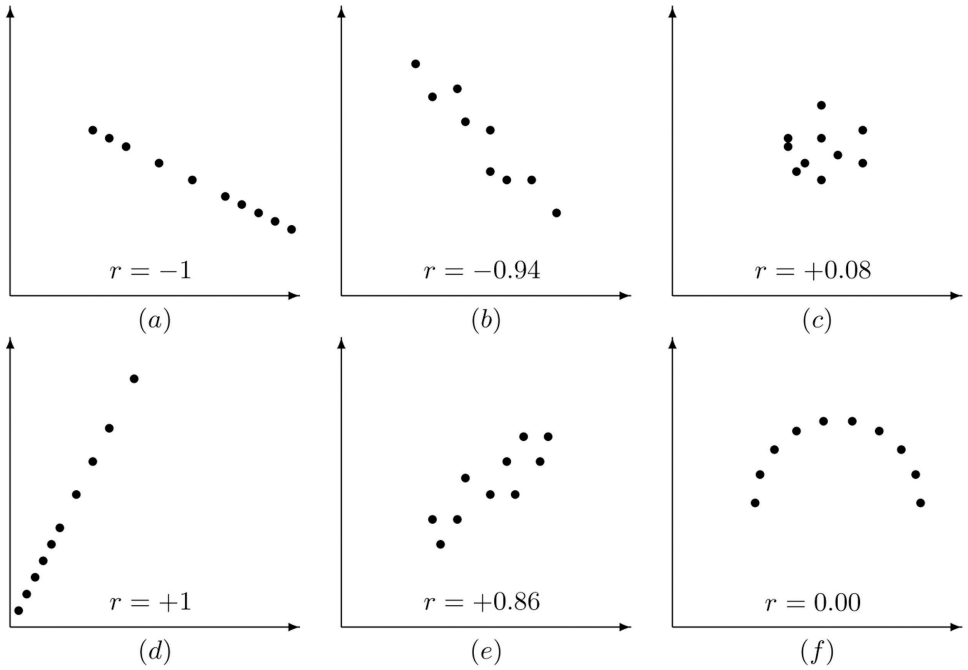

Figure 4.2: Illustration of correlation coefficients from $r = -1$ to $r = 1$. The image was retrieved from `https://stats.libretexts.org/Textbook_Maps/Map%3A_Introductory_Statistics_(Shafer_and_Zhang)/10%3A_Correlation_and_Regression/10.2%3A_The_Linear_Correlation_Coefficient` on 01.09.17

Chapter 5

Results & Cross Check of Performance

5.1 Cross-checking Method

Having generalized the algorithm used in the `remove_dipole` routine, we need to evaluate the performance of the method by comparing the dipole estimate produced using our matrix equations. This has been done in two ways, by first performing the analysis on a set of 5 maps in order to by eye assess the precision of maps produced by the estimate from our method compared to `remove_dipole` and the input parameters, and by generating 1001 maps in a similar way, and calculating the deviation from the directions given by the input parameters in section 5.1.1. In addition we have estimated the correlation between the original and reconstructed maps as a check to see if correlation can be a viable way to analyse the similarities.

The analysis of the first five maps are given with example maps in order to get a feel for the precision of our method. Coefficients are listed for each map as a_{10}, a_{11} for the input parameters, our estimate and `remove_dipole` estimate in table 5.1. The input parameters for the maps were created from the power spectrum given in the HEALPix package using the `create_alm` routine with 5 different RNG seeds, creating 5 random maps with the same statistical properties. The reconstructed maps are given in figure C.1 with input maps on the left and our estimate on the right, and C.2 with the same input on the left but with maps constructed from `remove_dipole` estimate on the right.

Even though our method is based on the same expression as the `remove_dipole` routine, we can see that the estimate in table 5.1 differ. The reason is not completely known, but it is most likely a consequence of the difference in expressions. Our matrix is a combination of more multiplications at each pixels compared to `remove_dipole` that only use the vectors estimated by `pix2vec` routine in HEALPix to transform the pixel number to coordinate. Each element is then a simple xx, xy, xz multiplications for each of the vector component. In our routine each of the matrix elements are the combination of two spherical harmonics, who's expression are combinations trigonometric functions. This makes the `remove_dipole` routine more computationally effective since it does not have to calculate the spherical harmonics at each data set and pixel. It may be that the magnitude of factors included in our calculation introduces different sources of errors than in the `remove_dipole` routine, giving rise to different errors, and subsequently different estimates. The reconstructed maps given in figure C.1 and C.2 show that even if this is the case our estimates do not appear to be worse than the `remove_dipole` routine. In fact, with these estimates, both seem to perform poorly, much worse than expeceted,

	Input coefficients	Matrix equation estimate	remove_dipole estimate
Map 1	(-2.88784, 0.00000) (-1.03352, 1.40258)	(-1.92228, 0.00000) (-5.22505, -4.16917)	(-1.04420, 0.00000) (-6.37590, -4.76308)
Map 2	(-2.46430, 0.00000) (1.52734, 3.28633)	(-4.93917, 0.00000) (7.16540, 6.41325)	(-5.93665, 0.00000) (1.26006, 1.50420)
Map 3	(-3.16522, 0.00000) (-6.78341, -0.85025)	(-5.53202, 0.00000) (4.74213, 8.38455)	(-11.28532, 0.00000) (7.16111, 9.46243)
Map 4	(1.50780, 0.00000) (1.91591, -0.62786)	(2.47397, 0.00000) (-0.55466, 12.55335)	(-9.03095, 0.00000) (6.31317, 22.30355)
Map 5	(0.39560, 0.00000) (-0.33523, 2.51781)	(2.08751, 0.00000) (-18.90763, -3.81189)	(-7.71231, 0.00000) (-11.83111, 18.71677)

Table 5.1: Comparison of performance between the method developed in this thesis and the `remove_dipole` routine provided in the HEALPix package. The maps used in the comparison were created from the input parameters given in the first column and up to $l_{\max} = 200$, and then masked with a downgraded U73 mask. The coefficients themselves were constructed from the power spectrum provided with the HEALPix package, using the `create_alm` routine. The middle columns gives the coefficients estimated from the masked maps by the method developed in this thesis, and the right column shows the `remove_dipole` estimate.

especially when compared to the estimated maps of the quadrupole and octopole.

The performance of the quadrupole and octopole estimation is slightly more difficult to pinpoint as the only comparison we can do is to the input parameters. A similar table as the ones above is given in table 5.2 for the quadrupole and table 5.3 for the octopole, and shows the estimated quadrupole and octopole components of the same five maps. The quadrupole components of the five $l = 200$ maps are shown together with maps reconstructed from the estimated quadrupole components of in figure C.3 and the same is done for the octopolein figure C.4.

When considering the directional estimates we will perform, the reconstructions seem to be good enough to get similar estimates. Looking at the first and third maps in figure C.4, both the input and the reconstructed ones, we can see signs of the potential problems discussed in section 4.3. Neither of these maps have a very clear planar component, and there might not be a very well defined direction in these two cases, potentially causing a large differences in the direction estimate from small differences between the maps. This further motivates the use of correlation in addition to angular clustering.

5.1.1 1001 Maps

We can see that although the estimates reconstructed in section C.1 are not perfect , much of the basic shape is the same between the original maps and their estimated versions. A calculation of directions on these should result in similar direction estimate for most maps, with a potential noticeable deviation in the dipole. We perform this same analysis on *many* more maps in order to see how the estimates perform on average. In this analysis we construct two different sets of maps, one with structures only up to $l_{\max} = 3$ (denoted low-l in the results) and one with structures up to $l_{\max} = 200$ as in the cross check above, and calculate the angular distance between the direction of the input maps to the reconstructed. We combine this investigation with a calculation of correlation. If our method had been able to estimate the coefficients perfectly we would expect correlation coefficients and angular distance $\cos(\Delta\theta)$ of around 1, but since the masking removes parts of the information available and create couplings between multipoles, this will not be possible. What we can expect if the routine performs as it should

	Input coefficients	Estimated Coefficients
Map 1	(3.43318, 0.00000)	(13.10768, 0.00000)
	(-43.21957, 7.14443)	(-46.59665, 8.64785)
	(-0.66746, -11.34556)	(0.92210, -5.69804)
Map 2	(50.74255, 0.00000)	(57.91564, 0.00000)
	(2.61325, -22.19211)	(3.73622, -25.15351)
	(-27.59577, -3.38846)	(-34.19785, -9.41293)
Map 3	(20.89543, 0.00000)	(25.49699, 0.00000)
	(52.89974, -43.53516)	(57.57484, -50.16285)
	(-2.09188, -38.70479)	(-8.14832, -41.89288)
Map 4	(50.35405, 0.00000)	(54.27940, 0.00000)
	(14.28472, -24.63454)	(13.95938, -29.53484)
	(-37.46594, 17.27344)	(-38.18893, 21.15806)
Map 5	(10.50937, 0.00000)	(22.72660, 0.00000)
	(12.12037, -13.62008)	(11.90875, -16.69035)
	(-53.19149, -32.71982)	(-57.28188, -37.30636)

Table 5.2: Comparison between the estimated quadrupole components of the five random constructed maps with structures up to $l_{max} = 200$. The first column shows the spherical harmonic input coefficients for $l = 2$, the second column shows the estimate. The coefficients and maps were constructed in the same way as the for the tables 5.1 and 5.3.

	Input coefficients	Estimated Coefficients
Map 1	(-10.32225, 0.00000)	(-12.07896, 0.00000)
	(-28.47761, -20.89857)	(-39.83422, -27.62542)
	(5.55362, -18.44429)	(5.21326, -19.77658)
	(-11.04653, 18.01716)	(-14.45080, 16.23913)
Map 2	(-8.23133, 0.00000)	(-10.67799, 0.00000)
	(10.05695, -4.28018)	(15.31860, -6.35704)
	(13.90018, 20.19460)	(13.72200, 24.93044)
	(-16.53871, 15.26785)	(-12.11573, 5.32980)
Map 3	(12.06784, 0.00000)	(16.92730, 0.00000)
	(25.35159, 20.56581)	(29.76267, 23.79450)
	(-23.08267, -10.24438)	(-25.97477, -14.15007)
	(-12.55704, -6.85660)	(-2.19967, -1.77304)
Map 4	(8.78322, 0.00000)	(10.59897, 0.00000)
	(-20.72684, 44.03496)	(-26.79880, 47.00748)
	(9.22581, 4.04625)	(12.87598, 3.37650)
	(-6.81874, -13.62201)	(-1.62585, -4.97066)
Map 5	(4.94916, 0.00000)	(8.34544, 0.00000)
	(-33.19677, -15.25938)	(-32.53121, -15.32951)
	(-16.84598, -2.39952)	(-16.59277, -4.90327)
	(16.25208, 23.59920)	(29.99926, 25.06727)

Table 5.3: Comparison between the estimated octopole components of the five random maps with structures up to $l_{max} = 200$. The first column shows the spherical harmonic input coefficients, the second column shows the estimate from a map $l = 200$. The coefficients and maps were constructed in the same way as the for the tables 5.1 and 5.2.

	$\cos(\Delta\theta)$, Low-l	$\cos(\Delta\theta)$, High-l	r_{corr}, Low-l	r_{corr}, High-l
remove_dipole	0.38395920	0.33487092	0.044190175	0.055283135
Dipole	0.38057311	0.33209062	0.34813541	0.31815221
Quadrupole	0.98396483	0.89747797	0.99898406	0.98046191
Octopole	1.0000000	0.85722130	1.0000000	0.97457989

Table 5.4: First two colums: Average angular distances between directions calculated from the input maps compared to the estimated maps from our method only in the quadrupole and octopole, and our method and remove_dipole in the dipole case. The low-l maps were constructed from the power spectrum provided in the HEALPix package with structures up to $l_{\text{max}} = 3$, the high-l map with structures up to $l_{\text{max}} = 200$. Last two colums: Average correlation coefficients between the maps from the same analysis.

are noticeably positive coefficients.

We create 1001 random generated maps from the base power spectrum available in the HEALPix package, in the same way as the five maps above were constructed. The resulting angular difference between the directions estimated from the dipole components of the input maps and the estimated maps are shown in figure 5.1, with our method in black and remove_dipole in red. The top figures show the difference in direction between the input map and estimated map when the input map only contains structures up to $l_{\text{max}} = 3$ to the left, and with structures up to $l_{\text{max}} = 200$ in the right, while the bottom figures show the corresponding correlation coefficients. Similar results are shown in 5.2 for the quadrupole and figure 5.3 for the octopole.

Again we see that the performance of our routine compared to remove_dipole is more or less equivalent in the sense that they are equally wildly varying. The angular distance $\cos(\Delta\theta)$ in the top figures for the two different sets of map have more or less identical results in remove_dipole and our method. It is hard to tell because the remove_dipole result lays more or less perfectly on top of our result. In the correlation analysis, on the other hand, thre seems to be a difference between our estimate and remove_dipole, with the oscillations seen in remove_dipole (green) being more centred around 0. The average angular distance and correlation coefficients are given in the top two lines in table 5.4. The difference between the methods are on average very small, both resulting in an average angular distance and correlation of ~ 0.3 to 0.4, except for the correlation between the input maps and the reconstructed remove_dipole. As we saw in figure 5.1, the remove_dipole correlation seem to be lower than the correlation found for our method, on average significantly lower.

This discrepency is very curious. Considering the fact that the remove_dipole routine is as well established as it is I am tempted to attribute this to an unknown bug. The implementation is very simple, and there is no sign there are any discrepencies between the implementation for the dipole component and the quadrupole and octopole components, but the inaccuracy of the estimates and reconstructed maps both shown in the plots here and in figure C.1 seem much larger than expected.

For the octopole and quadrupole we see that the precision of the estimates fall when increasing the details in the map from $l_{\text{max}} = 3$ to $l_{\text{max}} = 200$. This is an expected effect from the coupling between multipoles, both adjacent and nonadjacent. The couplings between low and high multipoles in the high-l maps is not captured when the estimate is only performed up to $l = 3$, since the first three multipoles also have couplings to much higher mulltipoles. The methods estimating the octopole from the low-l, shows a perfect direction estimate with the $\cos(\Delta\theta)$ equal to 1, while the quadrupole estimate is ~ 0.98. The low-l maps are designed with structures up to $l_{\text{max}} = 3$, so the masking causes noticeable couplings between $l = 2$ and $l = 3$.

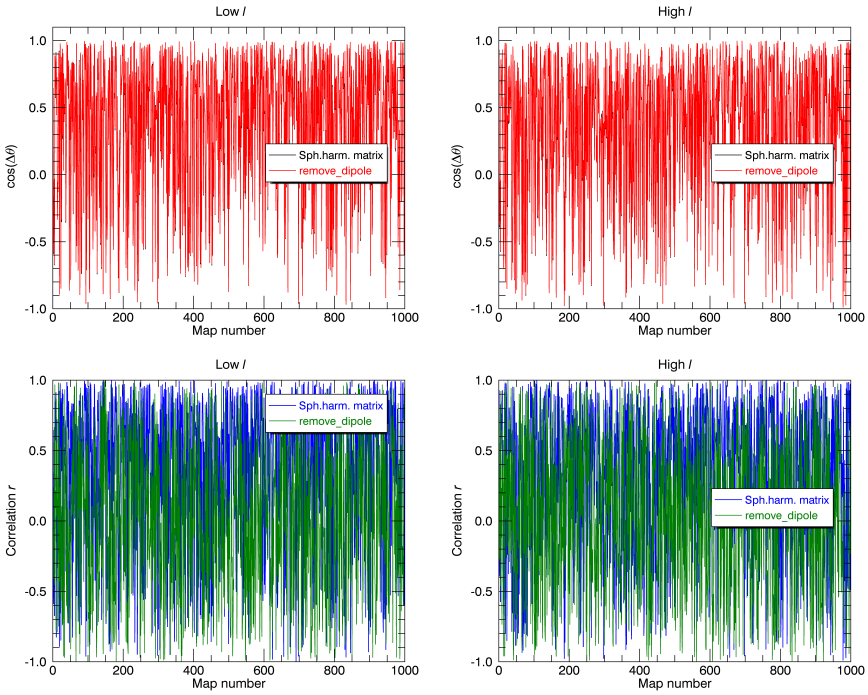

Figure 5.1: Top figures: Angular distance between the direction estimated for the dipole component of masked maps and an unmasked versions for 1001 maps constructed up to $l_{\max} = 3$ (left) and $l_{\max} = 200$ (right) The black line shows the estimate from our method (well hidden behind the red), the red line shows the estimate from `remove_dipole`. Bottom figures: Correlation coefficients calculated between the same maps as the ones used to produce the difference in direction in the top images for a map constructed up to $l_{\max} = 3$ (left) and $l_{\max} = 200$ (right), The blue line shows the correlation between the unmasked input maps and our estimate and the green line shows the correlation between the input and `remove_dipole`.

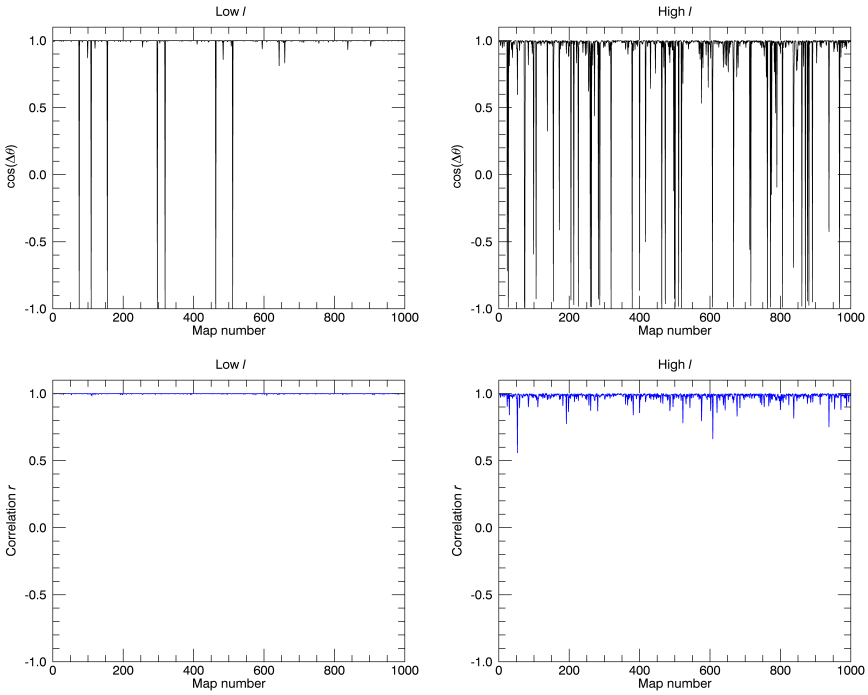

Figure 5.2: Top figures: Angular distance between the direction estimated for the quadrupole component of masked maps and an unmasked versions for 1001 maps constructed up to $l_{\max} = 3$ (left) and $l_{\max} = 200$ (right). Bottom figures: Correlation coefficients calculated between the same maps as the ones used to produce the difference in direction in the top images for a map constructed up to $l_{\max} = 3$ (left) and $l_{\max} = 200$ (right).

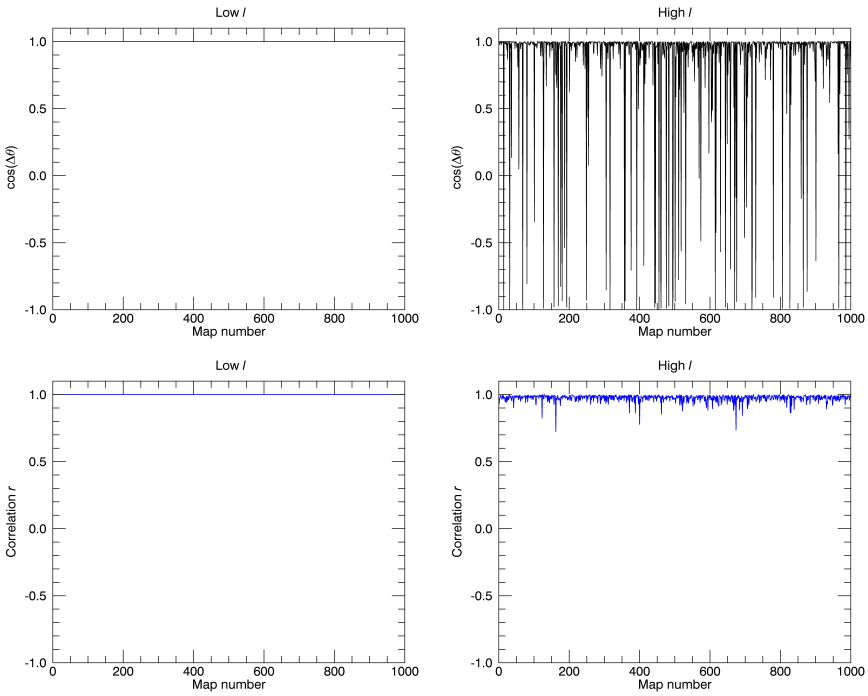

Figure 5.3: Top figures: Angular distance between the direction estimated for the octopole component of masked maps and an unmasked versions for 1001 maps constructed up to $l_{\max} = 3$ (left) and $l_{\max} = 200$ (right). Bottom figures: Correlation coefficients calculated between the same maps as the ones used to produce the difference in direction in the top images for a map constructed up to $l_{\max} = 3$ (left) and $l_{\max} = 200$ (right).

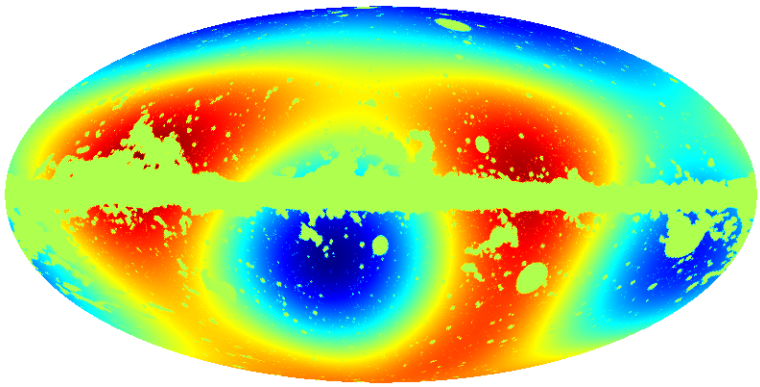

Figure 5.4: Example of a large structure map masked by the U73 mask. The map has been created by one of the 1001 random generated maps used to generate the correlation coefficients and angular distances plotted in figure 5.1 - 5.3 using a resolution of $N_{\text{side}} = 128$. The U73 mask has been down graded to the same resolution.

Ths coupling between $l = 2$ and $l = 3$ is not included in the estimate when it is only performed for the quadrupole causing the slightly worse precision in the quadrupole estimate. Had the maps used in the quadrupole estimate only contained structures up to $l = 2$ the result would have been as precise as the octopole estimate.

This coupling effect is best illustrated by showing a masked map of large structures. An example is shown in figure 5.4. The masking breaks up the structures, effectively creating several smaller structures accross the map. The more ”complicated” the mask (more disconnected blobs spread accross the map, no clean band), the more structures are created. This together with the loss of information in the masked areas give rise to the loss of precision in maps with smaller structures/greater details.

What we can also see is that the correlation coefficients between the maps are noticeably positive, motivating the use of correlation coefficients together with the direction estimate when assessing the presence of the angular clustering. The angular distance estimates frequently dip down to $\cos(\Delta\theta) = -1$ in the high-l maps, even when all vectors with $\theta > 90°$ are flipped in the opposite direction, demonstrating the potential problems occurring from not having a well defined direction. The estimates of correlation coefficients appear on average more accurate than the direction estimate, and can help us see if the direction estimate catch enough of the directions to give a reliable result, or if the orientations of the positive and negative spots on the maps are too complex for the routine to find a well defined planar direction. The significance result in the following sections are therefore accompanied by a correlation plot.

5.2 Reproducing Planck Results

Having armed ourself with a method which has adequately reproduced the underlying coefficients of masked maps with different levels of detail, we need to know if it is capable of reproducing the results published in the 2015 Planck isotropy article (Ade et al., 2016c).

The angular clustering of dipole direction accross multipoles is calculated as described in section 3. A map is partitioned in $N_{\text{side}} = 1$ patches accross the sky and a power spectrum is estimated in each patch. For each data set (simulation or observational data) and multipole l we then have an $N_{\text{side}} = 1$ map giving the value of the power spectrum C_l calculated in each patch. These indicate the strength of the fluctuations on all scales from $l = 2$ to 1500 in each patch. The dipole components of each such map is then calculated resulting in a dipole direction, and the angular distance between these at each multipole is calculated using the expression for the cosine of the angular distance between two points on a sphere, $\cos(\Delta\theta)$, in equation **??**. The portion of simulation that has a clustering as strong as the observed data is then found using Rayleigh statistic given in equation 3.5. Example maps of the "power spectrum maps" are given in figure 3.3.

Figure 5.5 shows the result of the angular clustering significance implemented by us in the top figure, and the Planck results produced using estimates from the four different foreground cleaning methods are shown in the bottom figure. The significance of the clustering found using our estimates of the dipole components are very similar to the result published in Planck (SMICA result from 500 simulated maps are shown in light blue in the top figure), confirming that the implementation of the method works as intended. The significance found using `remove_dipole` estimate is shown in red in the top figure, overplotted together with the significance found using ours. For most multipoles it would seem that the significance achieved with our method is slightly higher thant the `remove_dipole` estimate, but the difference is negligible. We can see this if we look closer at the Planck results in the bottom part of the figure.This difference in significance is well whithin what we see between the four different foreground cleaning methods, and is most likely a result from the difference in estimated directions between the two.

Figure 5.6 shows the same analysis performed on $N_{\text{side}} = 2$ maps instead of the $N_{\text{side}} = 1$ used in Planck. The estimate is found using two different $N_{\text{side}} = 2$ maps; one where the pixels along the eqator is masked (black line), and one where they are not (green). We have included an example of $N_{\text{side}} = 1$ and $N_{\text{side}} = 2$ maps in figure 5.7 in order to show that the power spectrum estimated from the pixels around the equator contain nearly no information compared to the equator pixels in the $N_{\text{side}} = 1$ map. This lack of information leads to strong oscillations in the power spectrum at the equator pixels, and even if the power spectrum maps are already weighted by standard deviations calculated from the simulations, the lack of information in these pixels leads us to believe that the value of the C_ls calculated there are not reliable.

Figure C.5 and figure C.6 in section C.2 show a set of continuous power spectrum (constructed from the binned spectrum as described in section 2.3) picked out for a set of pixels in one of the $N_{\text{side}} = 1$ maps (figure C.6) and $N_{\text{side}} = 2$ maps (figure C.5). The pixels from 22 and up in figure C.5 are picked out from the heavily masked equator of the $N_{\text{side}} = 2$ map, and we can see that compared to the power spectrum from the second pixel shown in the top left plot in the same figure, and the plots in figure C.6, these contain strong oscillations and in some cases it is difficult to make out the basic shape of the power spectrum. The power spectrum of pixel number 33 (the one crossing from the far left to the far right on the pixel line below the

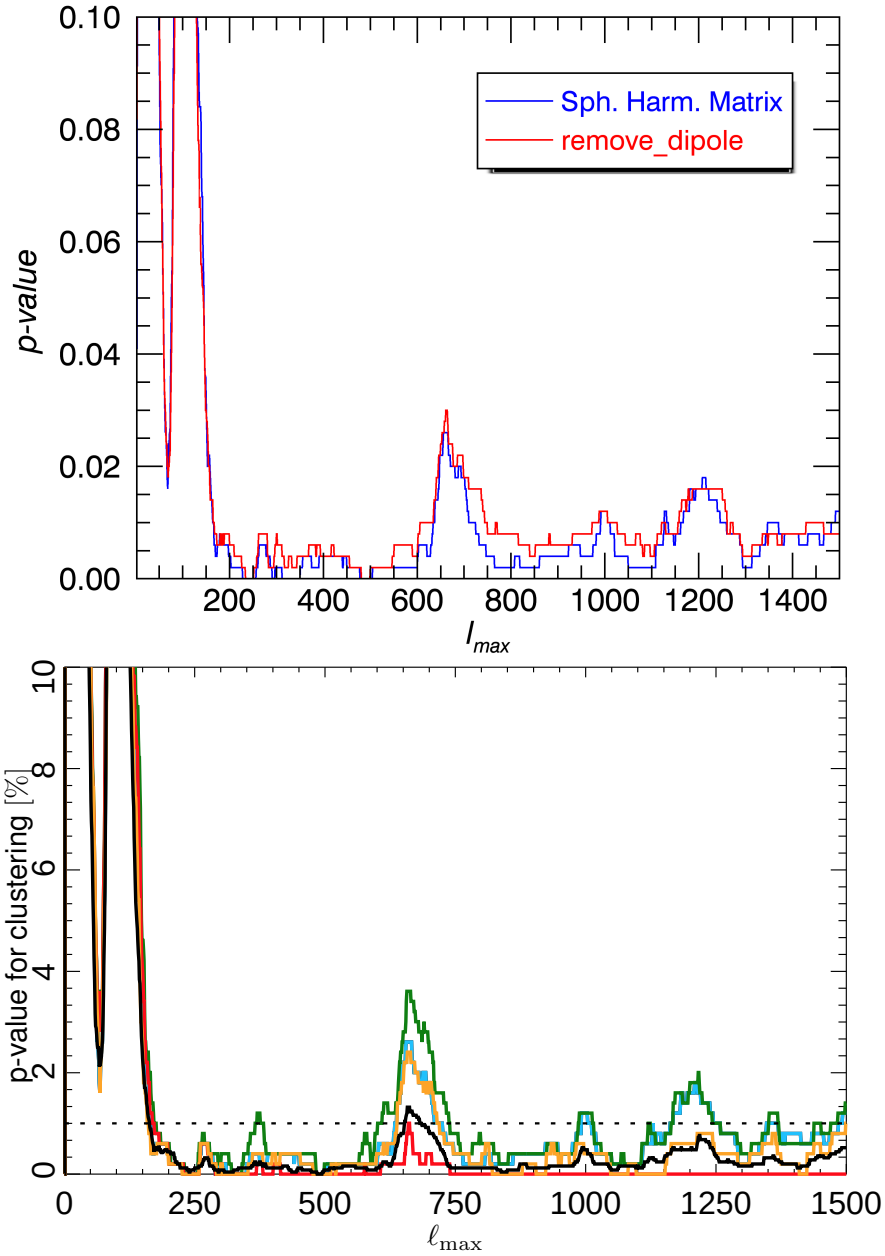

Figure 5.5: Significance of dipole angular clustering produced using our method and `remove_dipole` in the top figure, based on 500 simulations. The equivalent result published in the Planck 2015 isotropy article is shown in the bottom figure, determined for the four different foreground cleaned maps, Commander (red), NILC (orange), SEVEM (green), and SMICA (blue). For the SMICA maps, the p-values based on 2500 simulations are also shown (black). The p-values are based on the fraction of simulations Rayleigh statistic (see equation 3.5), determined for each multipole l, compared to the data. The results shown here have been marginalized over bin sizes in the range $\Delta l = 8$ to $\Delta l = 32$.

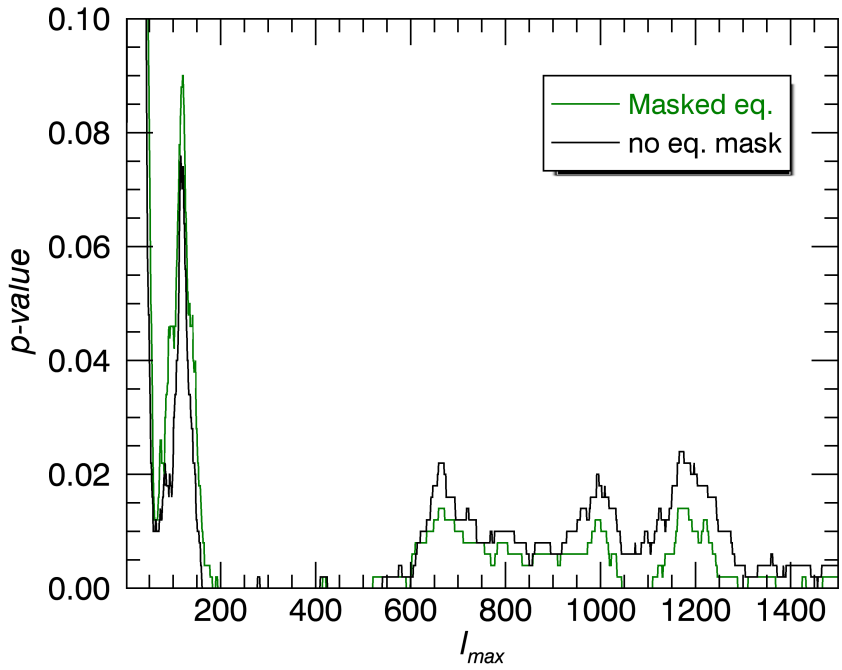

Figure 5.6: Significance of dipole angular clustering produced using our method and `remove_dipole` using the HEALPix $N_{\text{side}} = 2$ maps as opposed to the $N_{\text{side}} = 1$ maps used for figure 5.5. The black line shows the result when no pixels in the $N_{\text{side}} = 2$ maps are maskde, while the green line shows the estimate achieved when removing the equator pixels that are heavily influenced by the U73 mask in the power spectrum calculations.

equator) is also included, because it appears to also be heavily masked by the U73 mask.

These example power spectrum are picked out from the data, but we could quantify this information loss across data and simultions. The increase in oscillations is basically an increase in standard deviation for pixels around the equator, and we can compare this to the standard deviation in the rest of the map.

The standard deviation of a set of discrete data x of n samples is defined as in equation 5.1, where $\overline{x}$ is the mean of the data set. What we want to investigate is the standard deviation accross the power spectrum, in each pixel of the map. The number of samples equauls the number of multipoles in the spectrum and the mean is the mean accross it. The resulting standard deviation is plotted as a function of data set (simulation or observational data) in figure 5.8 for pixel 3 and pixel 24. The index containing the observational data is marked with a green line. Both standard deviations have been normalized by the maximum value in pixel 24 for illustration purposes, the actual values are in the range 10^{-9}.

$$\sigma = \sqrt{\frac{1}{n-1}\sum_{i=1}^{n}(x_i - \overline{x})^2} \tag{5.1}$$

It is clear that the pixels in the equator area exhibit a significantly larger standard deviation than the ones outside it, across all simulations. Even if we here do not show the standard deviation for all pixels, this plot together with the power spectrum shown in figures C.5 and C.6 motivates the removal of this area in the angular clustering analysis. We have included a

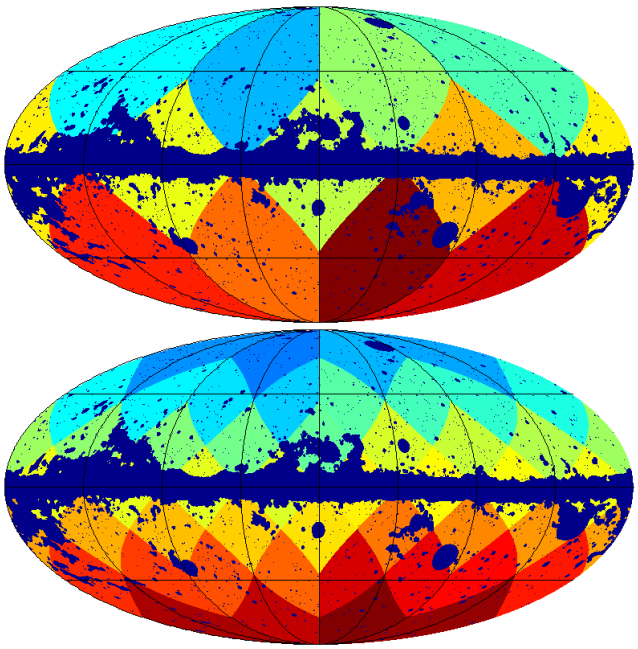

Figure 5.7: Example map showing the pixel size of an $N_{\text{side}} = 1$ (top figure) and $N_{\text{side}} = 2$ (bottom figure) maps with the U73 mask on top.

magnified plot of the simulations numbered 0 to 50 to demonstrate that it is not the data that exhibits a strikingly large standard deviations compared to the rest of the data sets, but one of the generated simultions. All results from $N_{\text{side}} = 2$ are shown with analysis done on maps with a masked equator as well as for maps with no equator mask.

Looking at figure 5.6, containing the angular clustering significance of dipole components calculated on $N_{\text{side}} = 2$ maps, it appears that the estimates from a masked equator has a slightly higher significance than the map that is not masked. In general, both masked and unmasked map show a higher significance in the range $l = 200$ to $l = 500$, and a slight decrease in the range $l = 600$ to $l = 1000$ than the $N_{\text{side}} = 1$ calculations. We can clearly see the top of the peak around $l \sim 150$ which was hidden well above $p = 0.1$ in the $N_{\text{side}} = 1$ maps, and the significance between $l = 200$ and $l = 500$ is whitin three decimals equal to 0. Otherwise the general shape of the significance stays the same, with the same peaks around $l = 700$ and $l = 1200$.

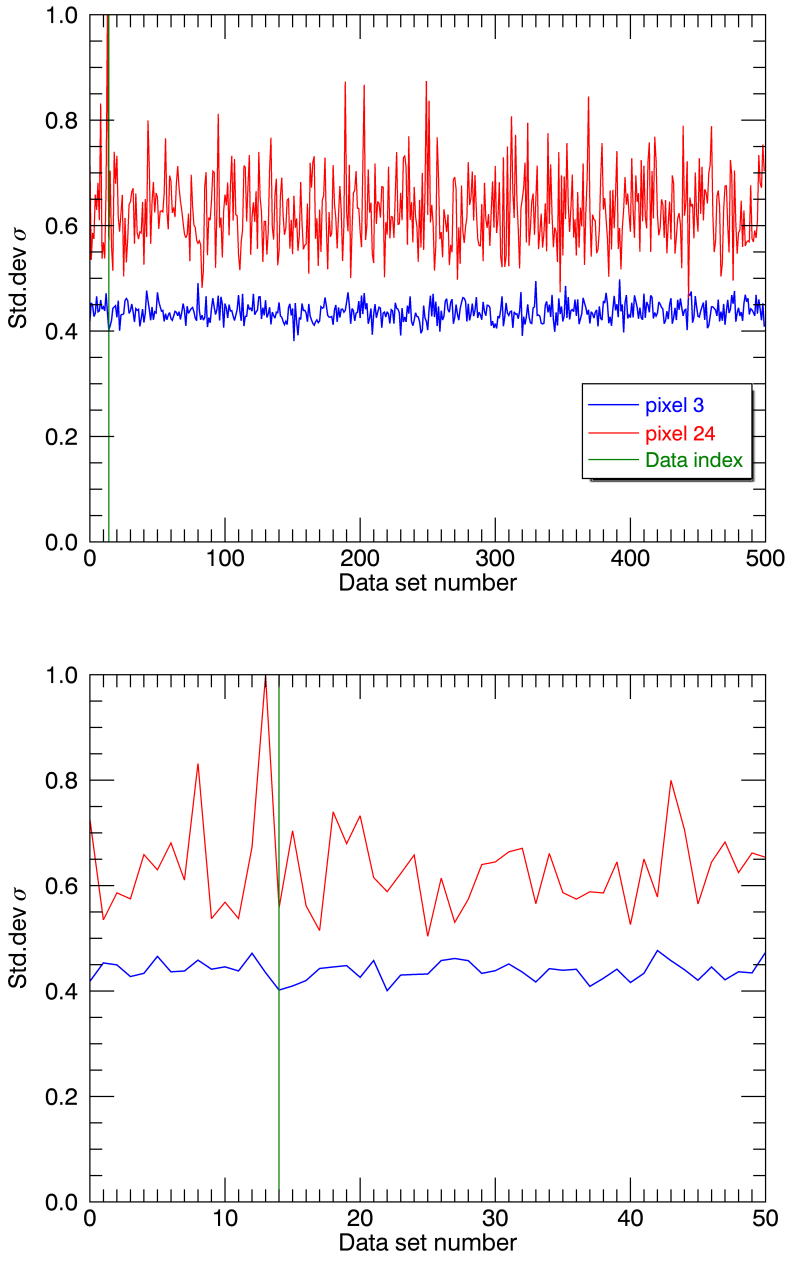

Figure 5.8: Standard deviation of pixel 3 and 24 in the $N_{\text{side}} = 2$ for all 500 simulations + data in the top figure and for the first 50 in the bottom. Since we are interested in the standard deviation in the heavily masked pixels compared to other, less affected pixels, we have normalized the data by the maximum value in pixel 24 in order to better illustrate the result. The range of the values are in reality around 10^{-9}. The number containing the observational data in the list of data sets is indicated by the green line in the plot. It would appear that the biggest standard deviation occurs in the data, but the bottom figure shows that it is actually a simulation and that the observational data does not exhibit any different standard deviation than the the rest of the simulation.

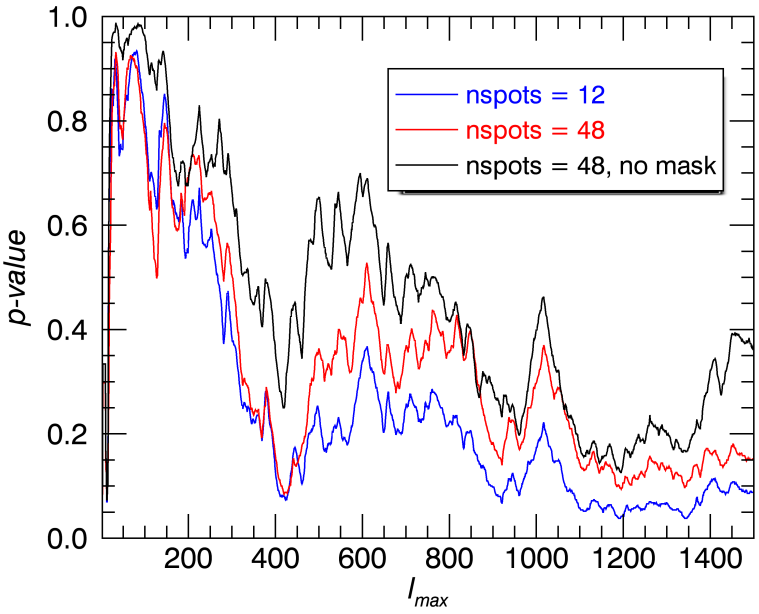

Figure 5.9: Angular quadrupole clustering calculated using the pseudo-Rayleig statistic given in equation 3.5. The angular difference is found from the ddefinition of direction of quadrupole and octopole components given in section 4.3.

5.3 Clustering of the Quadrupole and Octopole Directions

Performing the same angular clustering analysis on the quadrupole and octopole results in figures 5.9 and 5.10. The quadrupole and octopole components are calculated from the $N_{\text{side}} = 1$ (only the quadrupole) and $N_{\text{side}} = 2$ maps (octopole and quarupole), constructed as described in section 2.3. The spherical harmonic coefficients up to a given l (no higher than 3) is calculated using the code developed in this thesis, and the direction is estimated as described in section 4.3, based on de Oliveira-Costa et al. (2004).

Since this method investigates the driection of planar like quadrupoles and octopoles, the direction given is not completely defined. It can be given as either "upwards" or "downwards", a difference of 180°, with both results being perpendicular to the plane, and therefore equally correct. Not correcting for this will affect our estimated clustering since a difference of 180° results in a large angular distance between direction, which is not picked up as a detection by the pseudo Rayleigh statistics. Because there is no obvious criteria or consistency in the definition of direction to indicate whether the "upwards" or "downwards" direction are found, we flip all vector directions that have a θ coordinate greater than 90° (i.e. all the vectors pointing below the equator) by 180°, setting them equal to the negative of the first estimated vector direction. This ensures that all estimated directions are at least pointing towards the same hemisphere.

In the quadrupole case, the $N_{\text{side}} = 1$ map gives the highest significance (lowest p-values), followed by the $N_{\text{side}} = 2$ map with equator masking and then the unmasked equator. We argued in section 3.1 that the $N_{\text{side}} = 1$ maps contain enough information to calculate the quadrupole components of a map, but considering that the the significance falls off as we increase the resolution, this might indicate that an analysis like this requires a resolution higher than the $l_{\text{max}} \approx 2N_{\text{side}}$ rule of thumb. Something similar can be seen by the increase in significance in

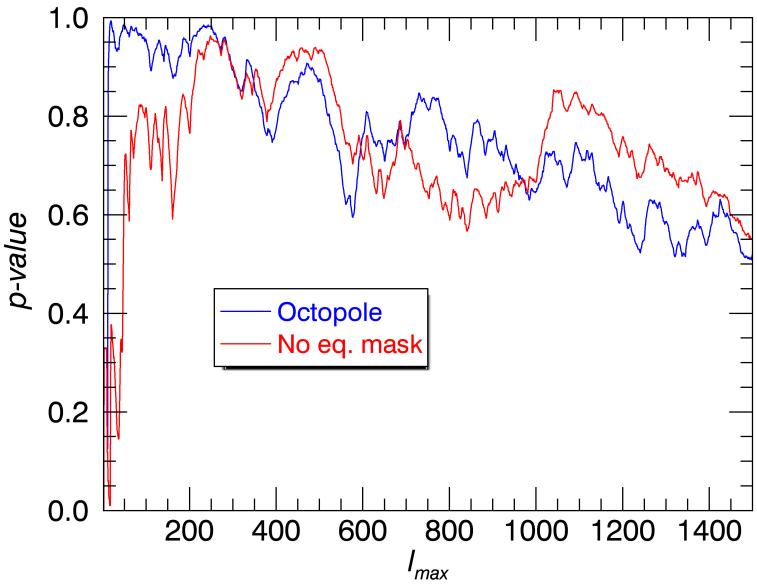

Figure 5.10: Angular octopole clustering calculated using the pseudo-Rayleig statistic given in equation 3.5. The angular difference is found from the ddefinition of direction of quadrupole and octopole components given in section 4.3.

the dipole significance when moving from $N_{\text{side}} = 1$ to $N_{\text{side}} = 2$. In that case, the increase in resolution strengthens the detection seen in the $N_{\text{side}} = 1$ map in parts of the multipoles, even if we do not mask the heavily masked equator pixels. The fact that the quadrupole significance decreases with increased resolution might therefor indicate that having a higher resolution gives a more reliable result. Even so, no multipole range in the plot shows any sort of significant detection of quadrupole angular clustering in any multipole range, whether they are masked or not.

In the octopole case shown in figure 5.10 the significance is much lower than for the quadrupole, remarkably so in the lower multipoles. Since the directions should be random distributed in an isotropic universe, we would expect some clustering accross the multipoles. An absence of clustering is also curious, and p-value of 1 is just as remarkable as a p-value of 0. In the clustering calculated with the $N_{\text{side}} = 2$ maps that have not been masked across the equator we can see p-values very close to 1 in the low multipole range. Masking the pixels with the highest standard deviation removes some of this, but we can still see remarkably high p-values around $l = 300$. Since this occurs in both the masked and unmasked $N_{\text{side}} = 2$ it is most likely not an artefact introduced from the masking. The octople is still well whithin the rule of thumb limit $l_{\text{max}} \approx 2N_{\text{side}}$, so increasing the the resolution of the maps used when finding the octopole clustering would most likely not change this estimate significantly. This indicates that it is present in the estimation of octopole directions, and tells us that compared to the observed data, the octopole in the simulation has nearly no clustering accross some of the lower multipoles.

Picking out a simulation and running it through the same framework as the data can give us a better indication of how the behaviour of the p-values will be in a data set that is based on the assumption of isotropy. Figure 5.11 shows such a comparison, with the dipole, quadrupole and octopole angular clustering significance in the same figure. We see that the same high

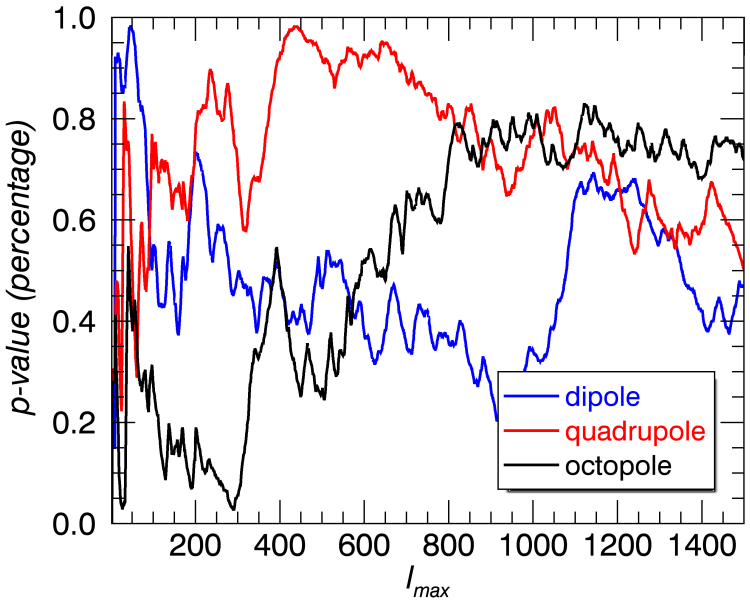

Figure 5.11: Significance of the dipolar, quadrupolar and octopolar angular clustering significance for a randomly chosen $N_{side} = 2$ simulation set. The simulation was put in place of the data and run through the same framework as the data that produced the p-values in figure 5.5, 5.9 and 5.10.

p-value occurs for some multipole ranges in the simulations as well. The occurance in the octopole is most likely a combination of the random nature of the simulations and the fact that the defintition of direction is not perfect for the octopole and quadrupole.

5.4 Correlation Analysis

The correlation coefficient between two maps is given in equation 4.16. By reconstructing a cleaned map from the estimated spherical harmonic coefficients used when calculating the direction of the quadrupole and octopole in the previous section, we can find the correlation coefficient between maps for every multipole. The angular clustering gives us the similarities between the directions of the multipole maps in the data. This essentially means that the maps are very similar accross multipoles, not including amplitude. An equivalent investigation of this using map correlation would then involve correlating the data sets at each multipole to all other multipoles. This will give us a set of $l_{\max} = 1500$ correlation coefficients at each multipole for the component of interest. The correlation analysis done for the dipole, quadrupole and octopole components were performed from maps constructed from only the dipole, quadrupole *or* octopole components, setting the spherical harmonics coefficients of the other multipoles l to 0. The correlation between the dipole maps for example, sets the monopole to 0 before performing the analysis. Since we are primarily interested in the level of correlation between direction, we also normalize the maps by their max-value before the analysis is performed, so that only the similarities in the shapes of the structures are taken into account.

If it is only the alignment of the quadrupole and octopole we are interested in, then an anti-

correled result is equivalent to a correlated result. The alignment of a map is defined by how the patches are oriented, and not where the specific positive and negative patches are placed. An anti-correlated result means that a map is the negative of the map it is correlated to. The patches of positve and negative values are still in the same positions, just with positive patches in place of the negative ones, so the direction the way we have to defined is still the same. We can therefore conclude that the alighnment between the maps is still present in both the anti-correlated and correlated case, and that maps with a large negative correlation are still strongly aligned. This is only valid for our definitions of quadrupole and octopole alignment. Since the dipole has a very well defined direction, an anti-correlation would mean that the directions differ by 180°, and the angular directions are not clustered.

Figure 5.12 shows the average correlation coefficient at each multipole. Considering that the dipole has a well defined direction it is odd that the average correlation between maps at each multipole is as low as it is in the dipole, but the average value is not a good way to judge the significance of the result. In addition, there seem to be a clear difference between the correlation estimated using the $N_{\text{side}} = 1$ and $N_{\text{side}} = 2$ maps. The oscillations in the green line shows the $N_{\text{side}} = 1$ average correlation, and seem to be much smaller than the red and blue lines that show the $N_{\text{side}} = 2$ maps with a masked or unmasked equator. The quadrupole has by far the lowest average, while the octopole average oscillate around as much as the dipole, but tend to be slightly larger than 0, while the dipole oscillate equally far both to the negative and positive side.

In the case of the quadrupole and octopole components of the maps, it might also be interesting to see how the average would change by using the absolute value of the correlation coefficients, since anticorrelated maps are still aligned. For the absolute value, a result of around 0.5 would mean that the values have a spread between 0 and 1, and that the values before taking the absolute value are spread evenly between -1 and 1. These absolute value plots for the quadrupole and octopole are shown in figure 5.13. The average value of the quadrupole is now higher than the octopole, but the difference is not striking. The fact that the values did not automatically jump to around 0.5 tells us that the correlation is not wildly varying between 1 and -1 in, and that there might be some alignment between the maps at each multipole, resulting in an average correlation coefficient of aroun ±0.4. This is expected to some extent, considering that this is a random process, and in the same way that we would expect clustering to some degree (mentioned in the discussion on angular clustering in the octopole in section 5.1), we also expect so see some alignment in the correlation. The fact that the data has an average correlation coefficient at each multipole of ±0.4 does not necessarily tell us that there is a signifcant correlation

In figure 5.14 we have plotted the same averages, but this time calculated for two simulation together with the $N_{\text{side}} = 2$ data chosen from the first set of 25. As expected we see that the averages are more or less identical in the data and the simulations. With 500 simulations there is a chance that we would pick a random simulation that coincidentally have multipole maps very similar to those in the data, but given the significance calculated for the dipole in the previous section, this is highly unlikely to be the case in the top left part of figure 5.14. We need a test statistic that can better tell us the probability that the simulation maps are as aligned as the data across multipoles.

Without knowing whether or not the power spectrum maps are normally distributed, and assuming that they are most likely not considering that all maps are based on the underlying CMB power spectrum, finding a suitable test statistic is not trivial. There are alternatives that

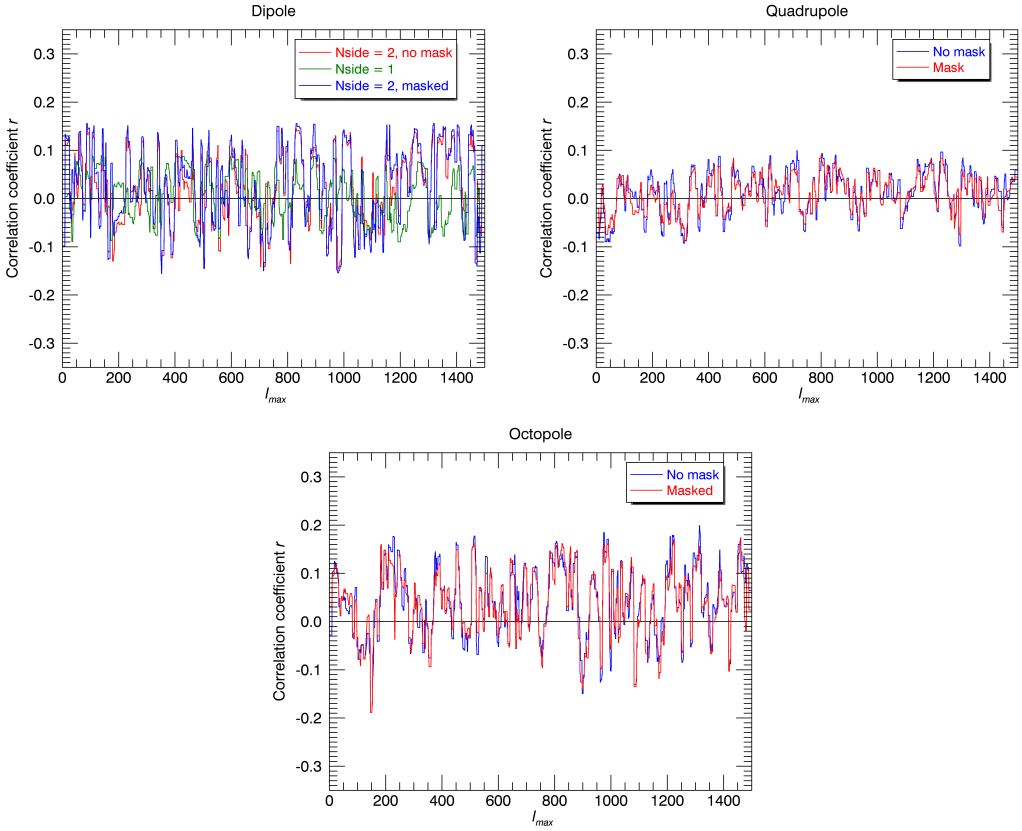

Figure 5.12: Correlation coefficeint averaged at each multipole. Top left is the dipole correlation, top right the qudrupole and the bottom image is the octopole. The plots show $N_{\text{side}} = 2$ with an unmasked and masked equator, with $N_{\text{side}} = 1$ is also included for the dipole correlation.

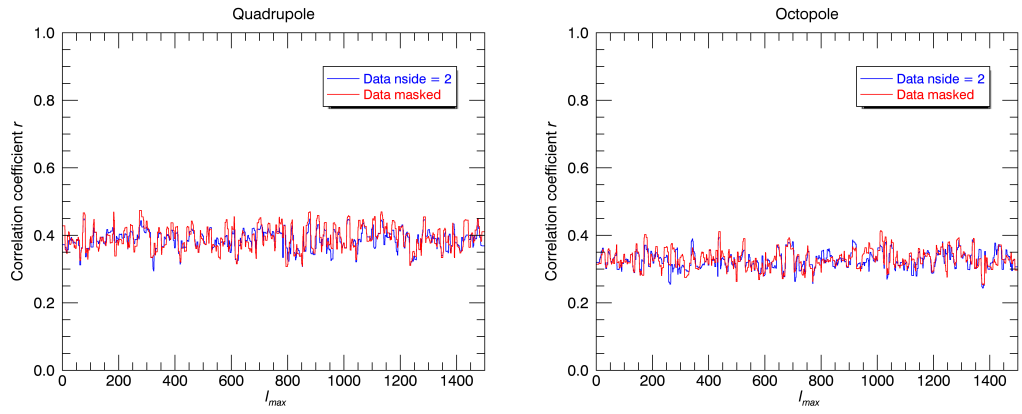

Figure 5.13: Absolute value of correlation coefficeint averaged at each multipole for the quadrupole (left) and the (octopole). The plots show $N_{\text{side}} = 2$ with an unmasked and masked equator.

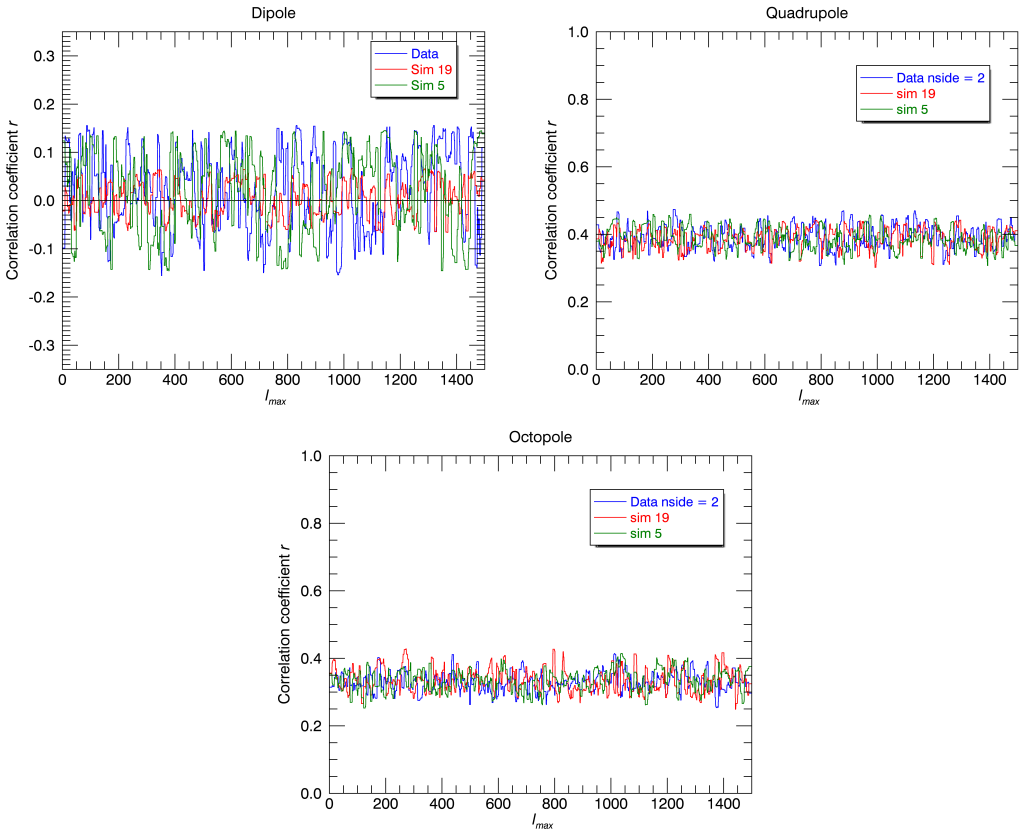

Figure 5.14: Correlation coefficeint averaged at each multipole for the masked $N_{\text{side}} = 2$ map of the data and 2 simulation, simulation maps 5 and 19. Top left is the averaged dipole correlation, top right the averaged absolute value of the qudrupole correlation and the bottom image is the averaged absolute values of the octopole correlation.

are based on ranked data (Vittinghoff et al., 2011), but this can quickly become complicated and due to the limited amount of time until the deadline of this thesis, we will instead implement the same pseudo-Rayleigh statistics as the ones used on the angular clustering. This statistic only measures the cumulative clustering up to a certain multipole l_{lim}, and finds the fraction of simulations that have a higher cumulative clustering. Neither the angular directions of the dipole or the correlation coefficients can with any cerainty be said to be normally distributed, which is not needed for this statistic. It does not fit any values to a standard table or distribution, but simply calculates a fraction which we interpret as a significance.

$$RS_{\text{corr}} = \sum_{l=2}^{l_{\text{lim}}} \frac{r_l^{XY}}{l_{\text{lim}} - 1} \tag{5.2}$$

The resulting significance for dipole, quadrupole and octopole is shown in figure 5.15. The only difference between the calculations of these p-values compared to the ones in the previous section, is that the sum runs over correlation coefficients instead of angular distance between directions of each power spectrum map. The pseudo-Rayleigh statistic is redefined as in equation 5.2, where r_l^{XY} denotes the correlation coefficient between two power spectrum maps X and Y at multipole l.

Initially, we do not use the absolute value for the quadrupole and octopole correlations discussed above in order to see if there is a significant correlation when we do not include the effect of anti-correlated maps. In this case the anti-correlated maps in the data will lower the significance since it is a negative contribution to the test statistic. If the results are still more correlated in the data than the simulations, then the postioning of the positive and negative patches in the sky is also more aligned across multipoles in the data, and not just the directional alignment like we defined it in section 4.3.

Oddly enough, in this correlation analysis there is no strong significance in the dipole. It seems that the $N_{\text{side}} = 1$ maps gives the largest significance in the range $l = 600$ to $l = 1000$, but in the higher multipoles the significance more or less disappear. The correlation done on maps with $N_{\text{side}} = 2$ is insignificant on all multipoles. We would expect to a strong significance in the correlation analysis considering the angular clustering detected in section 5.2, since a clustering of the directions indicate that the maximum values in the maps lay around the same place. If these structures are in the same place, we would expect to a strong correlation, and a strong significance.

The quadrupole does not show any signs of a significant correlation in the data compared to the simulations, but the octopole has a significance in the very limit in the higher octopole. The significance grows steadily until $l \sim 800$ where it seems to flattens out and stay steady at around $p = 0.005$ until $l_{\text{lim}} \approx 1400$. This is just in the limit of what we have considered as significant, but the result is interesting. Only around 0.5% of simulations are as correlated between multiopoles from $l = 1000$ and up.

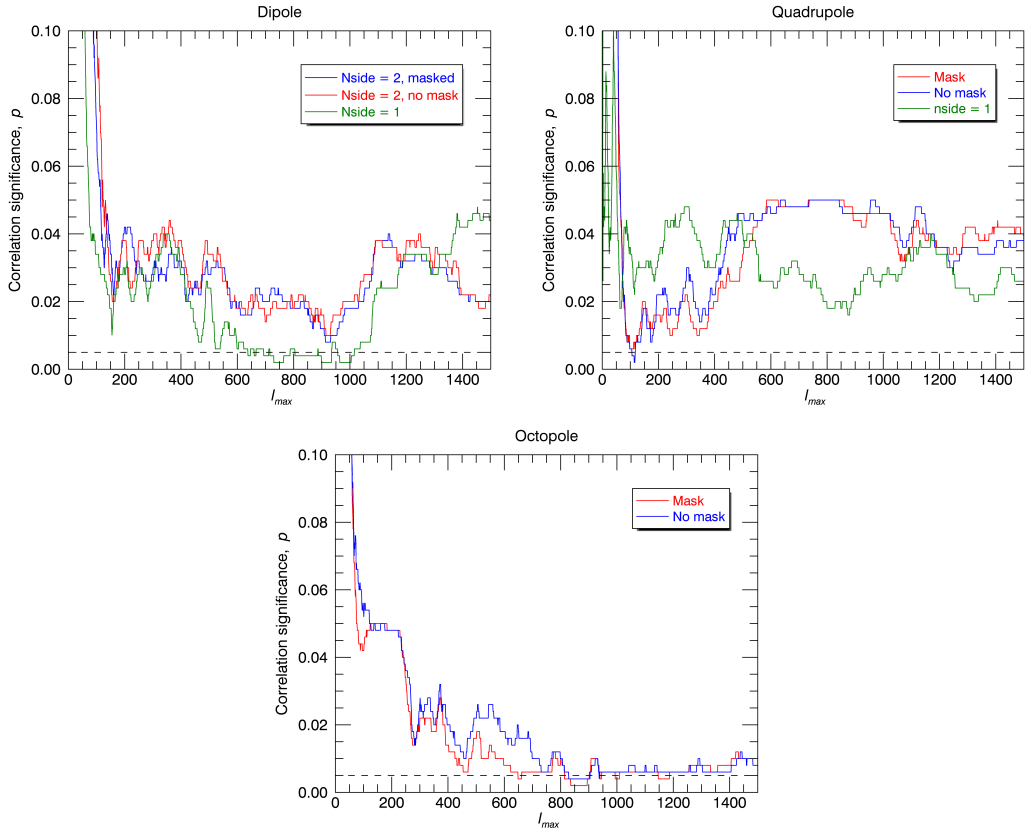

Figure 5.15: Significance of the correlation between power spectrum maps from the observed data compared to simulations. The correlation of the dipole components are shown in the top left, quadrupole in top right and octopole at the bottom. The statistics were calculated using the same pseudo-Rayleig statistic as the angular clustering significance shown in figures 5.5, 5.6, 5.9 and 5.10, but this time using the form given in equation 5.2 instead of equation 3.5.

Figure 5.16 shows the same type of significance plots, but this time for three randomly chosen simulations instead of the data. Note that the y-axis in these covers the range 0 to 1 and not 0 to 0.1 as the plots in figure 5.15. Most of these are far from significant, except for simulation 43, which has very low p-values in both the dipole, quadrupole and octopole. In the dipole and the range $l = 100$ to $l = 400$ in the quadrupole, the significance of simulation 43 seems to be slightly below significant (shown as a dashed line at the very bottom), but again, this might be the case when we pick out a random simulation from a set of 500. What is curious is that this simulation has low p-values accross both the dipole, quadrupole *and* octopole. There seems to be some dependence between the components. The maps used in this correlation analysis are reconstructed from only the components for the given $l = 1$, $l = 2$ or $l = 3$, with all others set to 0. If this was not the case, a correlated result in the dipole would affect the quadrupole and octopole as well if the dipole components were strong enough, and we would expect the correlation significances to be very similar. With all other multipoles set to 0, this is not the case and it would be unlikely to see similar correlation significance accross the three plots. Again, this is random data, but the fact that we manage to pick just the right one that happened to display this is curious.

Finally, we perform the same significance test for the absoute value of the correlation coefficients. The resulting significance is shown in figure 5.17, and it appears that the significance

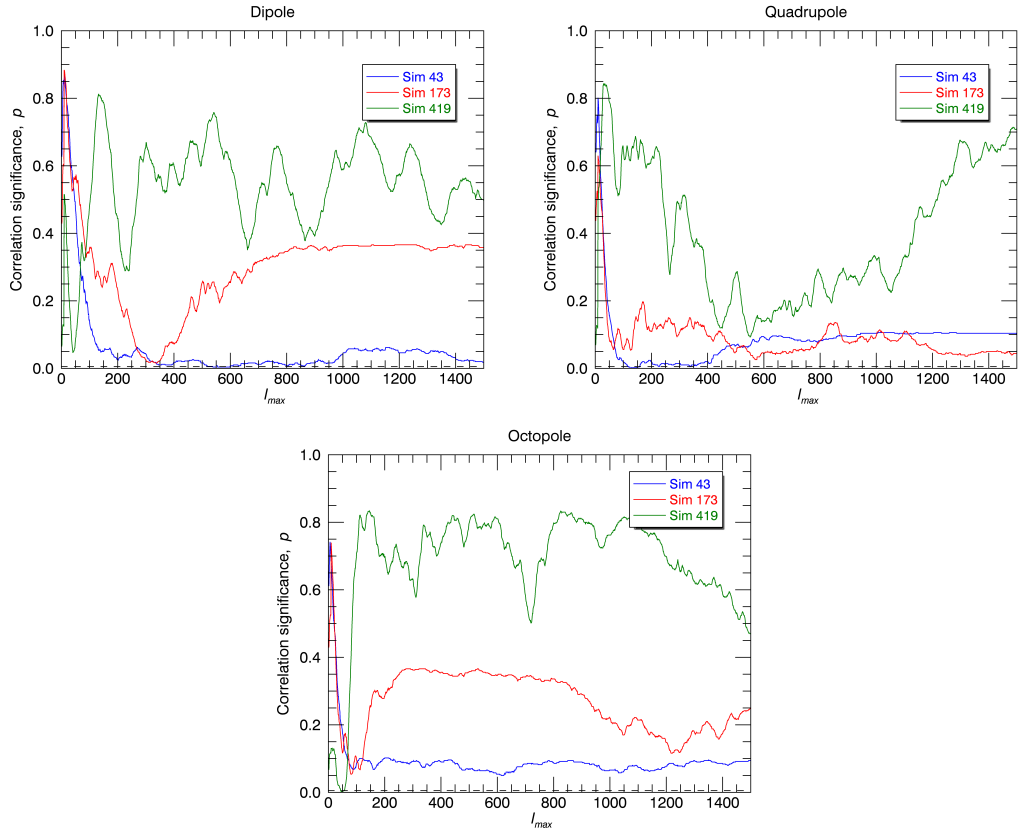

Figure 5.16: Significance of the correlation between multipoles in three (number 43, 173 and 419) randomly chosen simulations compared to all other simulations. The correlation of the dipole components are shown in the top left, quadrupole in top right and octopole at the bottom . The statistics were calculated using the same pseudo-Rayleigh statistic as the angular clustering significance shown in figures 5.5, 5.6, 5.9 and 5.10, but this time using the form given in equation 5.2 instead of equation 3.5.

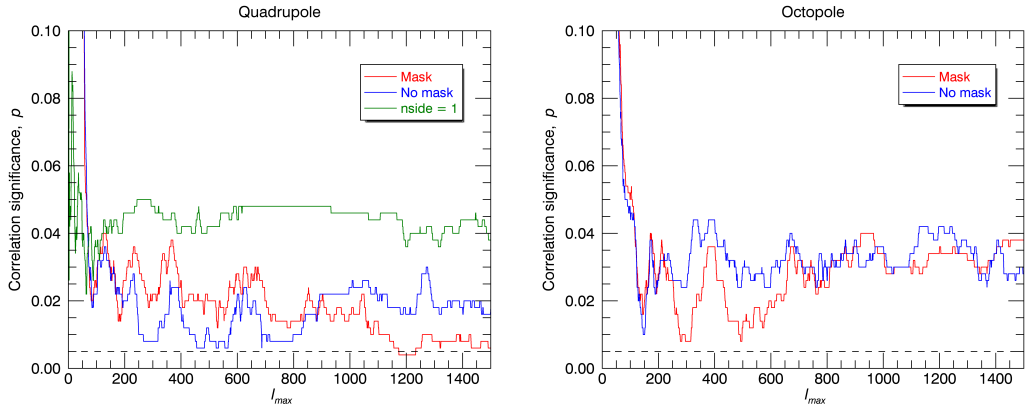

Figure 5.17: Significance of the absolute value of the correlation between power spectrum maps from the observed data compared to simulations. The correlation of the dipole components are shown in the top left, quadrupole in top right and octopole at the bottom. The statistics were calculated using the same pseudo-Rayleigh statistic as the angular clustering significance shown in figures 5.5, 5.6, 5.9 and 5.10, but this time using the form given in equation 5.2 instead of equation 3.5.

goes down compared to the figure in 5.15. If we only view the *alignment*, there is no signficiant difference between the simulations and the data. Since we pick up both anti-correlated and correlated maps in the significance, this also happens for the simulations. Apparently there are more anti-correlated results in the simulations than the data, and doing a significance analysis that also pick these up brings the behaviour of the data closer to the simulations. So the analysis of the alignment only results in a non-detection, but the actual correlation leads to a close to significant detection in the octopole, but not in the dipole unlike the angular clustering analysis.

Chapter 6

Discussion of Possible Errors & Improvements

6.1 No one ever shouts eureka, they just mumble *"That's odd..."*

The goal in this thesis is to continue the angular clustering analysis performed on the Planck data and extend it to higher orders. The cross checking performed in section 5.1 show that our solution of the spherical harmonic matrix performs adequately well in both the direction check and correlation check, apart from an odd behavior in the dipole components. One of the curious result of our significance analysis is the apparent lack of angular clustering of the dipole in the correlation analysis. The reason for this is still unclear and should be investigated more thoroughly, but considering the cross check result of the dipole there may be some connection. Still, if that was the case we would also expect to see a lack of clustering in the directional analysis, at least in the result estimated by our method, and as such this odd behavior is most likely the result of an unknown bug.

Looking at table 5.4 we see that both the mean angular distance and correlation lead to similar averages in our method. For the dipole components these two analysis are equivalent, both giving a strong similarity between the maps if the average is approximately equal 1. Both of these measurements of similarity denote a strong significance as a value of 1 ($\cos 0^\circ = 1$), no similarity as 0, and negatives of each other as -1 ($\cos 180^\circ = -1$). A similar value then means that both measurements find on average the same level of similarity between the maps. The fact that we then do not observe a significant detection when using correlation to estimate the angular clustering on any resolution other than $N_{\text{side}} = 1$ maps, and even then only in the very limit of what can be called significant, is curious. The oscillating correlation coefficients might be the result of a bug somewhere in the code, in that case before the estimation is done since the fault is seen in both estimates. A more thorough investigation of the reconstruction of dipole components, both in the code developed here and the expected precision of the dipole estimation with maps containing structures past $l = 1$, is needed in order to see where this discrepancy arises. Unfortunately the deadline of this thesis is fast approaching and there is not enough time.

Another curious result is the now apparent significant clustering of octopole components, calculated from the correlation coefficients. The fact that this detection is only present when the anti-correlated result is not counted as a detection, e.g. when we do not use the absolute value

of the correlation coefficient as a general measure of alignment, tells us that the detection is not just of the alignment, but of the actual distribution of higher and lower values of the power spectrum maps. But, this detection as we have referred to it up until this point, is still in the very limit of what we could count as a detection. Approximately 0.5 % of simulation exhibit a similarity across multipoles of this degree. Which is perfectly possible in maps with fluctuations generated from random processes like the CMB, it is just unlikely and unlikely does not mean impossible.

A possible criticism of this result is that our correlation results only evaluate the distribution of stronger and weaker pixels across the map, not the actual amplitude. We normalize the maps before the correlation analysis is performed because it is only the distribution that interests us. If the amplitudes had been taken into account we would most likely have achieved weaker correlations across multipoles from the varying amplitude in the power spectrum itself. The angular clustering analysis avoided this problem by only using the spherical coordinates with no information on the "radius of the sphere". We feel that since this a generalization of the angular clustering and is only an investigation of the possible presence of asymmetry, it makes sense to ignore the amplitude information for now, until we have a better way of incorporating the expected variations in amplitude from the variations in the power spectrum. Maybe by normalizing the pixels with the expected value of the power spectrum at the multipole in question.

Another flaw in the correlation analysis is that it as mentioned, only measures the similarities between the maps. At the end of the analysis we do not have any information on the actual distribution of stronger and weaker pixels, like the direction in the dipole or the average placement of the strong and weak spots in the quadrupole and octopole. This can cause problems if the result is to be compared to other analyses, i.e large scale structures, to see if we see signs of the same asymmetry in other types of experiments. We need to implement a more fitting analysis that also incorporates this information. Until then the analysis is incomplete, and we are left with only a part of the total picture.

6.2 Potential Improvements and Future Analysis

With the pseudo-Rayleigh statistic (equation 3.5) used in the analysis of significance, one very important aspect to question is the validity of our test statistic. Since we do not implement a "normal" test statistic in order to assess the significance of the angular clustering or correlation in the data, the normal definition of what is significant might not be a correct way to quantify our results. We have assumed that the maps at each multipole does not have normal distributed values across the simulations. The main reason that we concluded this is the law of large numbers, which states that as the numbers of samples increases the distribution will tend towards a normal distribution (Vittinghoff et al., 2011). Without time to check the actual statistical properties of our samples and only operating with 500 maps, it is risky to assume that the data is close to normal distributed. It would have been interesting to analyze these statistical properties and run more simulations in order to achieve a level of normality that would allow more accurate hypothesis testing. Most non-parametric hypothesis tests that can handle data that are not normal distributed are based on ranking the data, which quickly becomes very complicated with continuous data, requiring consideration in how the ranking is performed and often result in significances that are less reliable than test statistics that require close to normal distributed

data (Vittinghoff et al., 2011) [1].

Another problem occurring from the small number of simulations used is the calibration. We mentioned in chapter 3 that we weight the data and simulations by maps of the standard deviation of the simulations at each multipole. We are in a way creating a dependence across the simulated maps where by having the sigma dependent on all maps, and the weighted maps can then to a certain degree be correlated across the simulations. This can potentially affect the correlation analysis, but to which degree is uncertain until an analysis is repeated with the calibration calculated from simulations not used in the significance analysis. We could have split the simulations into two parts, 250 used for calibration and 250 used for analysis, but the number of samples used in that case would be too few to be able to draw any conclusion. This calibration defines what we view as an "expected result" in the sense that exactly 67 % of the calibration simulations are within 1σ significance and exactly 95 % are within 2σ by construction. Using a different data set for the calibrations ensures that it isn't only the observed data that deviates noticeable from these limits, and may help even out the result. The more simulations we have, the less this will be a potential problem, but with our 500 simulations we cannot discount this as a possible reason for e.g. the borderline detection in the octopole.

Finally, it might also be interesting to investigate the correlation occurring between the reconstructed maps of the estimated dipole, quadrupole and octopole components of the power spectrum maps in order to investigate if the detection found in octopole is a result of what we observed in the dipole in the angular clustering analysis. The significance found using the correlation analysis when running simulations through the same calculations as the data is shown in figure 5.16, and resulted in remarkably similar p-values for dipole, quadrupole and octopole. The maps used in the correlation were constructed from only the coefficients at the specific multipole, e.g. the octopole maps are created from only the a_{lm} coefficient with $l = 3$, all other multipoles l are set to 0. The fact that we still get p-values that are similar across dipole, quadrupole and octopole is curious. There is no apparent reason that this should be the case, unless there is some unknown connection between the first three multipoles of the maps reconstructed from the estimated spherical harmonic coefficients. If there is a correlation between the maps it would mean that the results found here are not necessarily in opposition to what was published in the Planck 2015 isotropy article, but that we pick up the correlation in the octopole instead of the dipole.

[1] During the investigation of viable alternatives to the Rayleigh statistic it quickly became obvious why all the statistical analysis introduced to us up to this point in our education were based on more or less normal distributed data.

Chapter 7

Summary & Conclusion

The goal in this thesis is to continue the angular clustering analysis performed on the Planck data and extend it to higher orders. We sought to build upon the analysis performed in Axelsson et al. (2013), Ade et al. (2014f) and Ade et al. (2016c) in order to investigate the assumption of isotropy in the universe. Specifically we wanted to investigate whether there is any significant quadru- and octopolar asymmetry in the CMB in the same way as there were indications of dipolar asymmetry in both the WMAP and Planck data by analysing the distribution of power in the CMB across multipoles (Ade et al., 2016c) (Ade et al., 2014f) (Eriksen et al., 2004). To achieve this we generalized the HEALPix code `remove_dipole` in order to extract the underlying spherical harmonic coefficients up to $l = 3$ (octopole), and implemented the definition of direction for quadrupole and octopole components given in de Oliveira-Costa et al. (2004).

The data used in these analyses are the Planck public release 2, freely available in the *Planck Legacy Archive*. The simulations were run through the FFP8 framework to simulate the effects caused by the observation. We use 500 of these simulated maps and a set of observational data. The effects of foreground have been removed from the data using the SMICA method, and the data and simualtions are all masked using the confidence mask U73.

The maps (simualtion and observational data) are partitioned into HEALPix $N_{\text{side}} = 1$ and $N_{\text{side}} = 2$ maps, and a power spectrum is calculated in each patch. This results in one map for each multipole, with pixel values equal to the power spectrum C_l in that pixel. We then estimate the spherical harmonics coefficient for each of the power spectrum maps, and an angular clustering analysis or correlation analysis is performed. The pseudo-Rayleigh statistic is then implemented in order to calculate the significance of angular clustering between maps at each multipole in the data compared to the simulations, or to estimate the correlation between maps at each multipole compared to the data. The significance gives us the amount of simulation with a higher correlation or angular clustering than the data, and a high significance is then a sign of a di-, quadru- or octopolar asymmetry in the sky.

We find that the estimation of angular clustering found with our method is in agreement with the results published in the Planck 2015 isotropy article (Ade et al., 2016c), and that an increase in resolution strengthens the significance in some multipole ranges. For the quadrupole and octopole components we find no significant clustering in any multipole ranges, but there are signs of a striking lack of clustering in the octopole. The correlation analysis results in a lack of correlation in the dipole components, but a borderline detection in the octopole, still with no detection in the quadrupole. This discrepancy between the angular clustering and

correlatioon analysis of the dipole is odd, but can be a result of unkown correlation between the reconstructed dipole quadrupole and octople maps, potentially causing the dipole detection to show up in the octopole instead.

From the cross checking performed in sectio 5.1 it appears that the method developed here works as intended, with the exception of an odd result in the dipole. The advantage with implementing the correlation analysis is that we avoid the complex problem of defining a direction for the quadrupole and octopole, but we also lose all information on direction in the detection. There seem to be a detection, but we do not know the direction in which maps are tending to point in. To do this we need to define a direction, but the definition of direction used here may have problems in finding a correct direction in maps that do not have significantly planar components.

In conclusion, the method developed for the estimation of the sphericalm harmonic coefficients up to $l = 3$ seem to perform as adequately well, on the same level as `remove_dipole` in the dipole case, but the results still need more processing. Specifically, we need to repeat this analysis on more than 500 maps and with calibration not performed by the same maps as the ones used in the analysis in order to see if the tentative correlation detection in the octople changes.

Appendix A

Matrix Equation Calculations

A.1 Analytical form of spherical harmonic coefficients a_{10} and a_{11}

Below are the calculations done in order to find the analytical expressions for the spherical harmonics coefficients using the spherical harmonics given in equation 2.4 - 2.12, setting the temperature map as a dipole, $T(\theta,\phi) = A\left[\cos(\theta_p)\cos(\theta) + \sin(\theta_p)\sin(\theta)\cos(\phi_p - \phi)\right]$.

$\underline{l = 1, m = 0}$:

$$
\begin{aligned}
a_{10} &= \iint T(\theta,\phi) Y_{10}^{*}(\theta,\phi)\sin\theta d\theta d\phi \\
&= \frac{A}{2}\sqrt{\frac{3}{\pi}}\int_0^{2\pi}\int_0^{\pi}\left[\cos(\theta_p)\cos(\theta) + \sin(\theta_p)\sin(\theta)\cos(\phi_p - \phi)\right]\cos\theta\sin\theta d\theta d\phi \\
&= \frac{A}{2}\sqrt{\frac{3}{\pi}}\cos\theta_p \iint \cos^2\theta\sin\theta d\theta d\phi + \frac{A}{2}\sqrt{\frac{3}{\pi}}\sin\theta_p \iint \sin^2\theta\cos\theta\cos(\phi_p - \phi) d\theta d\phi
\end{aligned}
$$

$$
\iint cos^2\theta\sin\theta d\theta d\phi = \int_0^{\pi}\cos^2\theta\sin\theta\int_0^{2\pi} d\phi d\theta = 2\phi\int_0^{\pi}\cos^2\theta\sin\theta d\theta = \frac{4\pi}{3}
$$

$$
\begin{aligned}
\iint \sin^2\theta\cos\theta\cos(\phi_p - \phi) d\theta d\phi &= \int_0^{\pi}\sin^2\theta\cos\theta\int_0^{2\pi}\cos(\phi_p - \phi) d\phi d\theta \\
&= \int_0^{\pi}\sin^2\theta\cos\theta\int_0^{2\pi}\sin(\phi_p)\sin(\phi) + \cos(\phi_p)\cos(\phi) d\phi d\theta \\
&= 0
\end{aligned}
$$

$$
\implies \quad a_{10} = \frac{A}{2}\sqrt{\frac{3}{\pi}}\frac{4\pi}{3}\cos(\theta_p) = 2A\sqrt{\frac{\pi}{3}}\cos\theta_p
$$

$\underline{l = 1, m = 1}$:

$$
\begin{aligned}
a_{11} &= \frac{-A}{2}\sqrt{\frac{3}{2\pi}}\iint \Big[\cos(\theta_p)\cos(\theta) + \sin(\theta_p)\sin(\theta)\cos(\phi_p - \phi)\Big]\sin^2\theta e^{-i\phi} d\phi d\theta \\
&= \frac{-A}{2}\sqrt{\frac{3}{2\pi}}\cos\phi_p \iint \cos\theta \sin^2\theta e^{-i\phi} d\phi d\theta \\
&\quad - \frac{A}{2}\sqrt{\frac{3}{2\pi}}\sin\phi_p \iint \sin^3\theta\cos(\phi_p - \phi) e^{-i\phi} d\phi d\theta \\
&= \frac{-A}{2}\sqrt{\frac{3}{2\pi}}\cos\theta_p \int_0^{\pi}\cos\theta\sin^2\theta\int_0^{2\pi} e^{-i\phi} d\phi d\theta \quad \left(\int_0^{2\pi} e^{-i\phi} d\phi = 0\right) \\
&\quad - \frac{A}{2}\sqrt{\frac{3}{2\pi}}\sin\theta_p \int_0^{\pi}\sin^3\theta\int_0^{2\pi}\cos(\phi_p - \phi) e^{-i\phi} d\phi d\theta \\
&= \frac{-A}{2}\sqrt{\frac{3}{2\pi}}\sin\theta_p \int_0^{\pi}\sin^3\theta\int_0^{2\pi}\cos(\phi_p - \phi) e^{-i\phi} d\phi d\theta, \quad \int_0^{2\pi}\cos(\phi_p - \phi) e^{-i\phi} d\phi = \pi e^{-i\phi_p} \\
&= \frac{-A}{2}\sqrt{\frac{3}{2\pi}}\pi e^{-i\phi_p}\sin\theta_p \int_0^{\pi}\sin^3\theta d\theta = \frac{-A}{2}\sqrt{\frac{3}{2\pi}}\frac{4\pi}{3}\sin\theta_p e^{-i\phi} \\
&= -A\sqrt{\frac{2\pi}{3}}\sin\theta_p\cos\phi_p + iA\sqrt{\frac{2\pi}{3}}\sin\theta_p\sin\phi_p
\end{aligned}
$$

These calculation results in the form below, using the relation between positive and negative phases, $a_{l-m} = (-1)^m a^*_{lm}$

$$a_{10} = 2A\sqrt{\frac{\pi}{3}}\cos\theta_p \tag{A.1}$$

$$a_{11} = -A\sqrt{\frac{2\pi}{3}}\sin\theta_p\cos\phi_p + iA\sqrt{\frac{2\pi}{3}}\sin\theta_p\sin\phi_p \tag{A.2}$$

$$a_{1-1} = A\sqrt{\frac{2\pi}{3}}\sin\theta_p\cos\phi_p + iA\sqrt{\frac{2\pi}{3}}\sin\theta_p\sin\phi_p \tag{A.3}$$

A.2 Extensive Calculation on the a_{lm} matrix for $l_{\max} = 2$

The calculations and expansions done on equation 4.1 in order to create the quadrupole matrix are listed below. The elements are simply expanded versions of the equation given in 4.9, split into real and imaginary parts on both sides of the equating sign. This leaves us with a vector consisting of real and imaginary parts of the pseudo sphercal harmonics on the left side, $\tilde{a}_{lm}$, and a vector of the same form with the underlying spherical harmonics $a_{l'm'}$ on the right side. The matrix consists of spherical harmonics multiplied by the pixel area in each pixel k, masked, and summed over pixels. Each element in the matrix then has the form

$$R_{ll'mm'} = \Delta_{\text{pix}} \sum_k M_k Y^{k*}_{lm} Y_{l'm'}$$

Since there is no l or m dependence in the masking and pixel area, we simply pull these factors outside matrix and spherical harmonics vector.

$$\begin{aligned}
\tilde{a}_{00} &= \sum_k \Delta_{\text{pix}} M_k [a_{00}(Y^k_{00})^2 + a_{10} Y^k_{10} Y^k_{00} + 2a^r_{11}\mathcal{R}\{Y_{11}\}^k Y^k_{00} - 2a^i_{11}\mathcal{I}\{Y_{11}\}^k Y^k_{00} + a_{20} Y^k_{20} Y^k_{00} \\
&\quad + 2a^r_{21}\mathcal{R}\{Y_{21}\}^k Y^k_{00} - 2a^i_{21}\mathcal{I}\{Y_{21}\}^k Y^k_{00} + 2a^r_{22}\mathcal{R}\{Y_{22}\}^k Y^k_{00} - 2a^i_{22}\mathcal{I}\{Y_{22}\}^k Y^k_{00}] \\
\tilde{a}_{10} &= \sum_k \Delta_{\text{pix}} M_k [a_{00} Y^k_{00} Y^k_{10} + a_{10}(Y^k_{10})^2 + 2a^r_{11}\mathcal{R}\{Y_{11}\}^k Y^k_{10} - 2a^i_{11}\mathcal{I}\{Y_{11}\}^k Y^k_{10} + a_{20} Y^k_{20} Y^k_{10} \\
&\quad + 2a^r_{21}\mathcal{R}\{Y_{21}\}^k Y^k_{10} - 2a^i_{21}\mathcal{I}\{Y_{21}\}^k Y^k_{10} + 2a^r_{22}\mathcal{R}\{Y_{22}\}^k Y^k_{10} - 2a^i_{22}\mathcal{I}\{Y_{22}\}^k Y^k_{10}] \\
\tilde{a}^r_{11} &= \sum_k \Delta_{\text{pix}} M_k [a_{00} Y^k_{00}\mathcal{R}\{Y_{11}\}^k + a_{10} Y^k_{10}\mathcal{R}\{Y_{11}\}^k + 2a^r_{11}\left(\mathcal{R}\{Y_{11}\}^k\right)^2 - 2a^i_{11}\mathcal{I}\{Y_{11}\}^k\mathcal{R}\{Y_{11}\}^k + a_{20} Y^k_{20}\mathcal{R}\{Y_{11}\}^k \\
&\quad + 2a^r_{21}\mathcal{R}\{Y_{21}\}^k\mathcal{R}\{Y_{11}\}^k - 2a^i_{21}\mathcal{I}\{Y_{21}\}^k\mathcal{R}\{Y_{11}\}^k + 2a^r_{22}\mathcal{R}\{Y_{22}\}^k\mathcal{R}\{Y_{11}\}^k - 2a^i_{22}\mathcal{I}\{Y_{22}\}^k\mathcal{R}\{Y_{11}\}^k] \\
\tilde{a}^i_{11} &= \sum_k \Delta_{\text{pix}} M_k [-a_{00} Y^k_{00}\mathcal{I}\{Y_{11}\}^k - a_{10} Y^k_{10}\mathcal{I}\{Y_{11}\}^k - 2a^r_{11}\mathcal{R}\{Y_{11}\}^k\mathcal{I}\{Y_{11}\}^k + 2a^i_{11}\left(\mathcal{I}\{Y_{11}\}^k\right)^2 - a_{20} Y^k_{20}\mathcal{I}\{Y_{11}\}^k \\
&\quad - 2a^r_{21}\mathcal{R}\{Y_{21}\}^k\mathcal{I}\{Y_{11}\}^k + 2a^i_{21}\mathcal{I}\{Y_{21}\}^k\mathcal{I}\{Y_{11}\}^k - 2a^r_{22}\mathcal{R}\{Y_{22}\}^k\mathcal{I}\{Y_{11}\}^k + 2a^i_{22}\mathcal{I}\{Y_{22}\}^k\mathcal{I}\{Y_{11}\}^k] \\
\tilde{a}_{20} &= \sum_k \Delta_{\text{pix}} M_k [a_{00} Y^k_{00} Y^k_{20} + a_{10} Y^k_{10} Y^k_{20} + 2a^r_{11}\mathcal{R}\{Y_{11}\}^k Y^k_{20} - 2a^i_{11}\mathcal{I}\{Y_{11}\}^k Y^k_{20} + a_{20}(Y^k_{20})^2 \\
&\quad + 2a^r_{21}\mathcal{R}\{Y_{21}\}^k Y^k_{20} - 2a^i_{21}\mathcal{I}\{Y_{21}\}^k Y^k_{20} + 2a^r_{22}\mathcal{R}\{Y_{22}\}^k Y^k_{20} - 2a^i_{22}\mathcal{I}\{Y_{22}\}^k Y^k_{20}] \\
\tilde{a}^r_{21} &= \sum_k \Delta_{\text{pix}} M_k [a_{00} Y^k_{00}\mathcal{R}\{Y_{21}\}^k + a_{10} Y^k_{10}\mathcal{R}\{Y_{21}\}^k + 2a^r_{11}\mathcal{R}\{Y_{11}\}^k\mathcal{R}\{Y_{21}\}^k - 2a^i_{11}\mathcal{I}\{Y_{11}\}^k\mathcal{R}\{Y_{21}\}^k + a_{20} Y^k_{20}\mathcal{R}\{Y_{21}\}^k \\
&\quad + 2a^r_{21}\left(\mathcal{R}\{Y_{21}\}^k\right)^2 - 2a^i_{21}\mathcal{I}\{Y_{21}\}^k\mathcal{R}\{Y_{21}\}^k + 2a^r_{22}\mathcal{R}\{Y_{22}\}^k\mathcal{R}\{Y_{21}\}^k - 2a^i_{22}\mathcal{I}\{Y_{22}\}^k\mathcal{R}\{Y_{21}\}^k] \\
\tilde{a}^i_{21} &= \sum_k \Delta_{\text{pix}} M_k [-a_{00} Y^k_{00}\mathcal{I}\{Y_{21}\}^k - a_{10} Y^k_{10}\mathcal{I}\{Y_{21}\}^k - 2a^r_{11}\mathcal{R}\{Y_{11}\}^k\mathcal{I}\{Y_{21}\}^k + 2a^i_{11}\mathcal{I}\{Y_{11}\}^k\mathcal{I}\{Y_{21}\}^k - a_{20} Y^k_{20}\mathcal{I}\{Y_{21}\}^k \\
&\quad - 2a^r_{21}\mathcal{R}\{Y_{21}\}^k\mathcal{I}\{Y_{21}\}^k + 2a^i_{21}\left(\mathcal{I}\{Y_{21}\}^k\right)^2 - 2a^r_{22}\mathcal{R}\{Y_{22}\}^k\mathcal{I}\{Y_{21}\}^k + 2a^i_{22}\mathcal{I}\{Y_{22}\}^k\mathcal{I}\{Y_{21}\}^k] \\
\tilde{a}^r_{22} &= \sum_k \Delta_{\text{pix}} M_k [a_{00} Y^k_{00}\mathcal{R}\{Y_{22}\}^k + a_{10} Y^k_{10}\mathcal{R}\{Y_{22}\}^k + 2a^r_{11}\mathcal{R}\{Y_{11}\}^k\mathcal{R}\{Y_{22}\}^k - 2a^i_{11}\mathcal{I}\{Y_{11}\}^k\mathcal{R}\{Y_{22}\}^k + a_{20} Y^k_{20}\mathcal{R}\{Y_{22}\}^k \\
&\quad + 2a^r_{21}\mathcal{R}\{Y_{21}\}^k\mathcal{R}\{Y_{22}\}^k - 2a^i_{21}\mathcal{I}\{Y_{21}\}^k\mathcal{R}\{Y_{22}\}^k + 2a^r_{22}\left(\mathcal{R}\{Y_{22}\}^k\right)^2 - 2a^i_{22}\mathcal{I}\{Y_{22}\}^k\mathcal{R}\{Y_{22}\}^k] \\
\tilde{a}^i_{22} &= \sum_k \Delta_{\text{pix}} M_k [-a_{00} Y^k_{00}\mathcal{I}\{Y_{22}\}^k - a_{10} Y^k_{10}\mathcal{I}\{Y_{22}\}^k - 2a^r_{11}\mathcal{R}\{Y_{11}\}^k\mathcal{I}\{Y_{22}\}^k + 2a^i_{11}\mathcal{I}\{Y_{11}\}^k\mathcal{I}\{Y_{22}\}^k - a_{20} Y^k_{20}\mathcal{I}\{Y_{22}\}^k \\
&\quad - 2a^r_{21}\mathcal{R}\{Y_{21}\}^k\mathcal{I}\{Y_{21}\}^k + 2a^i_{21}\mathcal{I}\{Y_{21}\}^k\mathcal{I}\{Y_{22}\}^k - 2a^r_{22}\mathcal{R}\{Y_{22}\}^k\mathcal{I}\{Y_{22}\}^k + 2a^i_{22}\left(\mathcal{I}\{Y_{22}\}^k\right)^2]
\end{aligned}$$

Appendix B

Short explanations on routines and packages used in this thesis

B.1 HEALPix

In this thesis HEALPix (Gorski et al., 2005), the "the Hierarchical Equal Area isoLatitude Pixelization", v3.2 is used to perform spherical harmonic transformations back and forth between power spectrum, coefficients and maps for given resolutions $N_{\rm side}$ and maximum multipole $l_{\rm max}$. It is a pixelation scheme specifically meant to optimize analysis spherical sky maps and their projections. As stated in Gorski et al. (2005), *"The simplicity of the spherical form belies the intricacy of global analysis on the sphere. There is no known point set that achieves the analog of uniform sampling in Euclidean space and allows exact and invertible discrete spherical harmonic decompositions of arbitrary but band-limited functions"*. This complication gave rise to many different methodologies to accomplish relatively fast map analysis on the sphere, including, but not limited to, spherical harmonics analysis, power spectrum estimation, wavelet/needlet decompositions and nearest neighbor searches.

In particular, the HEALPix pixelation provides pixelation schemes that constructs pixels of equal surface area no matter what position on the sphere they are placed. An example of the base pixel resolution given by $N_{\rm side} = 1$ is shown in figure B.1, with higher resolutions over plotted for comparison (Gorski et al., 2005). The base resolution $N_{\rm side} = 1$ was defined from the parameters $N_\theta = 3$ and $N_\phi = 4$, describing the total number of pixel cuts on the map between north and south, and across the equator of the map respectively, with the relation to the total number of pixels given as $N_{\rm pix} = 12N_{\rm side}^2$. The parameter $N_{\rm side}$ then gives the number of cuts along the side of the base pixel. This ensured that the angle between the pixels at the poles did not become acute, that the elongation of pixels along the equator was as small as possible and that we retained a 2^n multiplicity of pixels around the equator to enable efficient spherical harmonic transforms Gorski et al. (2005). The angular resolution of the pixels is then expressed as $\theta_{\rm pix} = \sqrt{\frac{3}{\pi N_{\rm side}^2}}$ (in degrees) with a pixel area given by $\Omega_{\rm pix} = 4\pi/N_{\rm pix} = \pi/3N_{\rm side}^2$.

HEALPix supports two different pixelation numbering scheme, the ring scheme and the nested scheme. The nested scheme creates a sort of tree structure in the numbering as shown in figure B.2, and is especially suited for nearest-neighbor searches and Haar wavelet transform (Gorski et al. (2005) and references within). The ring scheme on the other hand is much more suited

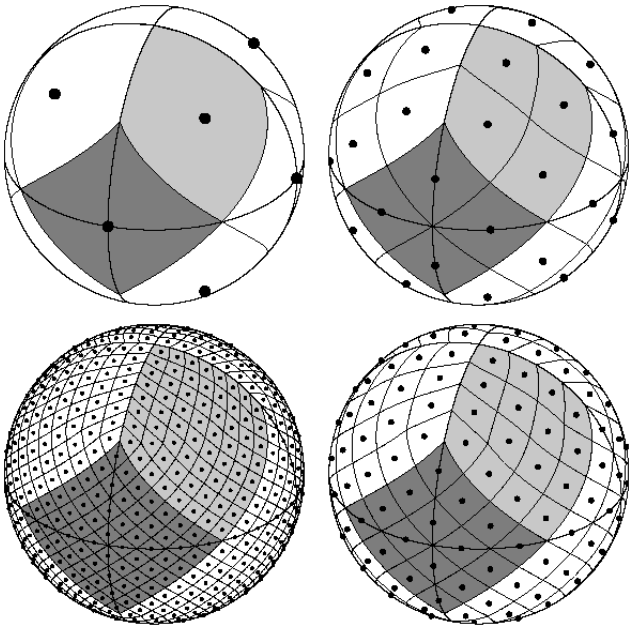

Figure B.1: Example HEALPix pixels on a sphere with different pixel resolutions set by the parameter N_{side} using the ring numbering scheme, with the base pixel setup ($N_{\text{side}} = 1$) in the upper right, $N_{\text{side}} = 2$ in the upper right, $N_{\text{side}} = 4$ in the bottom right and $N_{\text{side}} = 8$ in the bottom left (Gorski et al., 2005).

for effective spherical harmonic transforms, where the pixels are simply numbered by counting from north to south along the each latitude ring. The ring scheme is used exclusively in this thesis, as spheircal harmonic transforms and power spectrum analysis is of primary interest.

All maps shown in this thesis have been produced using the `mollview` package in healpix. `mollview` implements a mollwide projection of the sphere on a flat surface in the same manner as we see on globale maps of the earth. The coordinates are defined as $\theta = 0$ at the north pole, increasing as you move south, and $\phi = 0$ in the centre of the map, increasing to the left. We make use of `map2alm` and the reciprocal `alm2map` to transform maps back and forth between spherical harmonic coefficients and maps, in addition to some basic functions such as `pix2ang` and `pix2vec` in order to transform back and forth between coordinate types. The goal of this thesis is to generalize the `remove_dipole*` routine included in HEALPix , with many of the cross checks and comparisons have been produced with `remove_dipole` and it's reciprocal, `add_dipole`.

.

B.2 Singular Value Decomposition

In order to solve the matrix given in 4.11 we use singular value decomposition, or SVD for short. A theorem from Lay (2006) states:

Let A be an $m \times n$ matrix. Then there exists an $m \times n$ matrix Σ as in B.1 for which the diagonal entries in D are the first r singular values of A, $\sigma_1 \geq \sigma_2 \geq \sigma_3 \geq \ldots \geq \sigma_r > 0$, and there exists

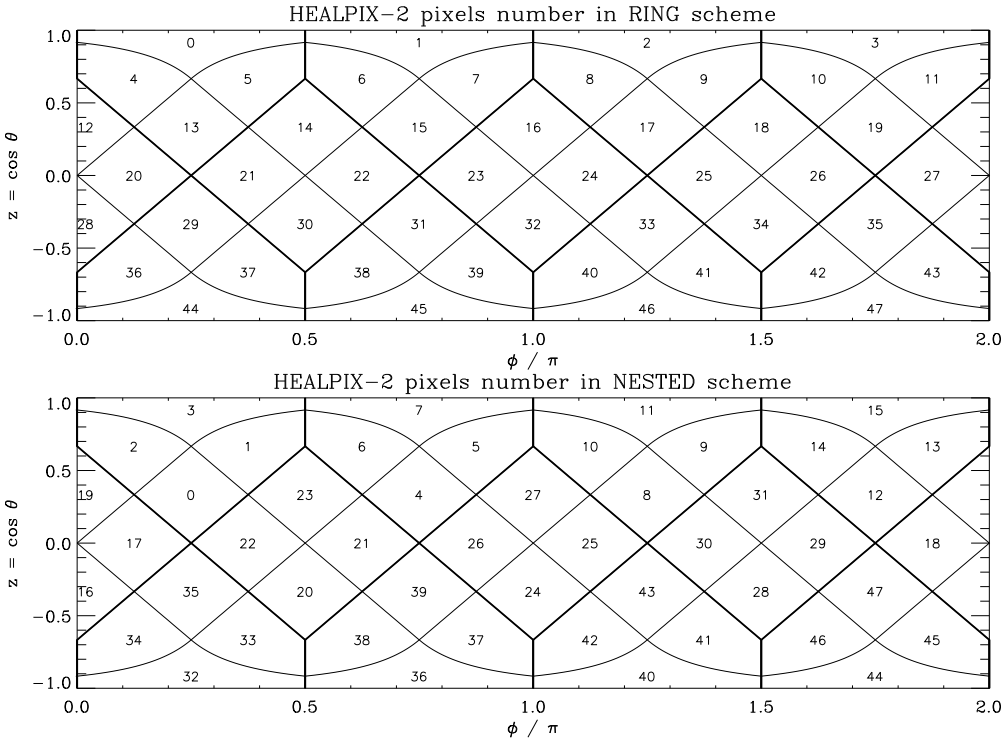

Figure B.2: Numbering scheme examples for Healpix ring (topp) and nested (bottom) Gorski et al. (2005) using $N_{\text{side}} = 2$ resolution. The corrdinates θ and ϕ refers to the colatitude and longitude respectively.

an $m \times m$ orthogonal matrix U and an $n \times n$ orthogonal matrix V such that

$$A = U\Sigma V^T \qquad \Sigma = \begin{pmatrix} D & 0 \\ 0 & 0 \end{pmatrix} \tag{B.1}$$

Basically, any matrix can be decomposed using SVD. In addition, solving matrix equations as in 4.1 becomes trivial, even with non-diagonal matrices, since the matrix Σ is diagonal by definition. The diagonal elements in Σ are given by the *singular values* A, which are defined as the square root of the eigen values. The matrices U and V are often refered to the *left singular vectors* and the *right singular vector* respectively, and are not necessarily uniquely defined by the original matrix A. The matrix V is constructed from the eigenvectors of the matrix A as column vectors, ordered according to the eigenvalues in decreasing order [1]. Finally, the matrix U has columns constructed from the vecotors Av_i weighted by the corresponding singular values, $u_i = Av_i/\sigma_i$.

Inverting an SVD matrix gives is trivial compared to inverting the original matrix. Having a combination of two orthiogonal matrices and a diagonal one, reduces the inverted matrix A^{-1} to

$$A^{-1} = V\Sigma^{-1}U^T, \tag{B.2}$$

[1] If you have the eigenvalues $\lambda_1 > \lambda_2 > \lambda_3$ the columns of the matrix V will be ordered as $[v_1\, v_2\, v_3] = V$, with the eigenvector v_i corresponding to the eigenvalue λ_i.

With the HEALPix package we have access to the single value decomposition algorithm used in the `remove_dipole*` routine, which we continue to use throughout the thesis.

Appendix C

Plots and maps used in 5.1

C.1 Comparison of constructed maps and reconstructed estimates of dipole, quadrupole and octopole maps

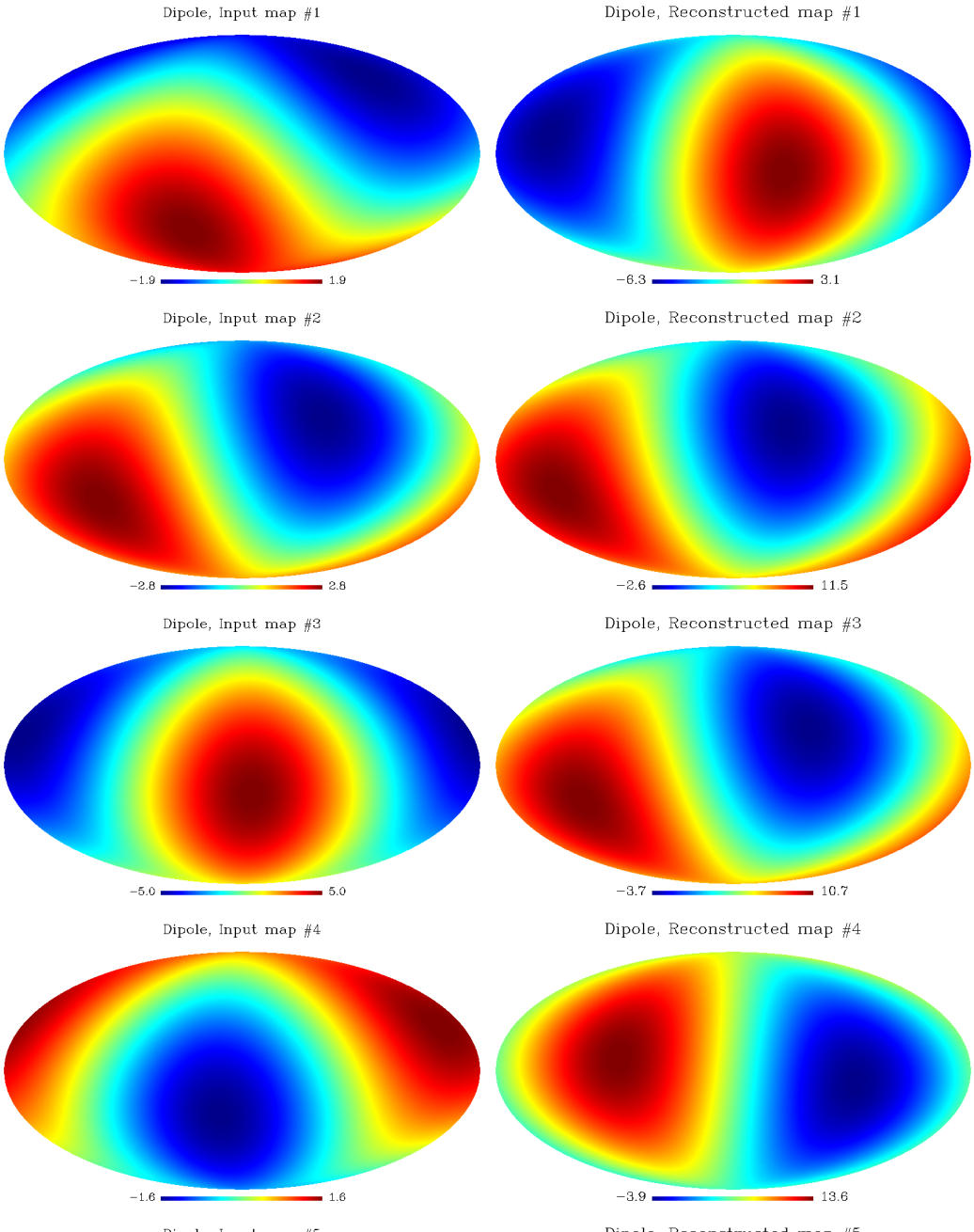

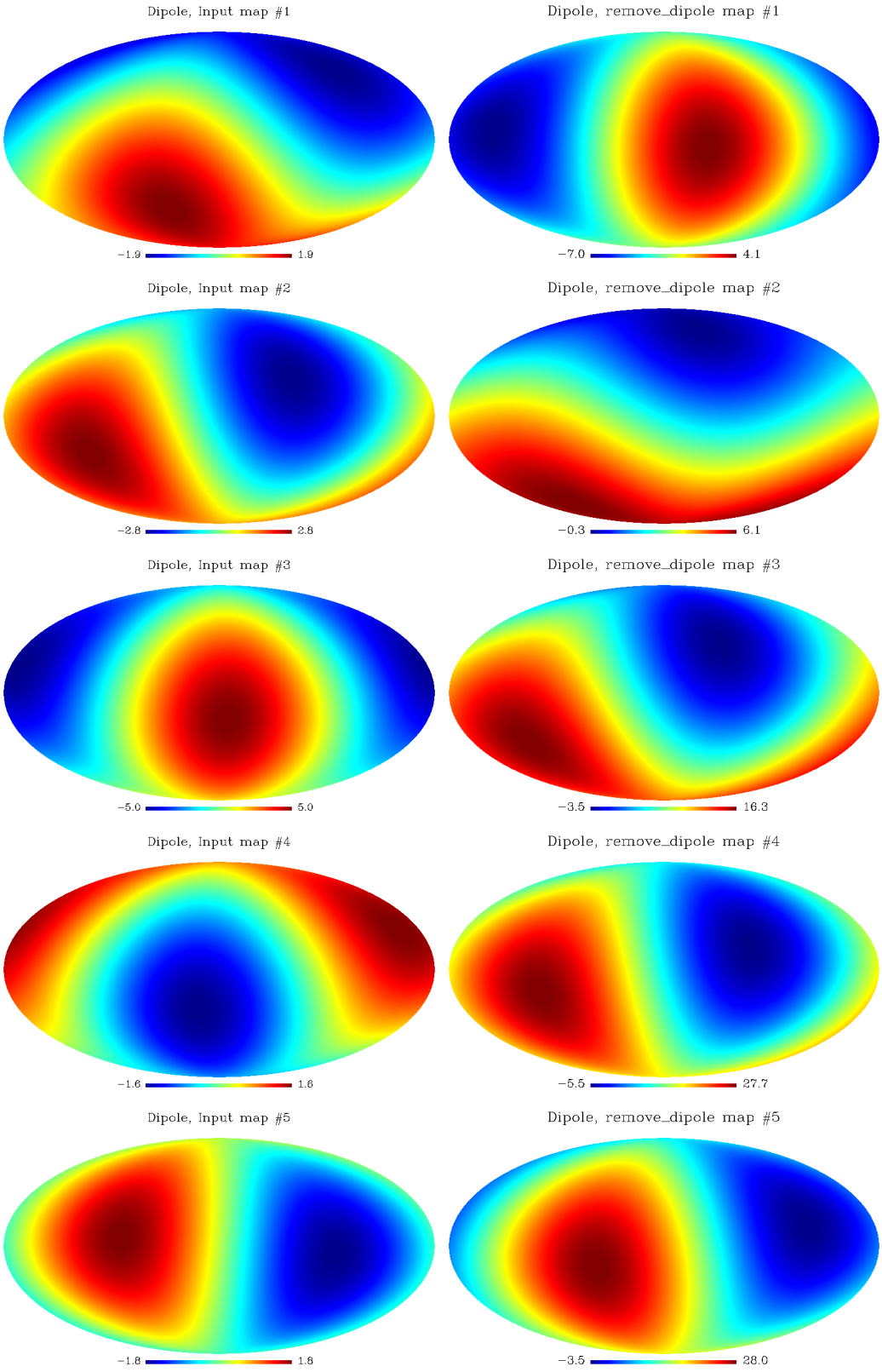

Figure C.2: Comparison between dipole component of input maps and components estimated by the `remove_dipole` routine. Left side shows input maps, right side shows estimate. The maps were generated using the power spectrum up to $l = 200$ available in the HEALPix package, the `create_alm` routine and `alm2map` with $N_{\text{side}} = 128$.

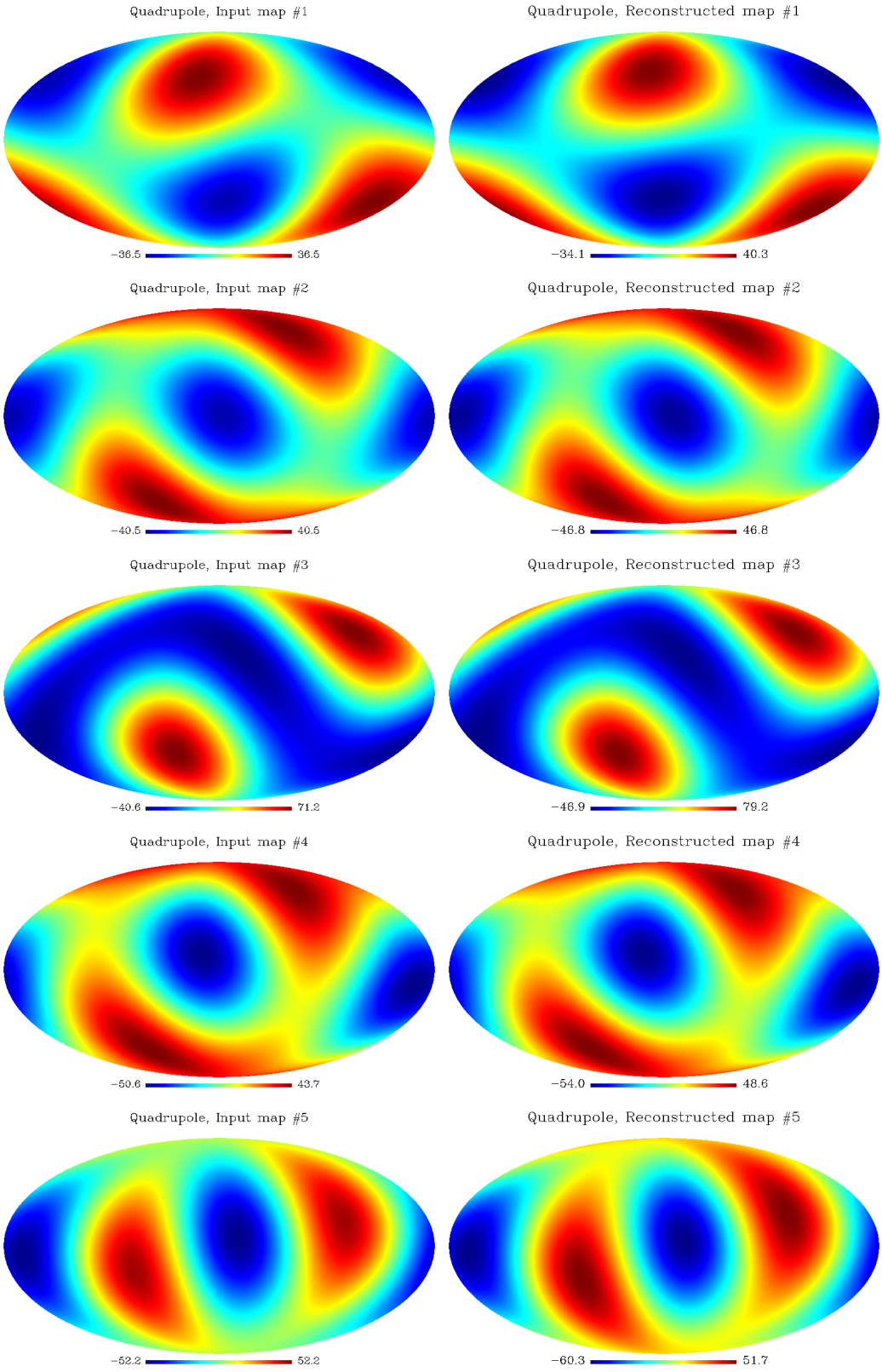

Figure C.3: Comparison between quadrupole component of input quadrupole maps and maps estimated by the routine developed in chapter 4. Left side shows input maps, right side shows estimate. The maps were generated using the power spectrum up to $l = 200$ available in the HEALPix package, the `create_alm` routine and `alm2map`.

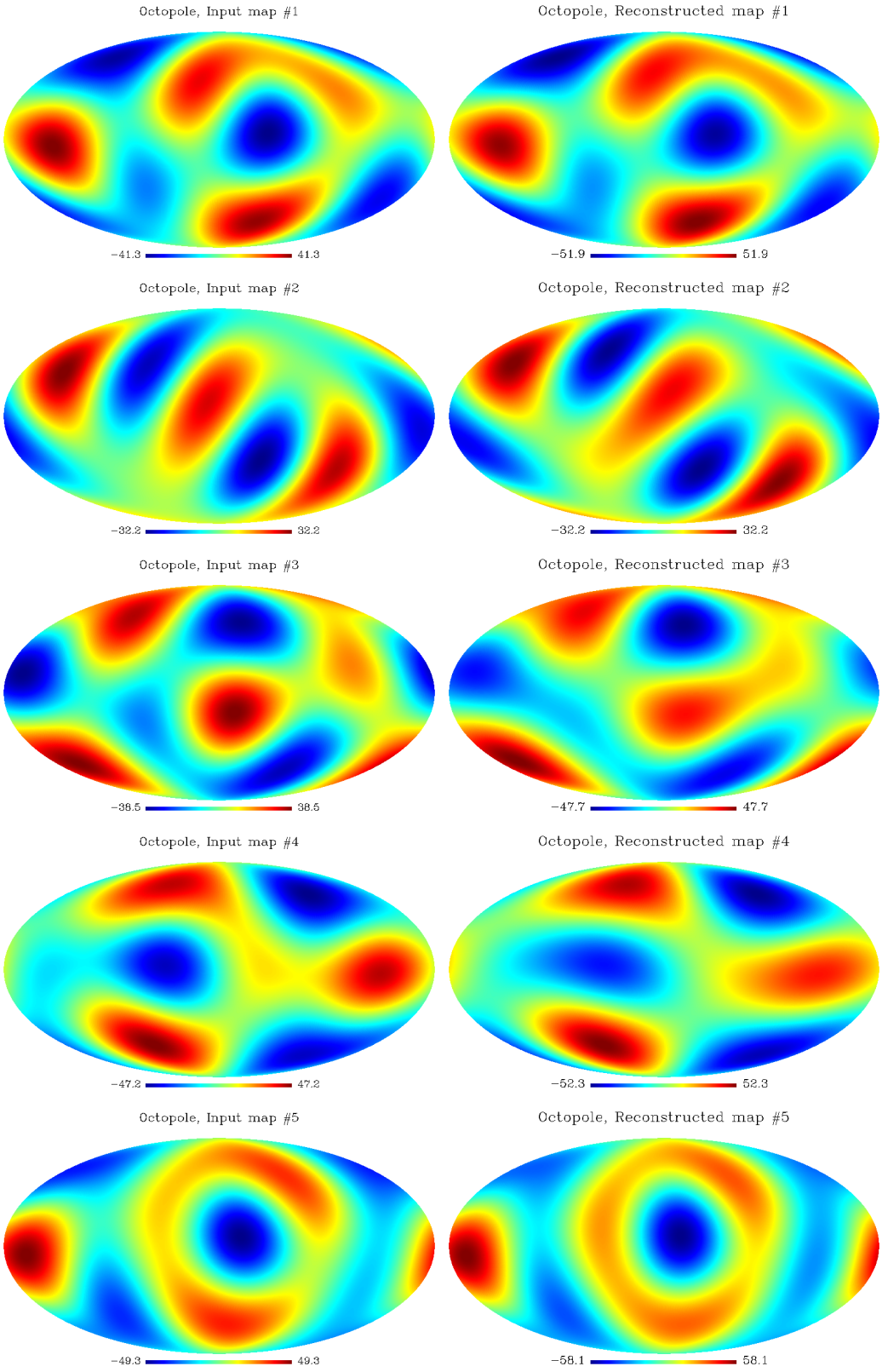

Figure C.4: Comparison between octopole input octopole component maps and maps estimated by the routine developed in chapter 4. Left side shows input maps, right side shows estimate. The maps were generated using the power spectrum up to $l = 200$ available in the HEALPix package, the `create_alm` routine and `alm2map`.

C.2 Powe spectrum plot from a chosen set of pixels for section 5.1

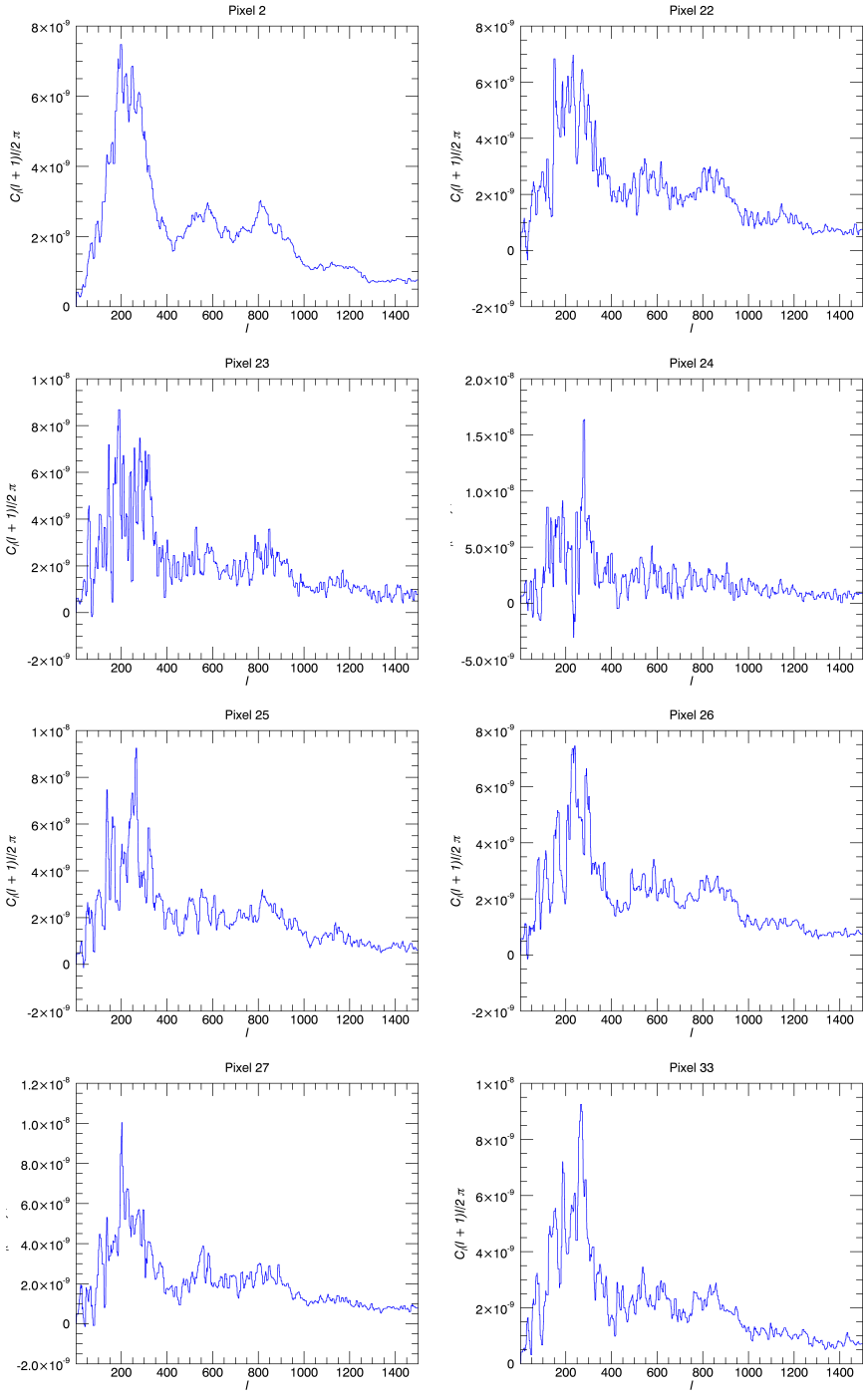

Figure C.5: Plots of continuous power spectrum from a selection of pixels in an $N_{\text{side}} = 2$ map, numbered above the plots. Pixel 22 and onwards are picked out from areas that would be heavily masked by the U73 mask in the power spectrum calculation using the MASTER code. Pixel number 2 is included to demonstrate the appearance of the power spectrum outside of the heavily masked area.

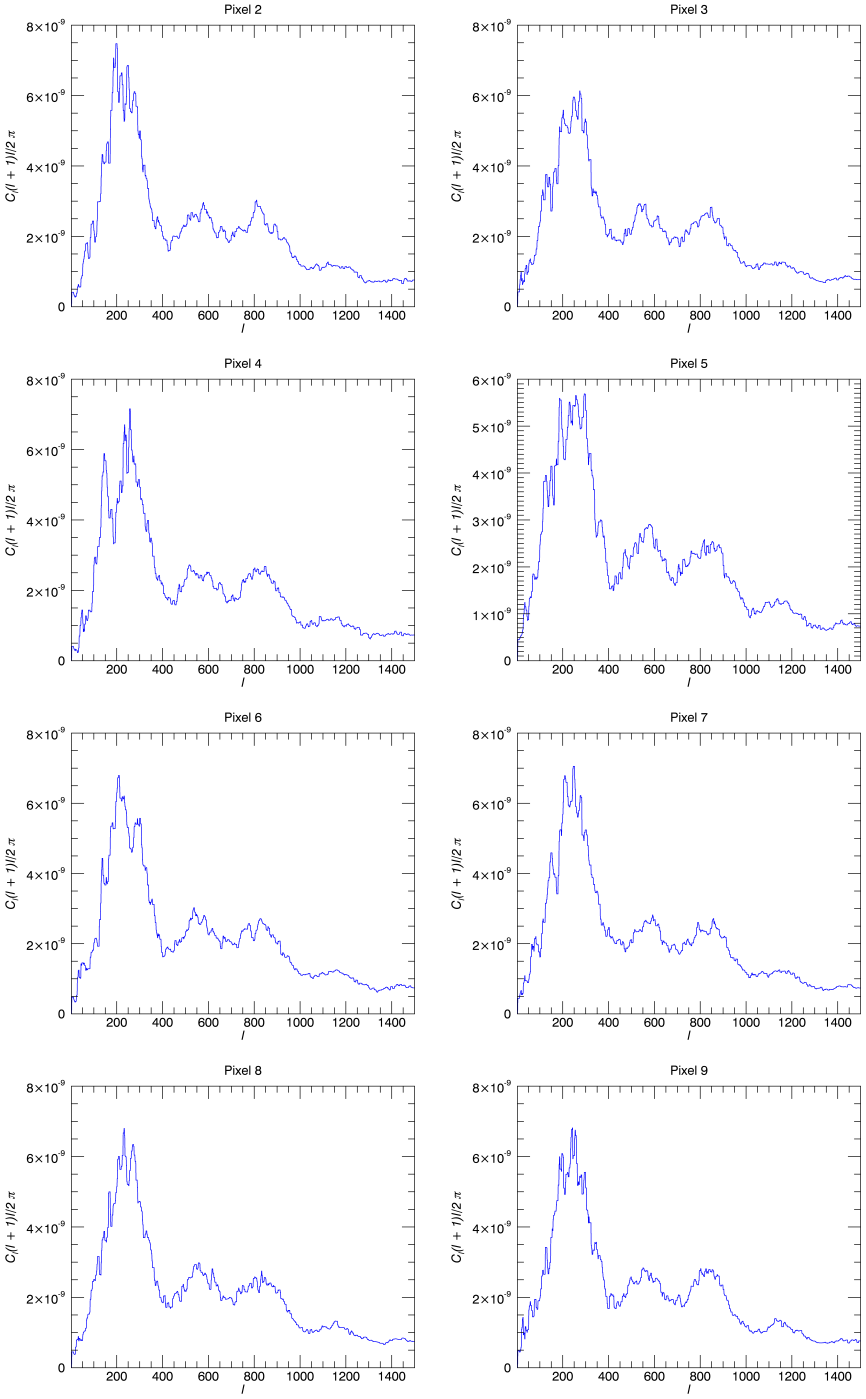

Figure C.6: Continuous power spectrums in pixels from the top of an $N_{\text{side}} = 1$ map and through the equator. Included to give a comparison between pixels in heavily masked and not areas in $N_{\text{side}} = 1$ to the highly oscillating power spectrums shown in figure C.5.

Bibliography

Adam, R. et al. (2016). Planck 2015 results. I. Overview of products and scientific results. *Astron. Astrophys.*, 594:A1.

Ade, P. A. R. et al. (2014a). Planck 2013 results. I. Overview of products and scientific results. *Astron. Astrophys.*, 571:A1.

Ade, P. A. R. et al. (2014b). Planck 2013 results. XII. Diffuse component separation. *Astron. Astrophys.*, 571:A12.

Ade, P. A. R. et al. (2014c). Planck 2013 results. XV. CMB power spectra and likelihood. *Astron. Astrophys.*, 571:A15.

Ade, P. A. R. et al. (2014d). Planck 2013 results. XVI. Cosmological parameters. *Astron. Astrophys.*, 571:A16.

Ade, P. A. R. et al. (2014e). Planck 2013 results. XXII. Constraints on inflation. *Astron. Astrophys.*, 571:A22.

Ade, P. A. R. et al. (2014f). Planck 2013 results. XXIII. Isotropy and statistics of the CMB. *Astron. Astrophys.*, 571:A23.

Ade, P. A. R. et al. (2014g). Planck 2013 Results. XXIV. Constraints on primordial non-Gaussianity. *Astron. Astrophys.*, 571:A24.

Ade, P. A. R. et al. (2016a). Planck 2015 results. XII. Full Focal Plane simulations. *Astron. Astrophys.*, 594:A12.

Ade, P. A. R. et al. (2016b). Planck 2015 results. XIII. Cosmological parameters. *Astron. Astrophys.*, 594:A13.

Ade, P. A. R. et al. (2016c). Planck 2015 results. XVI. Isotropy and statistics of the CMB. *Astron. Astrophys.*, 594:A16.

Axelsson, M., Fantaye, Y., Hansen, F., Banday, A., Eriksen, H., & Gorski, K. (2013). Directional dependence of λcdm cosmological parameters. *ApJL*, 773(1):L3.

Bennett, C. et al. (2003). First year Wilkinson Microwave Anisotropy Probe (WMAP) observations: Foreground emission. *Astrophys. J. Suppl.*, 148:97.

Bennett, C. L. et al. (2011). Seven-year Wilkinson Microwave Anisotropy Probe (WMAP) Observations: Are There Cosmic Microwave Background Anomalies? *Astrophys. J. Suppl*, 192:17.

Boas, M. L. (2006). *Mathematical methods in the physical sciences*. Wiley.

Cahill, K. (2013). *Physical Mathematics*, pages 318–323. Cambridge University Press.

de Oliveira-Costa, A., Tegmark, M., Zaldarriaga, M., & Hamilton, A. (2004). The Significance of the largest scale CMB fluctuations in WMAP. *Phys. Rev.*, D69:063516.

Dodelson, S. (2003). *Modern Cosmology*. Academic Press.

Ehlers, J., Geren, P., & Sachs, R. (1968). Isotropic solutions of the einstein-liouville equations. *Journal of Mathematical Physics*, 9(9):1344–1349.

Einstein, A. (1916). Die grundlage der allgemeinen relativitätstheorie. *Annalen der Physik*, 354(7):769–822.

Eriksen, H., Hansen, F., Banday, A., Górski, K., & Lilje, P. (2004). Asymmetries in the cosmic microwave background anisotropy field. *ApJ*, 605(1):14.

Fixsen, D. J. (2009). The temperature of the cosmic microwave background. *ApJ*, 707(2):916.

Gorski, K., Hivon, E., Banday, A., Wandelt, B., Hansen, F., Reinecke, M., & Bartelmann, M. (2005). Healpix: a framework for high-resolution discretization and fast analysis of data distributed on the sphere. *ApJ*, 622(2):759.

Gott, III, J. R., Juric, M., Schlegel, D., Hoyle, F., Vogeley, M., Tegmark, M., Bahcall, N. A., & Brinkmann, J. (2005). A map of the universe. *Astrophys. J.*, 624:463.

Hinshaw, G. et al. (2003). First year wilkinson microwave anisotropy probe (wmap) observations: Angular power spectrum. *Astrophys. J. Suppl.*, 148:135.

Hivon, E., Górski, K. M., Netterfield, C. B., Crill, B. P., Prunet, S., & Hansen, F. (2002). Master of the cosmic microwave background anisotropy power spectrum: a fast method for statistical analysis of large and complex cosmic microwave background data sets. *ApJ*, 567:2.

Horvath, I., Bagoly, Z., Hakkila, J., & Toth, L. V. (2015). New data support the existence of the Hercules-Corona Borealis Great Wall. *Astron. Astrophys.*, 584:A48.

Horvath, I., Hakkila, J., & Bagoly, Z. (2014). Possible structure in the GRB sky distribution at redshift two. *Astron. Astrophys.*, 561:L12.

Keel, W. (2007). *The Road to Galaxy Formation*. Springer Praxis Books. Springer Berlin Heidelberg.

Komatsu, E. et al. (2003). First year Wilkinson Microwave Anisotropy Probe (WMAP) observations: tests of gaussianity. *Astrophys. J. Suppl.*, 148:119–134.

Lay, D. C. (2006). *Linear algebra and its applications, 2003*. Addison Wesley, Boston.

Lee Rodgers, J. & Nicewander, W. A. (1988). Thirteen ways to look at the correlation coefficient. *The American Statistician*, 42(1):59–66.

Lyth, D. H. (1993). Introduction to cosmology. *arXiv preprint astro-ph/9312022*.

Park, C. G. (2004). Non-gaussian signatures in the temperature fluctuation observed by the wilkinson microwave anisotropy probe. *Monthly Notices of the Royal Astronomical Society*, 349(1):313–320.

Paykari, P. and Starck, J. L. (2012). Cmb data analysis. In: *Advances in Machine Learning and Data Mining for Astronomy*, M. Way, J. Scargle, K. Ali, & A. Srivastava, ed. Chapman & Hall/CRC.

Peiris, H. V. et al. (2003a). First year Wilkinson Microwave Anisotropy Probe (WMAP) observations: Implications for inflation. *Astrophys. J. Suppl.*, 148:213–231.

Peiris, H. V. et al. (2003b). First year Wilkinson Microwave Anisotropy Probe (WMAP) observations: Implications for inflation. *Astrophys. J. Suppl.*, 148:213–231.

Smoot, G. F. (1999). Cobe observations and results. In: *AIP Conference Proceedings CONF-981098*, volume 476, pages 1–10. AIP.

Spergel, D. N. et al. (2003). First year Wilkinson Microwave Anisotropy Probe (WMAP) observations: Determination of cosmological parameters. *Astrophys. J. Suppl.*, 148:175–194.

Spergel, D. N. et al. (2007). Wilkinson Microwave Anisotropy Probe (WMAP) three year results: implications for cosmology. *Astrophys. J. Suppl.*, 170:377.

Stoeger, W., Maartens, R., & Ellis, G. (1995). Proving almost-homogeneity of the universe: an almost ehlers-geren-sachs theorem. *ApJ*, 443:1–5.

Vittinghoff, E., Glidden, D. V., Shiboski, S. C., & McCulloch, C. E. (2011). *Regression methods in biostatistics: linear, logistic, survival, and repeated measures models*. Springer Science & Business Media.